Nonlinear Near-Field Dynamics of Plasmonic Nanostructures

By

Roderick B. Davidson II

Dissertation

Submitted to the Faculty of the

Graduate School of Vanderbilt University

in partial fulfillment of the requirements

for the degree of

DOCTOR OF PHILOSOPHY

in

Physics

December, 2016

Nashville, Tennessee

Approved:

Richard F. Haglund Jr., Ph.D.
Sandra J. Rosenthal, Ph.D.
Jason G. Valentine, Ph.D.
Kalman Varga, Ph.D.
Yaqiong Xu, Ph.D.
Benjamin J. Lawrie, Ph.D.

This work is dedicated to my father and my sister.

Their support has enabled me to chase my dreams with reckless abandon.

iii

TABLE OF CONTENTS

LIST OF FIGURES

Chapter 1

Introduction

1.1 Motivation

Nonlinear optics refers to that class of light-matter interactions in which the dielectric response is not linear in intensity. These effects make up the field termed as nonlinear optics in which the nonlinearity lies in the relationship between the driving electric field and the dipole moment per unit volume of the material. Almost all nonlinear optical effects hold potential for using light to control the state of optical signals. This capacity for manipulation brings the idea of optically-driven computation a great deal closer to reality in the same way that the invention of transistors revolutionized the field of electronics. In order to do this practically we need large efficiencies and low requisite powers. Both of these ends are served by generating stronger nonlinearities in the medium.

There are two different approaches for increasing the strength of these nonlinearities. The first method is to generate optical pulses that concentrate light in both time and space to such a degree that the electric fields associated with those pulses are large enough to drive these nonlinearities. The second method lies in the choice of the medium in which the optical pulse is generating nonlinear emissions. Due to asymmetric atomic arrangements, bulk crystals such as beta-barium borate or lithium niobate boast large optical nonlinearities that are capable of reaching conversion efficiencies of ~ 0.8 of the theoretical maximum for nonlinear processes such as harmonic generation. Even though bulk crystals like BBO can be efficient generators of nonlinear emission, the optical interaction volume they require to do this is prohibitively large for many applications in active optical circuitry.[1, 2] Unlike electronic circuits, optical processes do not generate enough heat to create a thermal bottleneck for increasing packing densities in logic units. If nonlinear optical components can be

1

made small enough to compare with existing technology, they will be poised to overcome fundamental limitations on electronics.[3, 4]

A promising solution to this problem has emerged from the field of plasmonic meta-surfaces. These are planar arrangements of metallic or dielectric nanostructures with sub-wavelength physical features. The electron plasmas in these particles are capable of confining the electric field from an optical source into nanoscale mode volumes. [5] The drastic increase in the electric field intensity that results from this confinement is ideal for driving optical nonlinearities. Previous work has demonstrated plasmonic nanoparticles with stronger nonlinearities per unit volume than that of BBO. [6, 7] However, this is not solely due to the increase in electric field intensity facilitated by the plasmon. The geometry of each individual nanoparticle making up the metasurface as well as their arrangement with respect to one another can be used to engineer an entirely new set of dielectric properties not associated with the metal or dielectric comprising the particles. This new set of properties is instead connected to the spatial profile of the electric fields generated at the surface of the nanoparticle. By manipulating the shape of the metal confining the plasmonic excitation, the symmetry of the electron oscillation can be controlled with nanoscale precision while the electrons are also funneled into smaller mode volumes. This means that the nonlinear properties of plasmonic systems can be enhanced simultaneously by increasing electric field strength and the nonlinearity of the material. [8]

A major advantage of using metasurfaces for nonlinear optical interactions is that the efficiency per unit volume of a metasurface much higher than that of bulk nonlinear crystals. With efficiencies upwards of 80%, BBO can approach near unity conversion in a process such as second-harmonic generation (SHG), but it requires crystals with millimeter spatial dimensions and incident powers of order 100 GW/cm^2.[1, 2] Even though plasmonic systems can achieve impressive conversion efficiencies per unit volume, their total interaction volume is limited to the order of cubic microns by the inherent loss associated with the optical properties of metals; these dimensional constraints are relaxed somewhat, how-

ever, for dielectric plasmonic structures. This means that the total conversion efficiency of any plasmonic system is still many orders of magnitude behind conventional nonlinear optics. Consequently, many iterations of nanoparticle geometries have been designed for both symmetry breaking properties and electric-field confinement in order to generate stronger nonlinear conversion efficiencies. [6, 7, 9, 10, 11, 12]

Every advance made in the nonlinear properties of these systems allows us to generate optical nonlinearities using weaker light sources. The absolute limit of this trend is when nonlinear metasurfaces are efficient enough to operate using only a few photons as an excitation source. This regime is termed quantum nonlinear optics, and it provides a compelling solution to the problem of small interaction volumes in plasmonic systems. Experiments in cavity quantum electrodynamics (CQED) have demonstrated that when dealing with optics in the quantum regime it is possible to reach large nonlinear conversion efficiencies without utilizing intense lasers beams. [13] However, CQED experiments need to be done at cryogenic temperatures. [14] Since these temperatures require large and expensive equipment, CQED systems remain impractical even though they have achieved remarkable nonlinear interaction efficiencies. Nanostructures in the quantum regime may provide a room temperature alternative to performing quantum optical processes. They have not yet reached sufficient efficiencies to surpass the optical performance of CQED systems, but this branch of nanoscience still remains largely unexplored.

In this dissertation we demonstrate that by manipulating the near-field radiation patterns of complex plasmonic nanostructures, we can engineer metasurfaces with greatly enhanced nonlinear optical properties. By observing the nature of the far-field radiation patterns both spatially and temporally, we reveal information on how plasmons can couple to other plasmons, dielectric materials, and two-level quantum systems.

In chapter 1, we will introduce fundamental concepts of optics and plasmonics that are necessary to understand the nature of the experiments demonstrated throughout this

dissertation. Here we will discuss the underlying concepts of nonlinear optics, plasmonics and the overlap between these two fields. This is followed by a discussion of plasmonics in the quantum regime.

In chapter 2, we demonstrate the gold Archimedean nanospiral geometry as a non-linear plasmonic element. We demonstrate unprecedented second-harmonic conversion efficiency in an all-metallic plasmonic element.[15] The nanospiral is also shown to have strongly chiral optical effects in the form of polarization conversion associated with its nonlinear emissions. The near-field plasmon profiles of the distinct resonance modes of the nanospiral are experimentally investigated using electron-beam induced luminescence (cathodoluminescence).

In chapter 3, we exhibit the gold serrated nanogap plasmonic geometry in order to demonstrate ultrafast control over plasmonically induced nonlinearities in a polymer film. We use spatial light modulation techniques to reveal interferometric data on second-harmonic emission with attosecond time resolution, and use this enhanced temporal resolution to sep-arate nonlinear emission from the polymer film from plasmonic scattering. [16]

In chapter 4, we investigate the photon statistics of nitrogen vacancy centers in dia-mond nanocrystals being excited by an electron beam. We use second-order correlation measurements to demonstrate Rabi flopping in a strongly driven two-level system. The diamond nanocrystals are coupled to a plasmonic silver pillar in order to induce stronger cathodoluminescence signals and therefore greater signal to noise ratios.

Chapter 5 concludes the dissertation with a discussion of the importance of nonlinear effects for plasmonic applications. We discuss how a fully quantum mechanical model of plasmonic nonlinearities can lead to the advancement of optically active plasmonic ele-ments and lead to the realization of practical on-chip devices.

1.2   Nonlinear optics

Several interactions between photons and matter are most easily described by the funda-mental property known as dielectric susceptibility, which relates the response of the charge

distribution of the matter to an externally applied electric field. Precisely stated, the dipole per unit volume, or polarizability, can be expressed in terms of a power series of the local electric-field as shown in equation.1.1.

$$P_i = P_0 + \varepsilon_0 [\chi_{ij}^{(1)} E_j + \chi_{ijk}^{(2)} E_j E_k + \chi_{ijkl}^{(3)} E_j E_k E_l + \cdots] \tag{1.1}$$

where $\tilde{P}$ represents the polarizability tensor of a given material, P_i represents the coordinates of each specific element of that tensor, $\chi^{(n)}$ the nth order susceptibility, and $\tilde{E}$ represents the external electric field applied to the material. $\chi_{ijk...}$ are the tensor components of the nonlinear susceptibilities, with the indices i,j,k,... referring to the anisotropic optical response of the material referred to Cartesian coordinates.

The first term, P_0, represents a ferroelectric which has a permanent electric dipole structure. While this term is of considerable interest for applications in electronics, it is not relevant to the experiments described here. The second term in this equation describes the polarization characteristics of linear optics. Specifically, it states that a materials charge distribution responds linearly to an externally applied electric field. This can be easily understood in the case of linear absorption. In most circumstances, the laser energy absorbed by a material from a laser beam will be directly proportional to the total amount of energy that the laser applies to the material. Implicit in this linear response theory is the assumption that the absorbed light does not change the optical properties of the material. Of course, like many of the assumptions in physics, it can be broken. [17, 18]

Nonlinear optics involves exactly these scenarios in which the dielectric properties of a material have a strong dependence on the intensity of the light passing through it, and they can be described using those terms in equation 1.1 that follow the linear term. However, there are requirements on both the electric fields and susceptibilities for efficient nonlinearities. Most bulk materials have an atomic or molecular arrangement such that $\chi^{(2)}$ and higher-order terms are much smaller than $\chi^{(1)}$. This means that the electric fields necessary to generate appreciable nonlinear terms are prohibitively large. Thus, even though multi-

quantum transitions - such as two-photon absorption - were predicted in 1931, it was not possible to demonstrate these effects in the laboratory. [19] With the invention of the laser in 1960, the requisite electric fields became readily available, so that seminal experiments in nonlinear optics were documented in less than a year afterward.[20, 21] Even in the early stages of laser technology, it became possible to probe the higher order polarizabilities of several materials such as quartz and other semiconductor based compounds. [4, 18]

Some of the more important nonlinear effects are the ones that allow for efficient energy conversion and modulation. Sum- and difference-frequency generation allow for multiple frequencies of light to interfere with one another to produce frequencies that are linear combinations of the initial frequencies. The list of specific nonlinear processes is lengthy, but each of these processes can be attributed to a specific term in equation 1.1. Since a large portion of the research presented here is centered on second-harmonic generation (SHG), we will examine more closely the term in which it is rooted: the second-order polarizability, $P^{(2)}$.

As can be seen in reference [3], if we treat the electric field $\tilde{E}$ as a complex time-dependent vector containing two distinct frequencies, ω_j and ω_k, such that,

$$\tilde{E} = E_{\omega_j}e^{(-i\omega_j t)} + E_{\omega_k}e^{(-i\omega_k t)} + E_{\omega_j}^*e^{(i\omega_j t)} + E_{\omega_k}^*e^{(i\omega_k t)} \tag{1.2}$$

where the last two terms are the complex conjugates of the first two, the second order nonlinear polarizability can be conveniently written in a summation.

$$\tilde{P}^2(t) = \sum_j P(\omega_j)e^{-i\omega_j t} \tag{1.3}$$

where the sum is over all values of j, thus over positive and negative frequencies. Under this convention we can separate each term and derive a unique interaction from each. The amplitudes of these interactions can then be written as

$$P(2\omega_j) = \varepsilon_0 \chi^{(2)} E_j^2 \quad (SHG)$$

$$P(\omega_j + \omega_k) = 2\varepsilon_0 \chi^{(2)} E_j E_k \quad (SFG)$$

$$P(\omega_j - \omega_k \neq 0) = 2\varepsilon_0 \chi^{(2)} E_j E_k^* \quad (DFG) \tag{1.4}$$

$$P(\omega_j - \omega_k = 0) = 2\varepsilon_0 \chi^{(2)} (E_j E_j^* + E_k E_k^*) \quad (OR)$$

These processes in the order listed above are, second-harmonic generation (SHG), sum-frequency generation (SFG), difference-frequency generation (DFG), and optical rectification (OR) where ω_1 is always larger then ω_2. The physical origin of these interactions is denoted by the linear combinations of ω_j and ω_k denoted on the left side of each equation. And, finally, optical rectification is the generation of a quasi-static polarization resulting from the destructive interference of two degenerate frequencies.[3]

In order to relate these polarizabilities to measurable quantities, we must relate the incident electric field to the nonlinear polarizability. We can do this by starting with Maxwell's equations and deriving the normal optical wave equation, equation 1.5, under the assumption that the material is nonmagnetic and the space contains no free charges or currents.

$$\nabla \times \nabla \times \tilde{E} + \frac{1}{c^2} \frac{\partial^2}{\partial t^2} \tilde{D} = 0 \tag{1.5}$$

If we now assume the material properties are nonlinear, we can let the displacement vector, $\tilde{D}$, have an additional term such that,

$$\tilde{D} = \tilde{E} + 4\pi \tilde{P}$$

$$\tilde{P} = \tilde{P}^{(1)} + \tilde{P}^{(n>1)} \tag{1.6}$$

After substituting the displacement term in equation 1.5 with the displacement term in

equation 1.6, we can derive the an inhomogeneous wave equation.

$$\nabla \times \nabla \times \tilde{E} + \frac{1}{c^2}\frac{\partial^2}{\partial t^2}\tilde{D}^{(1)} = \frac{-4\pi}{c^2}\frac{\partial^2}{\partial t^2}\tilde{P} \qquad (1.7)$$

From here, we can directly represent the tensor components of each nonlinear suscepti-bility from the nonlinear conversion efficiencies and the incident electric field intensities nonlinear polarizations, although, it is often easier to reduce this to an effective nonlinear susceptibility for a given electric field polarization. For the case of second-order nonlinear-ities, this would entail a simplification of the second order polarizability to,

$$\tilde{P}^{(2)} = \varepsilon_0 d_{eff}^{(2)}\tilde{E}^2 \qquad (1.8)$$

Since a large portion of the experiments focus on SHG, we will focus on this particular nonlinear interaction for the remainder of this discussion of nonlinear optics.

1.2.1 Second-harmonic generation

As seen in equation 1.4, the efficiency with which SHG can produced from a given material is determined by the second-order susceptibility of the material or the strength of the electric field applied to the material. Simply increasing the electric field strength using ever more powerful lasers eventually runs into practical limitations. In order to realize practical application of SHG we must create materials with larger nonlinear conversion efficiencies at lower optical excitation densities. If we examine the nature of the second-order polarizability term, there is an obvious symmetry provided by the $\tilde{E}^2$ term. To make the ramifications of this symmetry clear, we will make a few assumptions about the material and the incoming electric field. Figure 1.1 shows two crystalline structures. The fluorite crystal geometry in figure 1.1a has a centro-symmetric structure about the axis shown by a dashed black line. This means that the crystal structure is identical to its mirror image about this line. The same is not true for the the zinc-blende configuration in figure 1.1b which has a non-centrosymmetric geometry that can be found in gallium arsenide crystals.

Gallium arsenide is an efficient generator of even-ordered harmonic emissions for this very reason.

To understand why we must visualize two anti-parallel electric fields that are orthogonal to this axis of symmetry, as drawn by the red and blue arrows shown in Figure 1.1. In the centrosymmetric crystal, the potential experienced by the shift in charge distribution by either electric field is identical because the mirror image of the crystal structure would not experience a different local electric field. Therefore it is possible to write the following two equations:

$$\tilde{P}^{(2)} = \varepsilon_0 \chi^{(2)} \tilde{E}^2 \qquad\qquad -\tilde{P}^{(2)} = \varepsilon_0 \chi^{(2)} [-\tilde{E}]^2 \qquad\qquad (1.9)$$

Since the electric field term is positive upon being squared, the only solution to these equations in the presence of a non-zero polarization is the trivial one. So it follows that,

$$\tilde{P}^{(2)} = -\tilde{P} \qquad\qquad \chi^{(2)} = 0 \qquad\qquad (1.10)$$
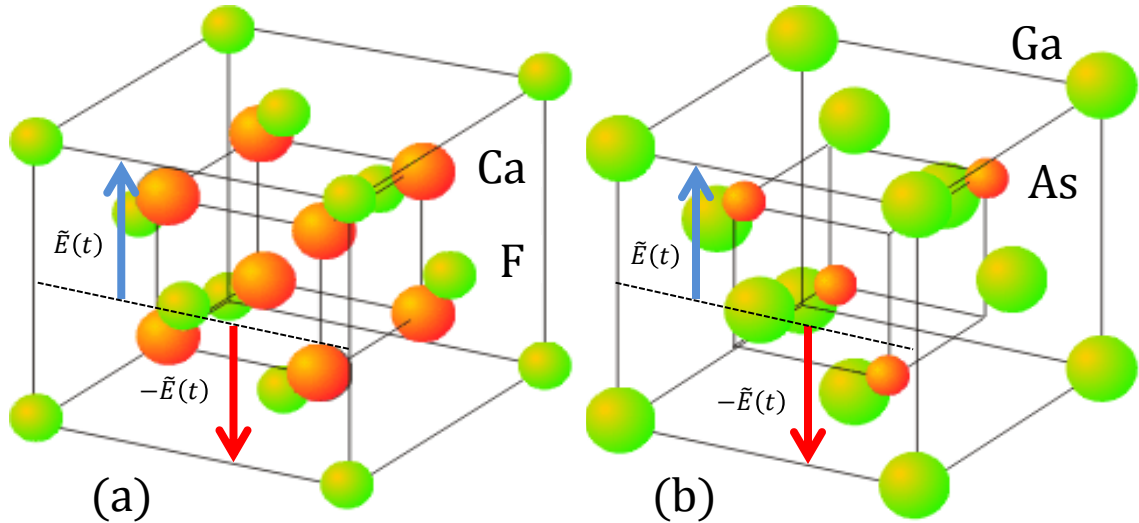
Figure 1.1: (a) A fluorite crystal structure exhibited by calcium fluoride (CaF_2) exemplifying a centro-symmetric crystal. (b) A zinc-blende crystal structure exhibited by gallium arsenide (GaAs) exemplifying a non-centrosymmetric crystal. GaAs is a strong generator of second-harmonic light. The red and blue arrows mark the directions of anti-parallel electric fields.[22]

This all changes when considering the non-centrosymmetric crystal. Since we can no longer make the assumption of identical electrical potentials upon mirror inversion, equation 1.6 is no longer true and $\chi^{(2)}$ can have non-zero values. It is important to note that the sensitivity $\chi^{(2)}$ has to orientation of the incident electric field and the crystal structure creates a polarization dependence of second-harmonic emissions in almost any experiment. This dependence can also create properties of the material that would normally be hidden in linear optics.[3] This fact is a major motivation for the research presented in chapters 2 and 3.

1.2.2 Experimental Characteristics of SHG

A defining characteristic of all of the nonlinear processes listed in equation 1.4 is that they are parametric processes. This means that the initial and final quantum state of the material are identical. The state of the material may change during the process, but only during the short lifetime of the process. These temporary states are known as virtual states, depicted in Figure 1.2 as dashed lines, and since no actual absorption takes place, their lifetimes defined by the uncertainty principle. The lifetime of a virtual state is on the order of $\hbar/\Delta E$ where ΔE is the energy difference between the virtual state and the closest real state. For an excitation in gallium arsenide by a photon with an 800 nm wavelength, a virtual state would have an upper limit on lifetime of approximately 30 fs. These short lifetimes can be useful for experimentally differentiating SHG from two-photon absorption and hyper Raleigh scattering. These are nonlinear processes that are also capable of generating signals at 2ω, however, since they induce a change in the quantum state of the material when they occur, they are non-parametric. These processes generally have lifetimes that are defined by the decay rate of the excited state. These lifetimes are typically on the order of nanoseconds or longer in isolated atomic or molecular systems, which is several orders of magnitude longer than the lifetime of typical virtual states. [3, 23]

Another common means of identifying a signal at 2ω as SHG is to observe the dependence of $\tilde{P}^{(2)}(2\omega)$ on the square of the electric field as shown in equation 1.7. The
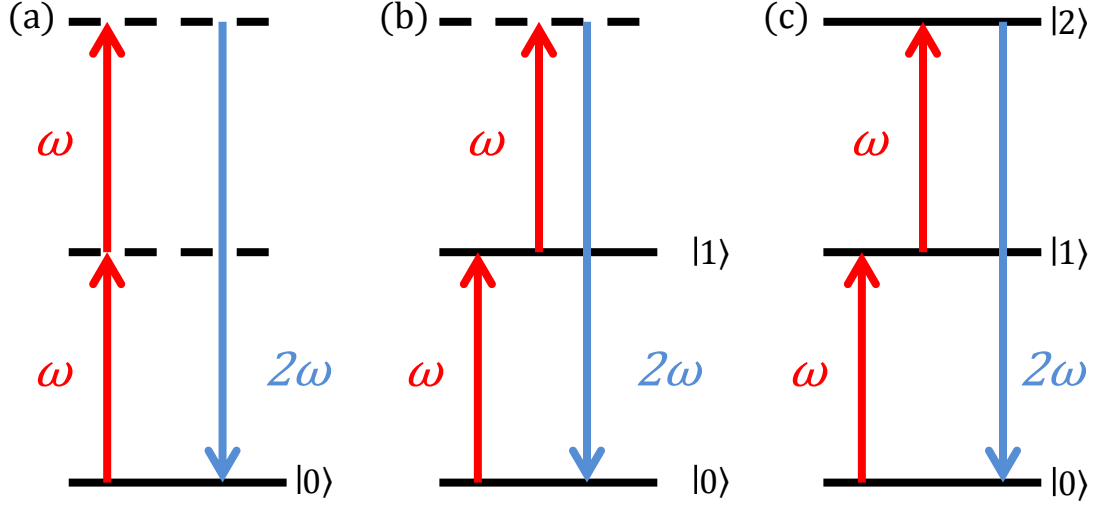
Figure 1.2: (a) Energy states of the second-harmonic generation process. Two photons are absorbed into virtual states (dashed lines) and emitted as a single photon as 2ω. (b) and (c) are two instances of sequential two-photon absorption with a single real state and single virtual state (b), and two real states (c). This simplified schematic is not generally applicable to atomic and molecular systems because of parity selection rules.

dependence of the SHG conversion efficiency on the intensity of an incident light source can then be derived utilizing two approximations. The slowly varying envelope approximation makes the simplification that the envelope of the nonlinear wave changes slowly in comparison to the wavelength of the light. Given the relationship shown in equation 1.8, the slowly varying envelope approximation yields the wave equation for 2ω as,

$$\frac{\delta E(2\omega)}{\delta z} = -\frac{i\omega}{n_{2\omega}c}d_{eff}E^2(\omega)e^{i\Delta kz} \tag{1.11}$$

where $\Delta k = k(2\omega) - 2k(\omega)$.

For small enough conversion efficiencies and relatively weak pump beams,, we can assume the amplitude of $E(\omega)$ remains unchanged throughout the length of the interaction. Combined with the boundary condition that $E(2\omega) = 0$ when $z = 0$, we can derive the following two relations.

$$E(2\omega) \propto d_{eff}E^2(\omega) \qquad\qquad I(2\omega) \propto d_{eff}I^2(\omega) \qquad\qquad (1.12)$$

where the electric field terms are simply exchanged for the intensity terms in the second equation. Thus, the intensity of a second-harmonic light source must vary as the square of the input light intensity. Unfortunately, this analysis does not separate measurements of 2ω in the laboratory from other 2ω light sources such as two-photon absorption because they depend on the square of the input light intensity as well. However, this is useful for differentiating the true 2ω signal from second-order diffraction effects and fundamental leakage as well as other problems that can plague a harmonic detection scheme since they will generally depend linearly on the fundamental intensity.[24]

The importance of SHG in applications of nonlinear optics lies in the fact that it has relatively high efficiency compared to other nonlinear optical interactions and still allows for optical modulation. This means that it could be used for data analysis and signal manipulation. Crystals such as beta barium borate (BBO) and potassium dideuterium phosphate (KDP), boast effective second-order nonlinearity coefficients of up to $2 \cdot 10^{12}$m/V. Second-harmonic conversion efficiencies within these crystals can be larger than 0.1 if provided enough optical interaction volume. This is typically on the order of cubic millimeters.[25, 1] These volumes prohibit any competitive analogs to active electronic circuitry that is already operating on the order of 100 nm^2.[26]

However, there are still certain aspects of optical circuitry that give it a unique advantage over its electrical counterparts. Heat generation and size limitations are a fast approaching bottleneck for electronic computing. Optical circuitry would be inherently less lossy and would generate far less heat. The field of plasmonics has arisen as a potential solution for the power and size limitations of applications in nonlinear optics. The past decade has witnessed substantial progress in utilizing nanoscale metallic systems for the manipulation of light on an unprecedented spatial and temporal scale. However, optical losses in metals are too high and nonlinear conversion efficiencies are still too low to real-

ize practical applications. This next section will describe aspects of electromagnetic theory that are important to understanding the cross-section of nonlinear optics and plasmonics.

1.3   Electromagnetic theory of plasmons

Plasmonics is a branch of optics dealing with the interaction of conductors with size features on the nanoscale with optical energy sources. These plasmonic systems can be described in large part by comparison to their macroscale counterpart, antennas. The standard definition of an antenna is a device for radiating or receiving MHz to GHz radiation. Most plasmonic structures are designed to resonate in the optical and infrared instead of the radio bands, however the physical laws that dictate how they manipulate the directionality and localization of electromagnetic radiation are the same. [27, 28]

An antenna serves to direct radiation by by either converting the motion of electron into free-space radiation or by coupling radiation to an electron plasma. It follows that the less resistance the antenna material has the less loss the antenna will suffer. Common materials for radio wave antennas are copper and aluminum because the skin depth decreases so rapidly with increasing frequency and the resulting power loss is too great. When scaling these antennas to resonate in the optical band however, these metals begin to incur much greater loss to both radiative and non-radiative decay paths. This is the source of most of the differences between optical and radio antenna design. Common materials for optical antennas are metals with the lowest possible resistivity. Gold and silver are perhaps the most common metals to use in plasmonics. Additionally, the shape of the optimal geometry of the optical antenna will vary greatly depending on the its specific purpose and resonant wavelength. Radio wave antennas will either be designed to maximize their electromagnetic cross-section with respect to their own physical size or direct radiation in a highly concentrated solid angle. Optical antennas, on the other hand, are not able to reach the efficiencies of radio antennas for these processes. Instead they excel at localizing and concentrating of incident radiation. [29]

The diffraction limit constrains the spatial resolution that can be reached by classical

13
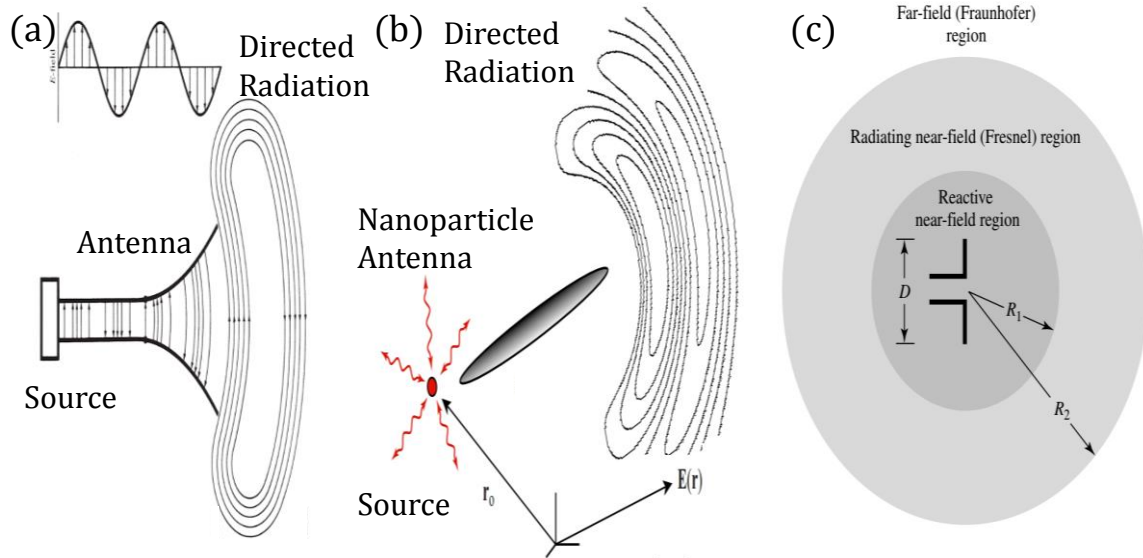
Figure 1.3: (a) Classic antenna design with an electromagnetic source and radiation pattern on the macroscale. [27] (b) Plasmonic antenna with a light emitting particle source and directed radiation pattern on the nanoscale.[29] (c) Regions surrounding an antenna of dimension size D.[27]

optics to the order of $\lambda/2$. There are three spatial regions around the antenna, the near field, intermediate field, and far field. These regions define the amount of information remaining in an emitters radiation patterns after damping and diffraction terms begin to take over. These regions are illustrated in figure 1.3c. If we had a detector in the far field region, also known as the Fraunhofer region, it would be unable to determine the spatial profile of the antenna as diffraction effects would have become too large for the image to be recovered. The reactive near-field region lies much closer to the antenna and is what we refer to by the near field throughout this dissertation. This is the region where a detector is capable of mapping out the precise spatial profile of the electric fields surrounding the antenna. In between these two regions is a transitional area known is the radiating near-field or Fresnel region. The angular distribution of the antenna radiation patterns dominate this region.[27] The definitions for these regions do not hold for antennas with feature sizes below the diffraction limit, but they can be understood in terms of what information about the antennas resonance can be measured with a detector at any point.[30]

Here we will outline the three major categories of plasmons, bulk plasmons, surface plasmon polaritons and localized surface plasmons, and the underlying theory of the near-field radiation of plasmons.

1.3.1   The bulk plasmon

In the free electron gas model, electrons are assumed to be unaffected by either collisions with other electrons or interactions with the crystal lattice potential. The impedance to electron motion and free charge carrier densities are properties of the specific metal in question. An important characteristic of any of these metals is the plasma frequency, ω_{plasma}. It is defined by equation 1.13 and represents the threshold frequency at which the electrons are unable to respond fast enough to react with light of a higher frequency.

$$\omega_{plasma} = \sqrt{\frac{ne^2}{\varepsilon_0 m}} \tag{1.13}$$

where n is the number density of free moving electrons, e is the charge of a single electron, and m is the effective optical mass of the electron. The plasma frequency separates two optical regimes of the conductor where the incident radiation, ω, is either greater or less than ω_{plasma}. The bulk plasmon can be excited in that region where $\omega > \omega_{plasma}$, known as the transparency regime, where electromagnetic waves can propagate through the volume of the metal. The dispersion relation for bulk plasmon excitation can be seen in figure 1.4b and is given by the dispersion of traveling waves, equation 1.14.

$$\omega^2 = \omega_{plasma}^2 + k^2 c^2 \tag{1.14}$$

where K represents the plane-wave components of the wave vector. Bulk plasmons are typically higher energy than the optical band photons. Sometimes they can extend into the deep ultraviolet bands. The phase matching conditions of the bulk plasmon precludes it from being directly excited with optical radiation. They are typically observed in experiments where electrons are used as an excitation source such as electron energy loss

(a)   (b)
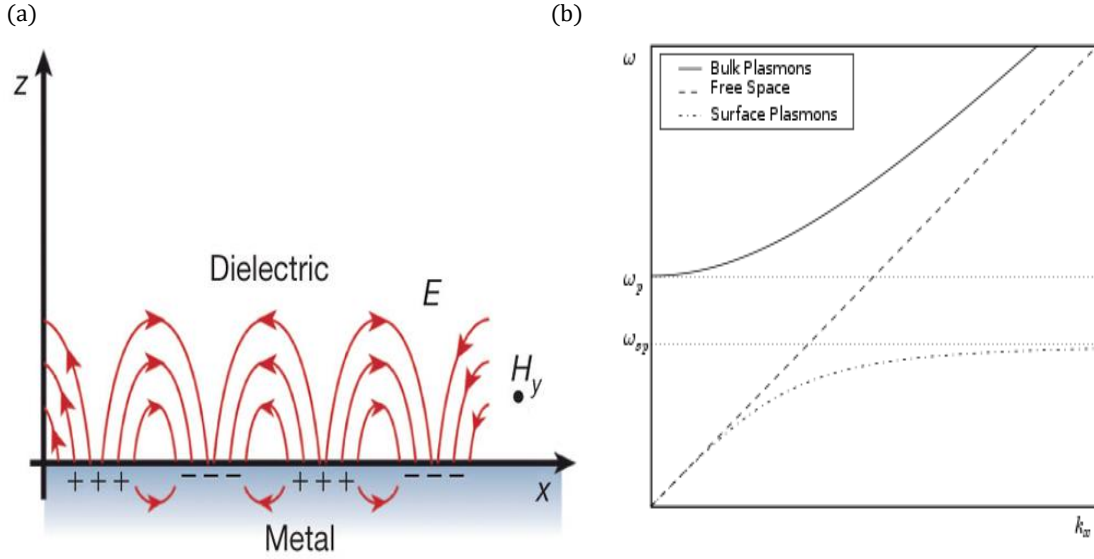
Figure 1.4: (a)Surface plasmon polariton propagating across a metallic interface.[31] (b) Dispersion relation of bulk plasmons (solid line) and surface plasmons (dashed line) [32]

spectroscopy.[5]

1.3.2 The surface plasmon polariton

While electromagnetic waves with a frequency below ω_{plasma} can not propagate in the volume of a metal, this does not prevent surface effects. Unlike bulk plasmons, surface plasmons require some degree of spatial confinement in order to define a resonance effect. Surface plasmon polaritons (SPP) are such a surface effect where an electromagnetic resonance propagates along an interface between a conductor and a dielectric as can be seen in figure 1.4a. The confinement here is in the direction normal to the interface. The dispersion relation for SPPs is shown opposite the light line from the bulk plasmon dispersion in figure 1.4b and is given by equation 1.15.

$$\omega_{SPP} = \frac{\omega_{plasma}}{\sqrt{1+\varepsilon_{dielectric}}} \tag{1.15}$$

While the phase matching conditions of SPPs are not as restrictive as bulk plasmons, they still require specific angles of excitation in order to have an appreciably long lifetime, typically on the order of tens of femtoseconds. [5] A common means of coupling light

into metallic interfaces is to use a glass prism or metallic gratings to control the angle of incidence. [5]

1.3.3 The localized surface plasmon

When the metallic surface is confined in three dimensions, a non-propagating surface plasmon can be excited known as the localized surface plasmon (LSP). The optical properties of the LSP are defined by the confining geometry of the metallic surface as well as the surrounding dielectric. This is the type of plasmon that is relevant to the research presented in this dissertation. So, we will treat the theoretical background of the LSP with more detail than the previous two types. A major advantage of the LSP is that does not necessitate the phase matching conditions of the SPP.

The derivation of the LSP resonance will rely on the quasi-static approximation. The size scale of LSP supporting nanoparticles sufficiently smaller than the exciting wavelength, λ, such that this approximation yields an accurate answer. In order to derive a few crucial quantities for LSPs, we will consider the case of the spherical metal particle of radius a, with air as a surrounding dielectric shown in figure 1.5. We take the direction of
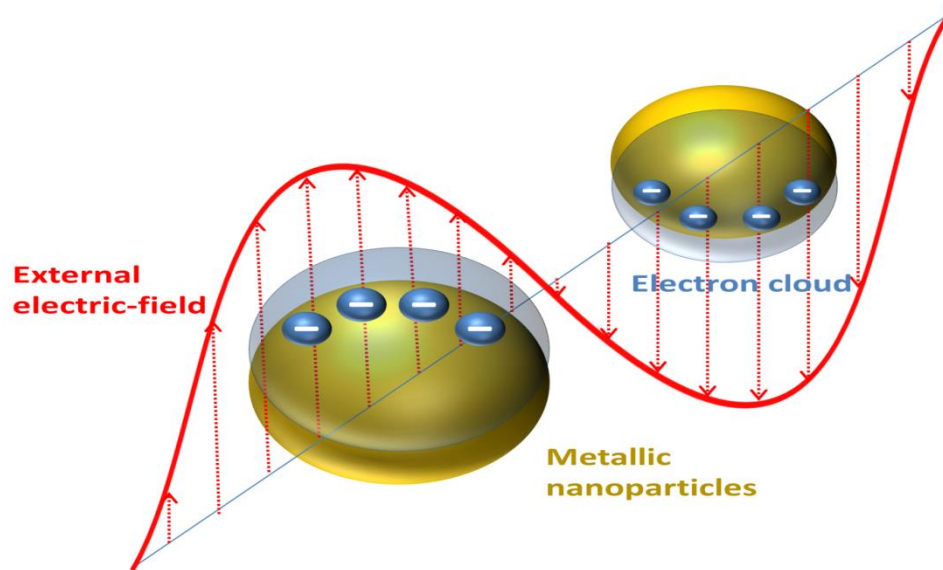
Figure 1.5: Metallic spherical nanoparticles under direct optical excitation.

propagation of the electromagnetic wave to be $\hat{\mathbf{z}}$ and the direction in which the Poynting vector of that electric field oscillates to be $\hat{\mathbf{x}}$. If we solve for the electric potential, Φ, using the Laplacian equation, $\vec{\nabla}^2\Phi = 0$, we can derive solutions for the electric fields in regions inside and outside the of the metal.

$$\mathbf{E_{in}} = \frac{3\varepsilon_m}{\varepsilon + 2\varepsilon_m}\mathbf{E}_0 \qquad \mathbf{E_{out}} = \mathbf{E}_0 + \frac{3\mathbf{n}(\mathbf{n}\cdot\mathbf{p}) - \mathbf{p}}{4\pi\varepsilon_0\varepsilon_m r^3} \tag{1.16}$$

where $\mathbf{E}_0$ is the externally applied electric field, $\mathbf{n}$ is the unit normal vector from the surface of the metal, $\mathbf{p}$ is the dipole moment as defined by equation 1.17.

$$\mathbf{p} = 4\pi\varepsilon_0\varepsilon_m a^3 \frac{\varepsilon(\omega) - \varepsilon_m}{\varepsilon(\omega) + 2\varepsilon_m}\mathbf{E}_0 \tag{1.17}$$

Here, the wavelength dependent dielectric function of the plasmon is represented by $\varepsilon(\omega)$. Since LSPs are a surface effect we are much more concerned with the E_{out} term. Specifically, it is the induced dipole moment, $\mathbf{p}$, that defines the complex polarizability of the surface resonance. When the Fröhlich condition is met, $Re(\varepsilon(\omega)) = -2\varepsilon_m$, the dipole moment of the surface plasmon is on resonance. This means that the induced electric field surrounding the metallic particle is at a maximum. Of course the $1/r^3$ term means that the electric field is highly localized close to the surface of the metal, but the enhancement factors, $\mathbf{E}_{induced}/\mathbf{E}_0$, can be as large as 10^3. [33] This quantity is determined by a number of experimental parameters and material characteristics such as surface defects, substrate interfaces, and non-radiative decay. The enhancement factors of metallic nanostructures have proven to be a powerful tool for interacting with nearby dielectrics. Later in the introduction chapter, we will refer back to this term as it is responsible for strong nonlinearities and strong coupling between nanoscale systems.

While our previous derivation of the resonant properties of the LSP used a spherical geometry for simplicity, the boundary conditions placed on this surface resonance can deviate from this model in order to create optical antennas with complex dielectric functions
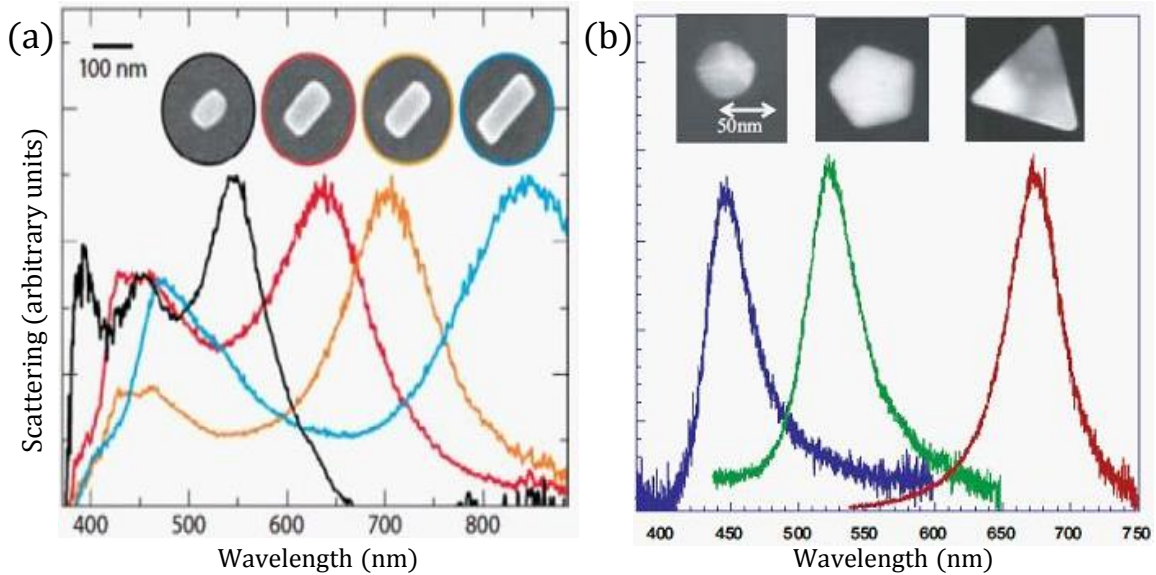
Figure 1.6: (a) Varying sizes of plasmonic nanorods and their respective resonances shown by measuring scattered light. (b) Varying geometries and their resonance spectra. Each of these was measured with unpolarized white light excitation sources. [34]

and optical responses. If instead, for example, we consider a rod-shaped nanoparticle like those in figure 1.6a, two distinct spatial distances are apparent along the short and long axis of the particle.

Since an electron on the surface of the rod would have to travel a much greater distance to resonate about the long axis, the wavelengths necessary to excite this resonance will be of longer wavelength than those that excite resonances about the short axis. Indeed, it can be seen in figure 1.6a that as the long axis is made longer, the longer wavelength peak in scattering cross section moves even further towards the infrared. Meanwhile, the shorter wavelength resonance stays constant if the short axis of the rod also remains constant. Figure 1.6b also exhibits a few plasmonic geometries that are even more complex, but the equal lengths of their major axes creates a single peaked resonance spectrum.[34]

1.4   Complex plasmonic structures - beyond the sphere and the rod

These more complex plasmonic geometries are considerably more cumbersome to solve analytically than the sphere. However, numerical analysis solutions for Maxwell's equa-

tions at the nanoscale have been widely used in order to not only determine the resonance position of arbitrarily complex plasmonic geometries, but also to simulate the spatial profile of the electric field enhancement factors in close proximity to the metallic surface. Perhaps the most widespread kinds of simulations are finite-difference time-domain simulations (FDTD). All of the near-field plasmonic simulations shown in Chapters 2-4 are generated using an FDTD simulation package written by Lumerical Solutions®. There is a brief discussion of how FDTD simulations relate to the experiments in each chapter in the respective experimental methods sections.

Even though they provide excellent support for experimental results, the idealized nature of these simulations can easily mask the experimental realities involved with fabricating and characterizing nanoscale systems. Inherent variations in nanofabrication, surface roughness, and substrate coupling are a few effects that will cause experiment to stray from idealized simulations. Regardless, these FDTD simulations provide a starting point for the time-consuming fabrication procedures.

So far we have only considered the simplest cases of plasmons in geometries the wavelength response and near field profiles of which are intuitively easy to understand. However, in order to realize practical plasmonic devices in the numerous branches in which they show promise, we will have to develop plasmonic structures that are significantly more sophisticated than a simple disc. Here we will introduce plasmonic structures with multiple spatially overlapping resonances as well as complex polarization responses. We will also discuss how plasmons are capable of coupling to one another and nearby dielectrics.

When a plasmonic structure supports multiple distinct resonances that overlap spatially, the two plasmons can hybridize to create a dielectric response that is more complex than a simple summation of the responses of the two plasmon responses alone. Let us consider the hybridization of the disc and hole illustrated in figure 1.7. These two geometries can be hybridized in the form of a ring. A plasmonic response similar to the hole structure can be observed on the interior of the ring while the plasmonic response of the disc can be
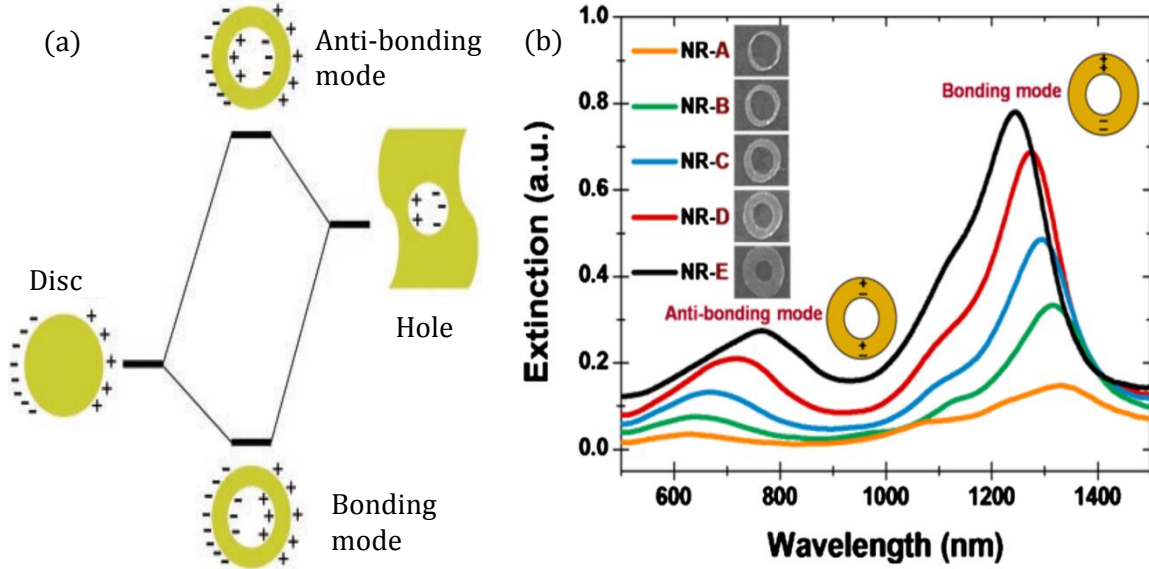
Figure 1.7: (a) Hybridization of disc and hole plasmons in a composite geometry. (b) Extinction spectra of the bonding and anti-bonding mode of the ring as a function of ring thickness. [35, 36]

observed on the exterior. The ring structure is capable of forming bonding and anti-bonding resonances. If the ring resonator is modeled using a coupled oscillator scheme, this is the equivalent of the oscillators resonating with a zero phase difference (bonding mode) and a π phase difference (anti-bonding). This complex plasmonic response takes place within a single continuous particle, but we can also engineer interesting optical phenomenon from coupling multiple particles via the electric field of the plasmon. [35, 36]

A plasmonic dimer is two particles are placed within interaction range with one another with mirror symmetry. Figure 1.8 shows two such arrangements using circular and triangular geometries. Plasmonic dimers are particularly useful for creating very large electric field enhancement factors, and can concentrate energy from a photonic source into an even smaller mode volume than single plasmonic elements. Figure 1.8b shows a plasmonic geometry known as the bowtie that is well known for using the its triangular shape to "funnel" electrons into a small metallic tip to create larger electric field enhancement factors than many other plasmonic arrangements. [38, 37]
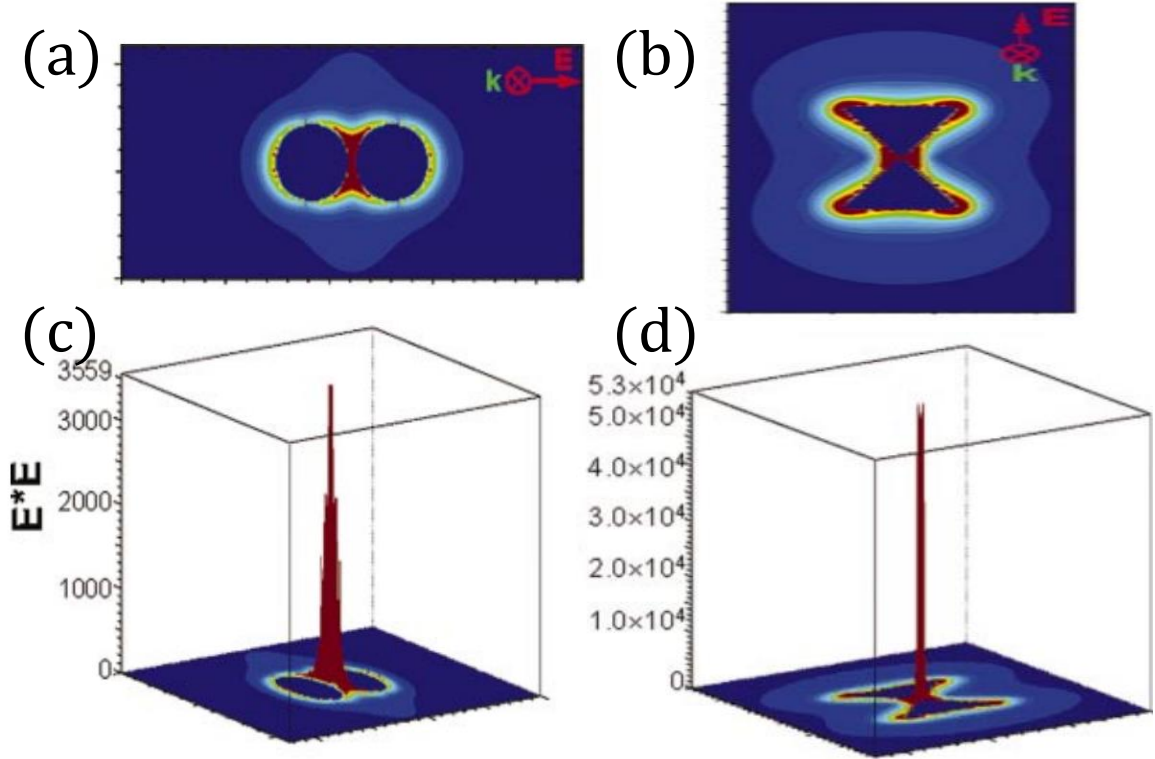
Figure 1.8: FDTD simulations of the near-field profile of plasmonic dimers. (a) Disc dimer with a 2nm gap, excited by $\lambda = 430nm$, (b) triangular dimer with a 2nm gap excited by light at 932 nm. (c)(d) Surface plots of the electric field enhancement factors shown in (a) and (b).[37]

1.5   Nonlinear plasmonics

So far we have only considered the linear optical property of plasmonic structures, but just as we are able to control optical phenomena attributed to $\chi^{(1)}$ like absorption, we can control optical effects attributed to higher order polarizabilities. As stated in the nonlinear optics section, nonlinear effects are sensitive to the strength of the local electric field and the nonlinear susceptibility of the material. Plasmonic structures are a natural fit for these studies as they make it possible to simultaneously engineer the materials dielectric properties and to generate high local electric fields. [8, 39]

Here we will focus on plasmonic examples of second-order nonlinearities, specifically SHG, using two different strategies for efficient manipulation of light. The first strategy is to generate large nonlinear susceptibilities within the plasmonic structure by itself. The sec-

ond strategy is to use the strength of the plasmonically generated electric field to enhance the nonlinear properties of a dielectric material placed in close proximity to the plasmon surface. Recalling the equation for the second-order polarizability term responsible for emission at 2ω,

$$P(2\omega) = \varepsilon_0 \chi^{(2)} E^2 \tag{1.18}$$

it is evident that a plasmonic structure that serves as an efficient generator of second-harmonic must have a nonlinear dielectric function with a relatively large $\chi^{(2)}$. In order for this to occur, the the plasmonic structure must have a broken inversion symmetry about some axis. Figure 1.9 shows several examples of plasmonic structures that utilize asymmetric boundary conditions on plasmonic resonances in order to enhance SHG conversion efficiencies.

In each instance illustrated in figure 1.9, some distortion was introduced into the plasmonic antenna in order to break symmetry about the axis perpendicular to the polarization axis of the exciting light. This asymmetry can be introduced in a single particle or from the arrangement of an array of particles. The tilted nanocup, figure 1.9c, shows particularly large SHG signal in comparison to its all metallic plasmonic competitors. It yields a conversion efficiency of up to $1.8 \cdot 10^{-9}$ with an input power of $300 \mu W$. This corresponds to a second-order nonlinear susceptibility of $3.2 pm/V$.[6] When considering the small volume these plasmonic antennas inhabit, their SHG conversion efficiency per unit volume can rival that of inorganic crystals with the strongest known nonlinearities. Since the interaction can not be scaled up without all of the optical signal being lost to non-radiative decay paths, we must strive to engineer ever more powerful plasmonic harmonic generators. We can do this by exploring the nature of symmetry breaking in plasmonic resonances. Additionally, if these antennas are exposed to optical intensities that are too large, they will be damaged via melting or ablation, and they will immediately lose their strong nonlinear properties. So promising plasmonic antennas must be able to make efficient use
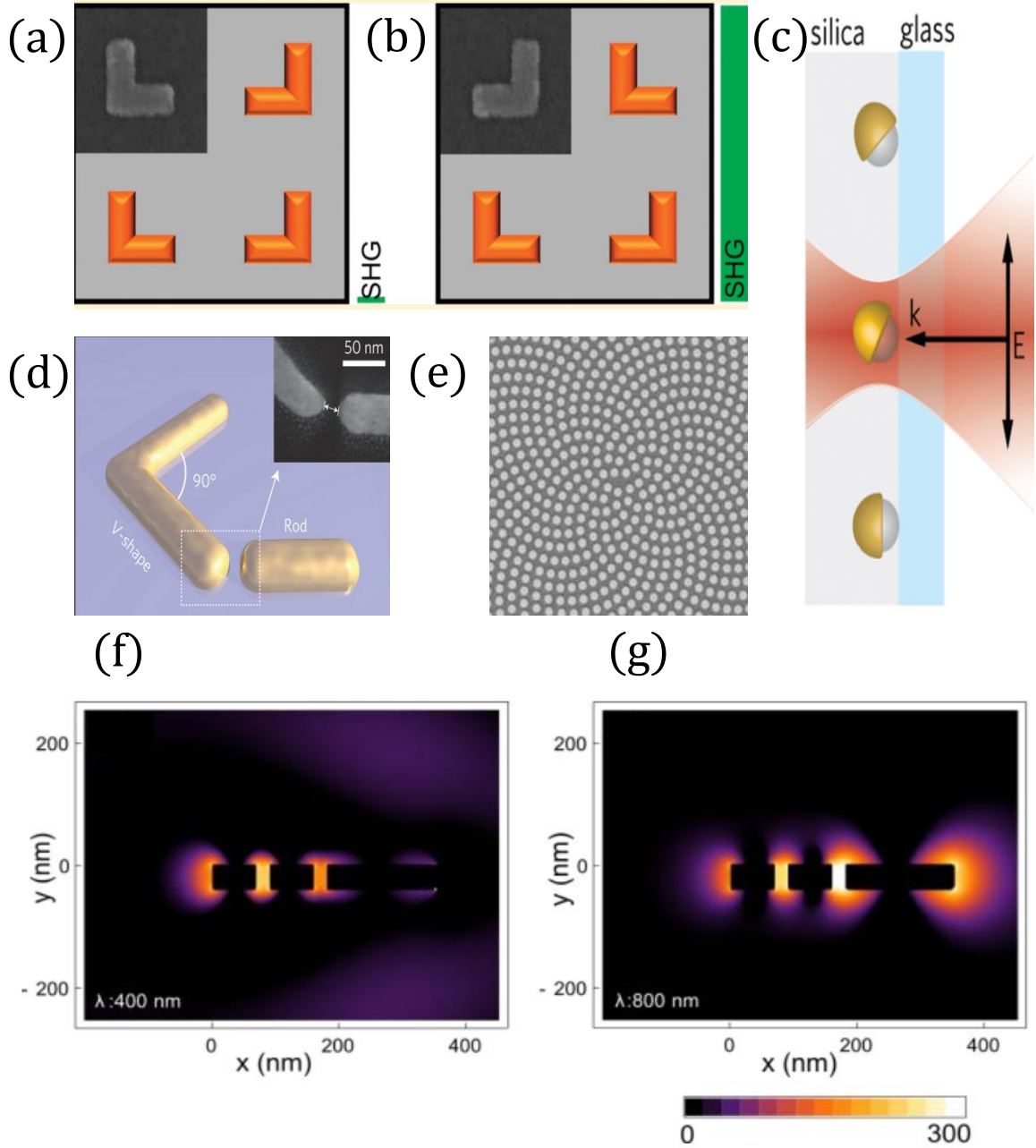
Figure 1.9: Plasmonic antennas engineered for efficient SHG conversion. (a)(b) L-shaped plasmonic structures arranged in a (a) symmetric and (b) asymmetric pattern. [12] (c) Three-dimensional nanocups with varying tilts about the polarization axis. [6] (d) Multi-resonant plasmonic coupling between L-shape and nanorod for exciting resonances at 2ω. [9] (e) Symmetric discs arranged in a spiral formation to break symmetry at the array level. [11] (f)(g) Multi-resonant coupled nanorods with near-fields calculated at (a) the SHG wavelength, $\lambda = 400nm$, and (b) the fundamental wavelength, $\lambda = 800nm$. [10]

of low intensity laser pulses or survive stronger optical intensities. Chapter 2 of this dissertation presents experimental results of record breaking SHG conversion efficiencies in the Archimedean nanospiral geometry. This is a step towards generating optically active plasmonic elements capable of efficient frequency conversion. [8]

Plasmonic antennas also excel at providing high fields in order to enhance harmonic conversion efficiency. By concentrating optical energy into a small volume occupied by a nonlinear material, plasmons are capable of generating much stronger nonlinear emissions than by bulk materials alone. Figure 1.10 shows two such instances where semiconductor systems were placed in plasmonic "hotspots" in order to enhance harmonic conversion efficiencies. In both instances, conversion efficiency enhancements of several orders of magnitude were observed over non-plasmonic systems. In the case of multi-quantum wells coupled to plasmonic antennas, figure 1.10b, SHG conversion efficiencies are observed as high as $2 \cdot 10^{-6}$. [42, 41] Chapter 3 of this dissertation describes experiments using a novel
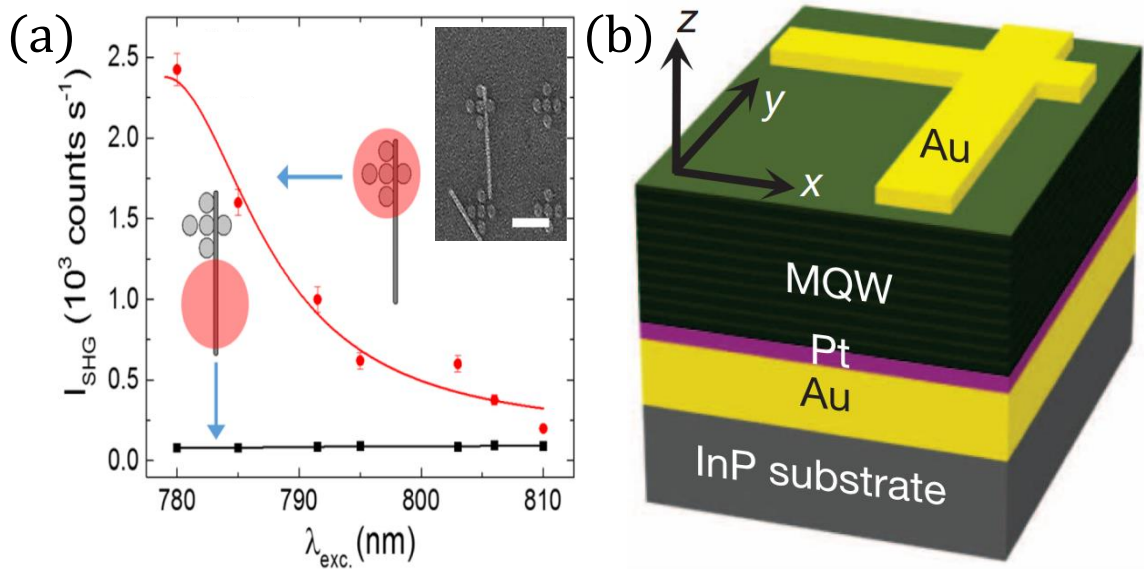
Figure 1.10: (a) Plasmonic enhancement of second-harmonic emission from a single zinc-oxide nanowire placed in the hotspot of a gold disc pentamer. Red curve shows SHG from plasmonically enhanced nanowire,.black curve shows normal SHG emission from the nanowire. (Inset) Scanning electron microscope image of gold pentamers with a single nanowire.[40](b) Multi-quantum well exposed to the plasmonic field of an offset cross antenna for the efficient generation of SHG [41]

characterization method for SHG in plasmonically enhanced dielectrics. The plasmonic nanostructure used in these measurements, the serrated nanogap, creates a platform for studying the temporal evolution of dielectric nonlinearities under plasmonic exposure with attosecond resolution.

While the progress made in nonlinear plasmonics in the past few years has been promising, there is still a long way to go before we can create active optical circuitry based on plasmonic components. However, recent experiments in quantum nonlinear optics using nanostructured materials have shown promise for generating large interaction efficiencies driven by strong driving fields and coupling strengths.

1.6   The quantum limit of nonlinear optics

So far, all of the nonlinear optical experiments demonstrated here have been classical in nature. In order to drive the efficiencies of these nonlinear interactions higher without necessitating intense excitation sources, we move towards the quantum optical regime, which deals specifically with the regime where classical fields are replaced by photon operators. Figure 1.11a shows schematically how light-matter coupling strength and the photon number define different regimes of linear, classical and quantum optics.[43] The exper-
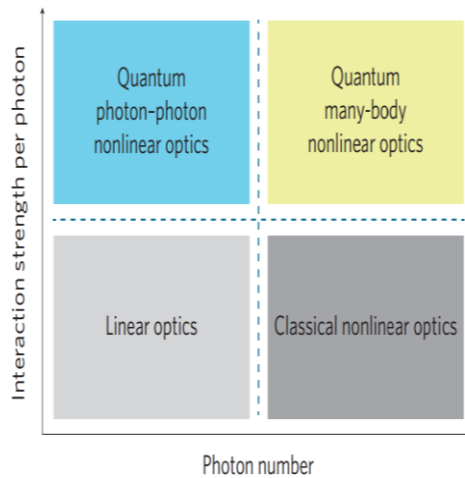
Figure 1.11: (a) Characteristic regimes of nonlinear optics with photon number and interaction strength between photons. [43]

iments demonstrated in chapter 4 of this dissertation build on a robust field of quantum many-body nonlinear optics by introducing quantum coherent control with electron-beam excitation sources in lieu of photonic excitations.

1.6.1 Second-order correlation functions and quantum light sources

Throughout this dissertation we describe the quantum coherent dynamics of nanoscale systems by analyzing thevsecond-order correlation measurements of the cathodolumines-cence (CL) generated by an electron beam in a scanning transmission electron microscope. These measurements determine the temporal statistics of a light source in terms of $g^{(2)}(\tau)$ which can be defined as [44, 45],

$$g^{(2)} = \frac{\langle \hat{a}^\dagger(t)\hat{a}^\dagger(t+\tau)\hat{a}(t+\tau)\hat{a}(t)\rangle}{\langle \hat{a}^\dagger(t)\hat{a}(t)\rangle^2} \tag{1.19}$$

This quantity represents the coherence of the source over time scales represented by τ. For $\tau = 0$, this can be rewritten as

$$g^{(2)}(\tau = 0) = \frac{\langle \hat{n}(\hat{n}-1)\rangle}{\hat{n}^2} \tag{1.20}$$

This correlation can be evaluated for an arbitrary input, $|n\rangle$, to show that

$$g^{(2)}(0) = \frac{n(n-1)}{n^2} \tag{1.21}$$

For a single photon state, $n = 1$, this leads to $g^{(2)}(\tau = 0) = 0$. [17]

In order to define the limitations on classical light sources, we can rewrite equation 1.19 as,

$$g^{(2)}(\tau) = \frac{\langle I(t)I(t+\tau)\rangle}{\langle I(t)\rangle\langle I(t+\tau)\rangle} \tag{1.22}$$

where $\langle I(t)\rangle$ represents the average intensity of the luminescence as a function of time,

and τ represents a delay in time. Classical light sources fall into two major statistical categories: coherent and bunched. Coherent sources such as single-mode lasers exhibit $g^{(2)}(\tau) = 1$. Incoherent light sources, such as thermal sources, have coherence values at $\tau = 0$ that are greater than those at $\tau \neq 0$. [17] This is also known as photon bunching.

The first of two limitations on classical light sources can be derived by representing the time dependence of $I(t)$ as,

$$I(t) = \langle I \rangle + \Delta I(t) \tag{1.23}$$

where $\langle \Delta I(t) \rangle = 0$. If we apply this to the numerator of equation 1.22, we can write,

$$\langle I(t)I(t+\tau) \rangle_{\tau \gg \tau_c} = \langle I \rangle^2 \tag{1.24}$$

where τ_c is the coherence time of the system. So that,

$$g^{(2)}(\tau \gg \tau_c) = 1 \tag{1.25}$$

Conversely, if we take the opposite limit for τ we can write,

$$g^{(2)}(\tau = 0) = \frac{\langle I(t)^2 \rangle}{\langle I(t) \rangle^2} \tag{1.26}$$

By the Schwarz inequality it follows that

$$\frac{\langle I(t)^2 \rangle}{\langle I(t) \rangle^2} \geq 1 \tag{1.27}$$

Using this relationship, we can write the first limitation for classical light sources as,

$$g^{(2)}(0) \geq g^{(2)}(\tau). \tag{1.28}$$

The second limitation can be derived from a slightly different application of the Schwarz inequality. If we use equation 1.23 again to represent time variance in the intensity of the

28

luminescence, we can rewrite the $g^{(2)}$ function as,

$$g^{(2)}(\tau) = 1 + \frac{\langle \Delta I(\tau) \Delta I(0) \rangle}{(\langle I \rangle)^2} \qquad (1.29)$$

Here, the Schwarz inequality takes the form,

$$|\langle \Delta I(\tau) \Delta I(0) \rangle| \leq \langle (\Delta I)^2 \rangle \qquad (1.30)$$

From these two equations, we can derive the second limitation on classical light sources,

$$\left| g^{(2)}(\tau) - 1 \right| \leq \left| g^{(2)}(0) - 1 \right| \qquad (1.31)$$

This relation places a lower limit on $g^{(2)}(\tau)$ that depends on the value of $g^{(2)}(\tau = 0)$. [46, 44, 45]

A common type of quantum mechanical correlation curve has $g^{(2)}(\tau = 0)$ values that are less than $g^{(2)}(\tau >> 0)$. This is termed anti-bunching, and is normally caused by emission from a single atom or defect. The photons from this type of source must be separated in time by the lifetime of the excited state. The type of quantum optical source that will be demonstrated in chapter 4 will exhibit Rabi flopping in the second-order correlation function. [47, 48]

Rabi-flopping in a two-level system can only happen if the system is being dressed by the driving electric field. A variety of quantum systems have been dressed by the electro-magnetic field for frequencies ranging from microwave to visible. [49, 50, 51, 52] Dressing a two-level system with an optical field in this way results in new eigenstates that are the entangled states of the emitted photon and driven quantum system. The Rabi flopping described in chapter 4 is the first evidence for an electron-beam dressed system, enabling nanoscale quantum state preparation in an electron microscope.[53]

1.6.2 Quantum optical behavior of nitrogen vacancy centers

Nanoscale materials and structures designed to work with low photon numbers must exhibit strong interaction efficiencies with the incoming beam in order to generate strong nonlinear signals. For these experiments, we chose a nanoscale excitonic system that has already demonstrated quantum nonlinear behavior under optical excitation, the nitrogen vacancy, NV, center. [43]

Photoluminescence studies have shown that NV centers in diamond are single-photon sources with a near zero probability of multi-photon emission. [55] Recent studies on the cathodoluminescence of a single NV center have also shown anti-bunching[56], whereas, cathodoluminsecent studies on NV center ensembles have shown photon-bunching statistics.[57]

Figure 1.12a shows an atomic force microscope image of a single diamond crystal with NV center defects placed near a silver plasmonic nanowire.

The enhanced recombination rate for the plasmonically coupled diamond nanopar-
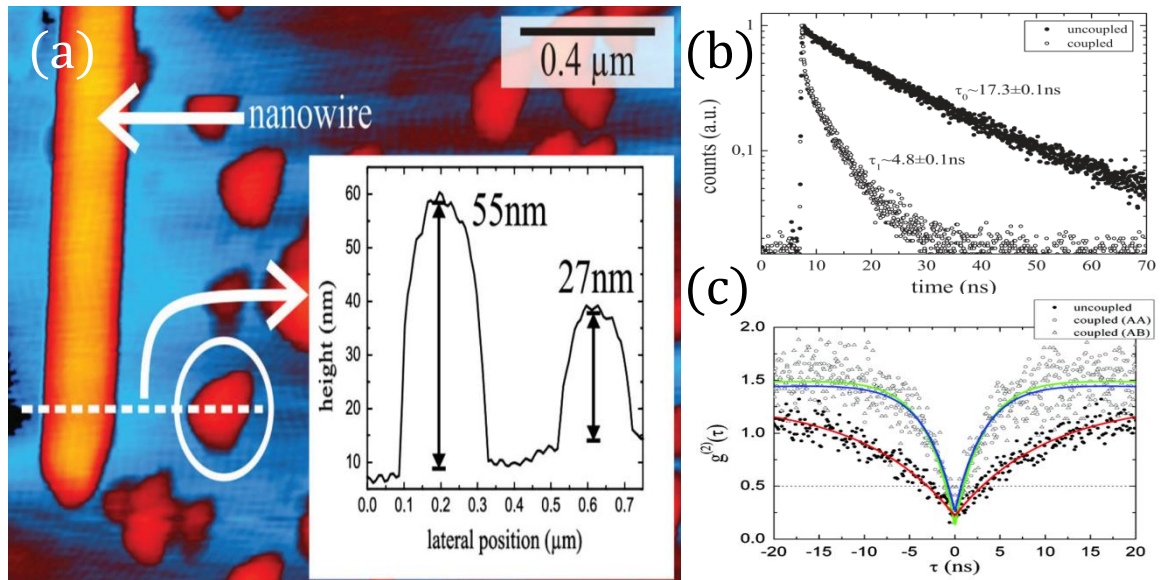
Figure 1.12: (a) Atomic force microscopy image of a single silver nanowire placed with one end approximately 200 nm away from a diamond crystal with nitrogen vacancy center defects. (b) Fluorescence lifetime measurements of the diamond crystal with and without plasmonic coupling. (c) Second-order correlation measurements on the diamond crystal with and without plasmonic coupling.[54]

ticle, as seen in figure 1.12b, is a result of the Purcell effect driven by the plasmonic near field.[54] This system serves as an efficient single-photon source as indicated by the second-order correlation measurements shown in figure 1.12c. [54] Since a single NV center is saturated by one photon, it effectively separates the radiated photons in time by the lifetime of the defect state, resulting in the emergence of anti-bunching.

Optically driven NV centers have been well characterized both as single photon sources in the weak-driving limit [58, 59, 60, 61, 62] and as dressed systems in the strong driving limit.[63] NV centers and other two-level systems have also been characterized in the weak-coupling limit under electron-beam excitation, but no work to date has demonstrated electron beam dressed states. [56, 57] Figure 1.13b shows anti-bunching for a single NV center driven by an electron beam. The work described in chapter 4 provides the first evidence for the electron beam dressing of two-level systems.
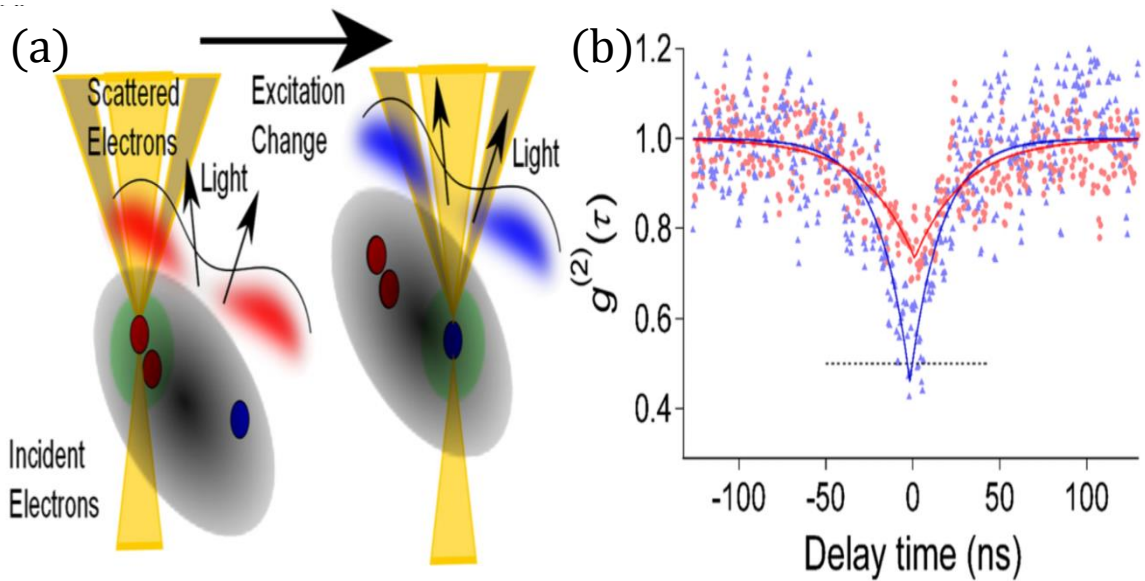
Figure 1.13: (a) Electron beam focused in two NV centers at the same time (left) and a single NV center (right). (b) Second-order correlation curves measurements from multiple NV centers (red) and a single NV center (blue).[56]

Chapter 2

The Archimedean nanospiral

The past decade has seen several plasmonic geometries presented for the enhancement of particular nonlinear optical phenomenon. These advances are slowly paving the path toward nanoscale devices capable of manipulating optical signals using either electron or photon based excitations. An efficient means of controlling and manipulating optical signals using plasmonic antennas holds promise for the creation of optical analog circuitry that can run entirely free from traditional electrical currents. In this chapter we will present groundbreaking measurements on the Archimedean nanospiral as a plasmonic architecture. The lack of inversion symmetry of the nanospiral is shown to create stronger second-order nonlinear susceptibilities than any other fully metallic plasmonic system reported to date. The rotational order of the spiral is also shown to contribute to the polarization responsiveness of nonlinear signals from the nanospiral. We continue to experimentally verify the electric field profiles of the nanospiral plasmon and their contributions to far-field emission. Overall, we expand on previous research involving the nanospiral to show that it is not only a useful plasmonic toolbox for linear optical phenomenon, but also an efficient plasmonic element for nonlinear optical interactions in a low-volume metasurface geometry.

2.1 Background of the plasmonic nanospiral

The Archimedean nanospiral stands out from the mass of planar plasmonic geometries for its potential as a single particle toolbox for several optical interactions. The linear properties of this nanoparticle have yielded results in two-dimensional chirality and complex polarization responses. The breaking of inversion symmetry coupled with the chiral nature of this single contiguous particle generate unique near-field electromagnetic patterns that can be exploited for both the linear and non-linear regime of optical interactions.

The Archimedean nanospiral is a spiral where each arm is spaced an equal amount from it neighboring arm regardless of its position. It can be defined by the equation

$$r = a\theta + b \qquad (2.1)$$

Where r is the radius of the nanospiral arm, θ is the angle, and a and b are constant coefficients. It can also be intuitively defined by four geometric parameters, as illustrated in Figure 2.1a, by winding number, arm width, arm spacing, and thickness. Typical dimensions for a nanospiral with a winding number of 4π that are designed to have plasmon resonances in the optical and near-infrared (NIR) band are arm spacings of 60 nm and arm widths of 40 nm. These nanospirals are fabricated in large arrays of gold particles using EBL. Gold is an ideal material for the plasmonic experiments presented here due to its high charge carrier concentration and mobility. Gold also has a resistance to environmental degradation which allows for repeatable measurements on the same nanoparticle arrays over an extended period of time. A scanning electron microscope (SEM) can be utilized to
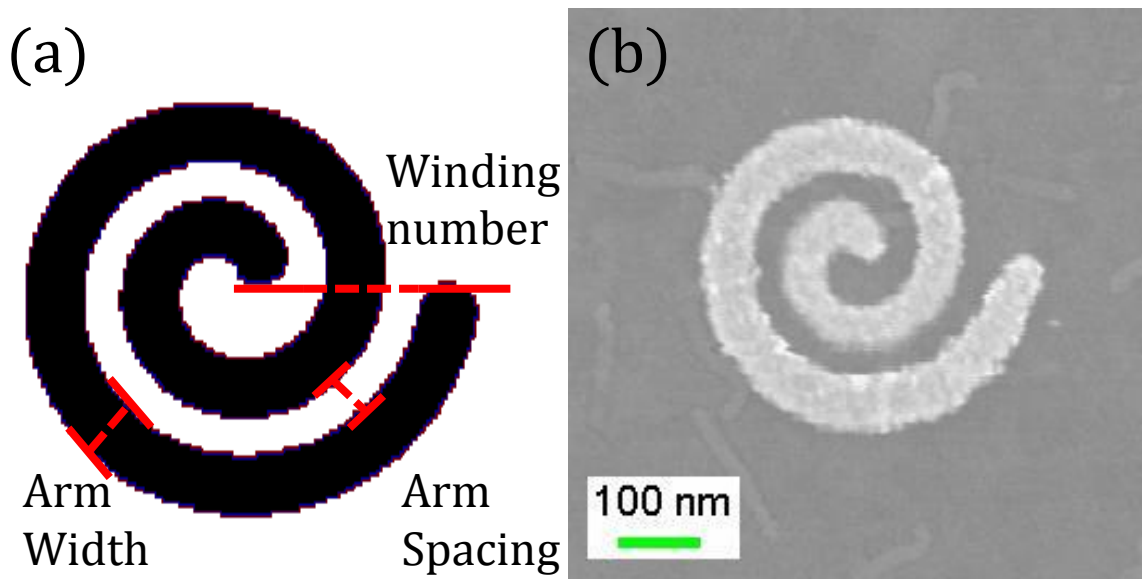
Figure 2.1: (a) Nanospiral geometry layout and parameters(b) Scanning electron microscope (SEM) image of a gold nanospiral fabricated using EBL. Winding number = 4π, arm spacing = 60 *nm*, arm width = 40 *nm*, thickness = 40 *nm*.

image these particles, Figure 2.1b. When fabricated in large arrays, typically 10x10 particles or more, optical interactions such as absorption become large enough to detect easily. Fabrication details for these nanoparticles can be found in appendix D.

In order to better understand the nature of the nanospiral plasmon excitation, finite-difference time-domain (FDTD) simulations were used to calculate the profile of the electric field enhancement factors near the surface of the metal. Three striking patterns arose in the plasmonic near-field of a 4π spiral profile corresponding to optical excitations in specific wavelength bands. The simulated extinction spectra shown in Figure2.2 illustrates the spectral position of these wavelengths. The hourglass mode, λ=580 nm, only takes place at one resonance point in this calculation. The other two patterns, focusing, $\lambda =$ 650-950 nm, and standing wave mode, $\lambda = 950$-1300nm, occur at several resonances with
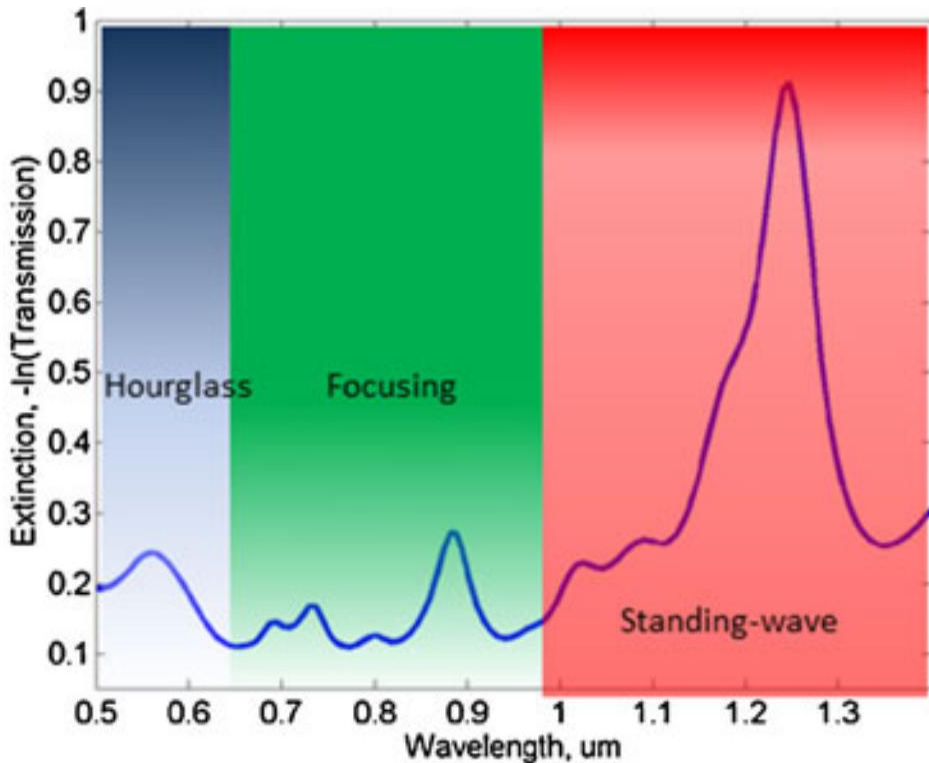
Figure 2.2: Simulated excitation of the 4π nanospiral under plane wave excitation calculated in finite-difference time-domain (FDTD) formalism. Blue shaded region represents the optical band in which the hourglass plasmon mode is excited, green - focusing mode, and red - standing-wave mode. [64, 65]
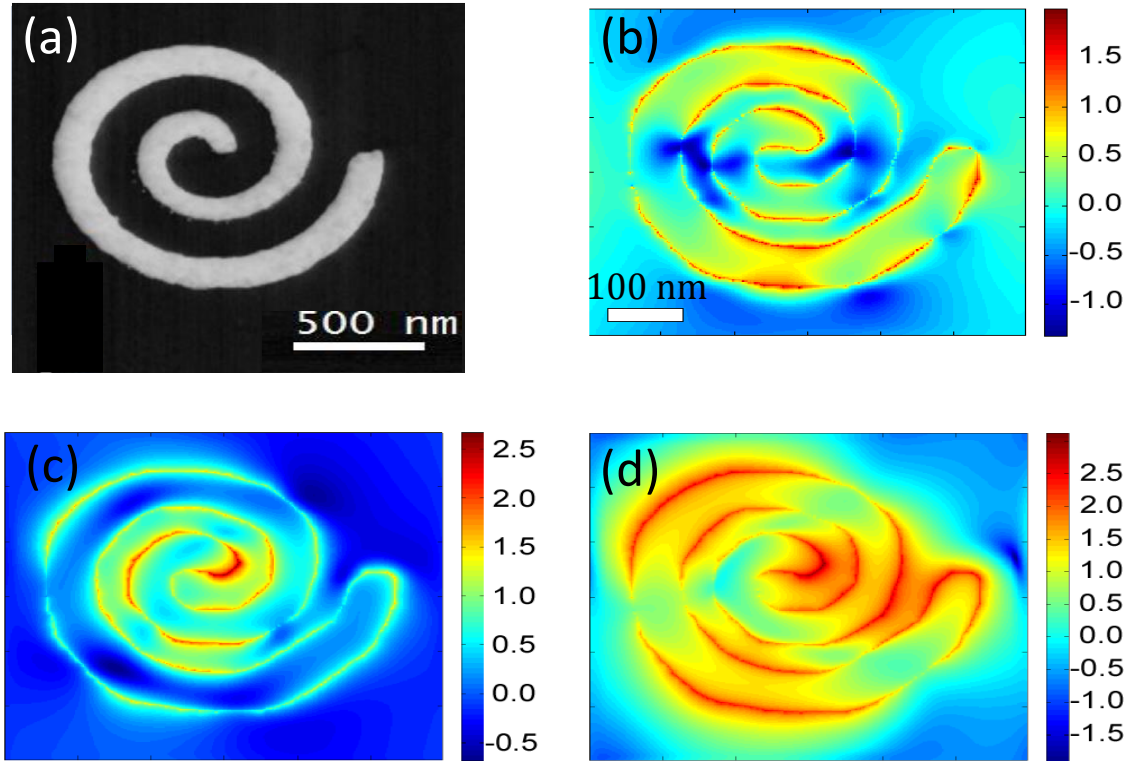
Figure 2.3: (a) High-angle annular dark field (HAADF) image of an EBL fabricated gold nanospiral. FDTD simulations of the plasmonic near field spatial profile of each major band in the nanospiral.(b) Hourglass mode excited at $\lambda = 558$ *nm*. (c) Focusing mode excited at $\lambda = 802$ *nm* (d) Standing-wave mode excited at $\lambda = 1,240$ *nm*[64, 65]

varying degrees of electric field enhancement. These patterns are especially clear at the resonances shown by the black circles in Figure2.2. Their corresponding near-field profiles are calculated in the plane crossing the upper surface of the nanoparticle in Figure 2.3. [64, 65]

While each of these modes holds interest in their specific optical responses, the focusing mode is the one of most interest to the research presented here. The initial attraction to the nanospiral geometry for nonlinear optical investigation is the complete lack of inversion symmetry it has about any axis. As was discussed in the nonlinear optical section of chapter 1, breaking inversion symmetry is a requirement for $\chi^{(2)}$ to not be zero. However, the second term in the second-order polarizability term is $\tilde{E}^2$. This means that we must also harness the electric field enhancement factors associated with the plasmon. The focusing

mode has the smallest mode volume of any of the three major bands, and, consequently, the largest electric field as well. This is the optical band that is most promising for second-harmonic generation.

2.2 Experimental methods

2.2.1 SHG detection and analysis

The experimental results on the SHG conversion efficiency of the Archimedean nanospiral were taken with the setup illustrated in Figure 2.4. The excitation source used to measure the SHG conversion efficiency of planar arrays of the Archimedean nanospiral was an ultrafast laser manufactured by Kapetyn Murnane Laboratories. This was a Ti:sapphire oscillator with an output spectrum centered at 800 *nm*. The laser output pulse width was approximately 50 *fs* in duration before pulse compression.

The oscillator beam was directed through a 128-pixel, double-mask, spatial light modulator (SLM, Biophotonics Solutions) that uses multiphoton intrapulse interference phase
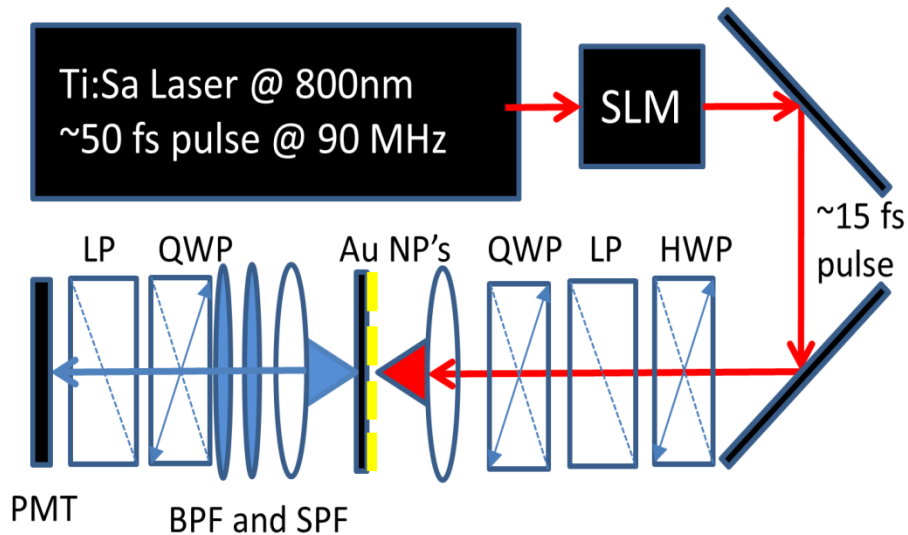
Figure 2.4: Experimental setup used for detecting second-harmonic generation from plasmonic nanoparticles. QWP quarter-wave plate. LP linear polarizer. HWP half-wave plate. BPF band pass filter. SPF short pass filter. SLM spatial light modulator.

scanning (MIIPS) to compress the 50 fs oscillator pulse to a transform-limited duration of 15 fs.[66, 67] The laser pulse was focused on to the nanospiral array using a lens with a numerical aperture of 0.35 to create a focal spot size of 10 μm. This was characterized using the knife edge technique. The maximum energy per pulse was 0.33 pJ at a repetition rate of 82 MHz and was varied using a half-wave plate and linear polarizer combination. After passing through the nanospiral array, the fundamental (800 nm) was filtered out of the signal using a short-pass filter centered at 625 nm and a band-pass filter centered at 400 nm. The SHG signal produced by the nanospirals was detected using a solid-state photomultiplier tube (PMT) (Hamamatsu, RU-9880U-110) in connection with a photon-counting system (Stanford Research Systems). The polarization state of the nonlinear emission from the nanospiral was analyzed using either a linear polarizer or a quarter-wave plate placed in front of the detector.

2.2.2   FDTD simulation of the near field

In order to connect the spatial profile of the near-field resonance of the nanospiral plasmon, FDTD simulations were made under various optical excitation conditions. All of the FDTD simulations shown in this chapter were made using periodic boundary conditions in the $\tilde{\mathbf{x}}$ and $\tilde{\mathbf{y}}$ directions that were spaced to simulate the dimensions of the nanospiral array. Two out of phase plane waves were used to simulate circular polarization. Details on using FDTD simulations for calculating the spatial profile of plasmonic resonances can be found in Appendix A.

2.2.3   Cathodoluminescence characterization of the near field

Experimentally verifying these spatial profiles associated with the nanospiral presents some unique challenges. Most near-field measurements techniques for plasmonic structures require a perturbation to the system. One popular method is known as near-field scanning optical microscopy, NSOM, where a tip is placed near the plasmonic surface.

The surface charge distortion on the tip is measured, and a surface charge distribution is inferred from this measurement as a function of the tip position. The problem with this method and several others like it when dealing with a complex system such as the nanospiral, is that one can never be sure what effect the perturbation had on the structure of the resonance.

A reliable method for measuring the spatial profile of plasmonic resonances with nanoscale precision is by observing the cathodoluminescence (CL) from a scanning transmission electron microscope. As illustrated in figure 2.5, an electron beam can be rastered across the surface of the plasmonic antenna while a parabolic mirror above the antenna gathers the luminescence emitted in the direction of reflection. While this emission is only a direct measure of the radiative decay of the plasmon, the strength of the CL with respect to the electron beam position can be directly connected to the local density of states function of
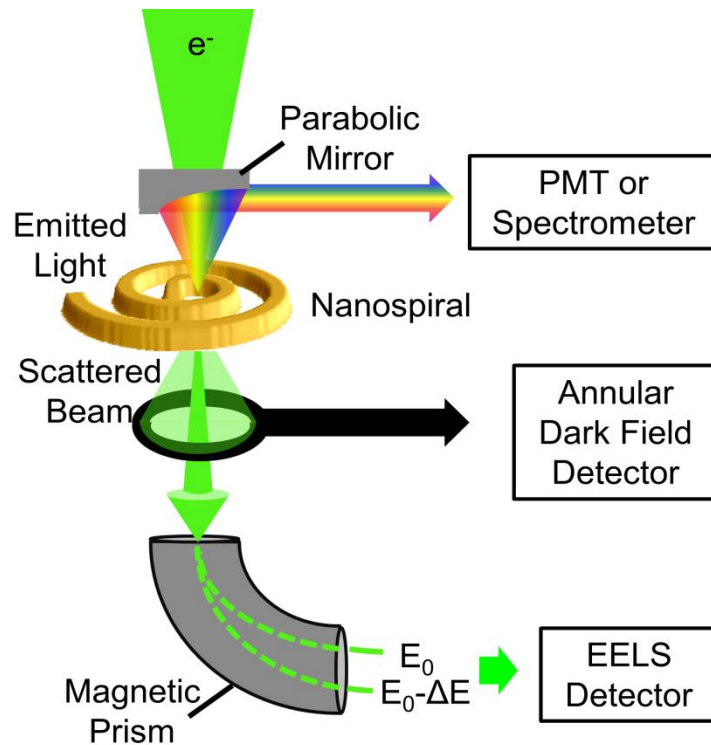
Figure 2.5: Scanning transmission electron microscope with a parabolic mirror for collecting cathodoluminescence (CL). Transmissive detection methods are used to characterize the mechanical structure of the antenna and the energy lost by the electron.

the antenna. Since the interactions take place with one electron at a time that is directly coupling to the dipole moment of the plasmon, there are less perturbations than similar measurements made with a metallic tip interacting with the antenna in the near-field of the plasmon.

A crucial quantity in fully characterizing the near-field behavior of plasmonic antennas is the local density of states (LDOS). This quantity will be discussed in greater detail in chapter 4, but the experiments characterizing the near-field modes of the nanospiral necessitate an understanding of the connection between electron microscopy measurements and the spatial profile of plasmon resonance. The LDOS is defined as the density of states that is available at a given energy for the local electric field. The LDOS has both a radiative and non-radiative portion. CL measurements are a measure of the radiative portion of the LDOS. In order to fully characterize the plasmonic response, CL measurements can be coupled with electron-energy loss which are a measure of the full LDOS. [68]

2.3   Results and discussion

In this section, we describe the second-order nonlinear response from arrays of planar 4π Archimedean nanospirals with sub-wavelength dimensions. The Archimedean nanospiral commends itself as a frequency-conversion architecture due to its unique asymmetry and two-dimensional chiral response. This geometry has a spectrally complex response in the visible to the near-infrared region and spatially differentiated, near-field configurations, as well as selectively enhanced optical response to the polarization states of incident light.[64, 65] These characteristics make the nanospiral a strong candidate for nonlinear optical applications where a broadband plasmonic element is necessary. Unlike plasmonic structures with globally broken symmetry created by modifying or arranging nanoparticles with some inherent local symmetry, [7, 69, 6, 11] the nanospiral has no local axes of symmetry at all so that the nanospiral can generate second-harmonic light from any polarization state. This inherent lack of symmetry therefore makes the nanospiral an attractive
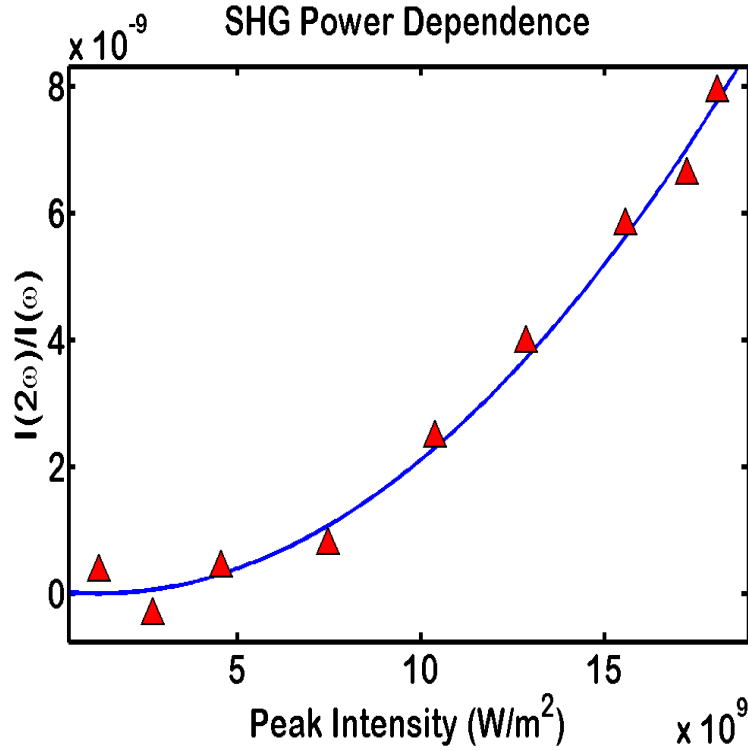
Figure 2.6: Second-harmonic conversion efficiency as a function of the peak intensity of the exciting pulse (red triangles). Second-order polynomial fit (blue solid line).

candidate for nonlinear metasurface elements.

2.3.1 Second-harmonic conversion efficiency

Figure 2.6 shows the measured second-harmonic conversion efficiency from the nanospiral array (red triangles) as a function of the incident laser power at 800 nm with linear polarization. The result is fit to a second-order polynomial computed in Matlab (continuous blue curve) with an R^2 value of 0.9911 as calculated. Extensive computer simulations of the spectral distribution of near-field modes of the nanospiral show that the dominant spatial configuration of the plasmon near 800 nm wavelength is the focusing mode, in which the near-field electromagnetic energy is concentrated in the center of the nanospiral. This makes the focusing mode ideal for harmonic generation, since second-order nonlinear phenomena depend superlinearly on the strength of the electric field. The focusing mode of

the nanospiral provides the spatial concentration of optical energy necessary for efficient conversion to the outgoing second harmonic. The structure of this near-field state also provides a polarization-sensitive template for quasi-chiral properties that are described later in this section.

The SHG measurements were not reproducible at powers greater than 280 W per nanoparticle because laser heating deformed the nanospirals, causing them to lose their asymmetric geometry; the shape of the deformations that occurred due to melting can be seen in Appendix B. Up until the point of deformation, the second-harmonic beam from the nanospirals showed no sign of saturation due to nonlinear down-conversion processes. After deformation, the nanoparticles exhibit neither second-harmonic response nor the other properties of the nanospirals. If the nanospirals were coated in a protective silicon layer as shown in references [7] and [6], the power threshold could be increased beyond an incident power of 280 W per nanoparticle in order to create even higher harmonic-generation efficiencies.
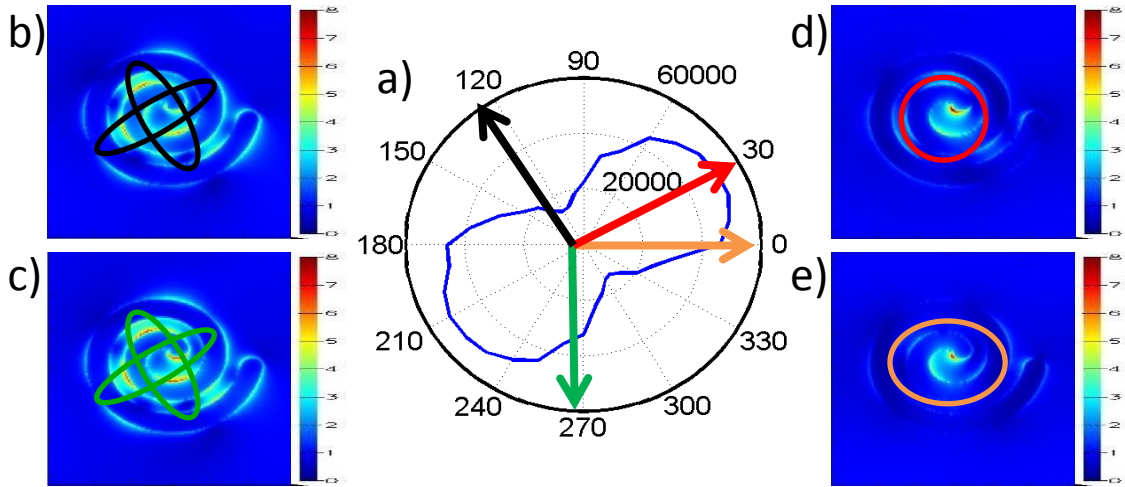
Figure 2.7: a) SHG response the axis of a linearly polarized excitation. 0 degrees corresponds to the line drawn between the beginning and end of the spiral (orange arrow). Maximum SHG signal occurs at 30 degrees (red arrow). Minimum SHG signal occurs at 120 degrees (black arrow). b-e) FDTD simulations of the electric-field strength for four different linear polarization states

41

2.3.2   Polarization modulation

Figure 2.7a shows that the SHG signal is modulated in angle as the axis of linear polarization is rotated with respect to the nanospiral axis. This change in signal corresponds to the changes in the computed near-field electric-field strengths in the center of the nanospiral shown in Figure 2.7(b-e). The maximum SHG signal occurs along the $30°$-$210°$ axis where the peak electric-field amplitude of the plasmon is the strongest; the field strength is distributed largely within the interior of the spiral and follows the rotation of the spiral arm through π radians [Fig. 2.7(d)]. The maximum field strength is higher than for other orientations, and the dipoles excited near the center are spatially coherent. Other orientations of the linear polarization vector correspond to decreasing SHG conversion efficiency due to a dissipation of the strong focusing mode along the exterior regions of the spiral. The electron concentrations are spread out well away from the center, and also create incoherent multipolar resonances throughout the spiral. The second-harmonic radiation produced by these physically separate resonances destructively interferes with itself as expected from SHG produced by a spatially symmetric set of electronic dipole resonators.[11] These symmetry effects are evident from brighter edges of the spiral in the simulations.

The second-harmonic response to circular polarizations, however, more clearly illustrates the effects of intra-particle resonances on the electric field strengths and consequently the SHG efficiency. The polarization dependence of the SHG intensity in Fig. 3 shows that for right-handed circular polarization rotating from the outside of the spiral to the inside - there is a larger enhancement than that observed with linear polarization. When excited with left-handed circularly polarized light the nanospirals show a significantly reduced second-order response. The maximum and minimum SHG signals differ by a factor of four, which occurs for an eccentricity of 0.66, where eccentricity is defined as the ratio of minor to major axis of the ellipse traced out by the polarization vector. This dependence on eccentricity arises because the nanospiral is not perfectly circular. The second harmonic conversion efficiency given by $I(2\omega)/I(\omega)$ - is thus a maximum for right circular polarized
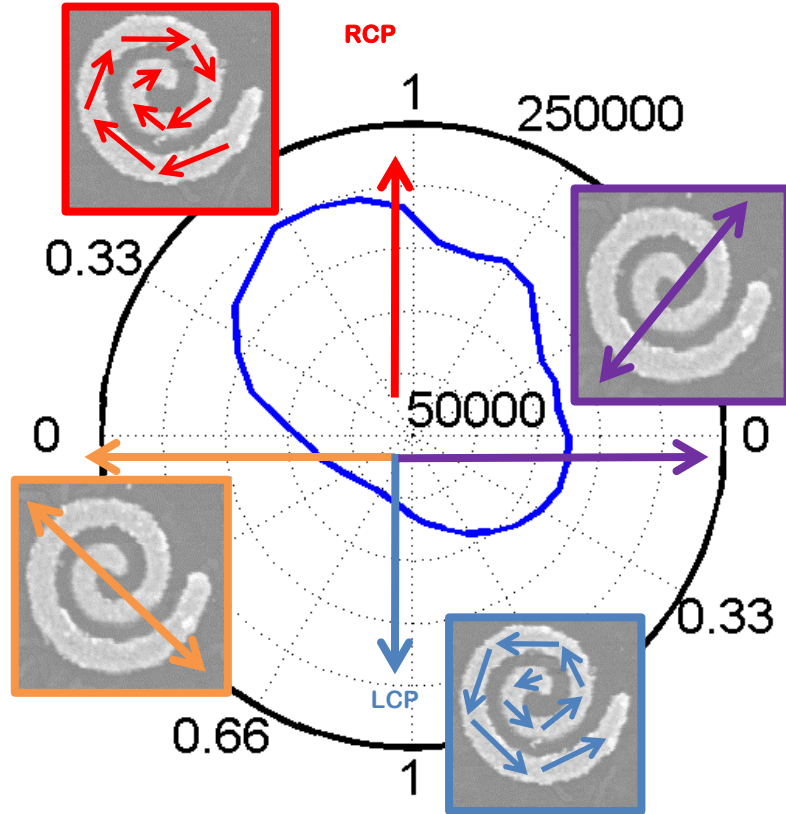
Figure 2.8: Conversion efficiency response to eccentricity and handedness of circular polarization. Horizontal axis corresponds to the two linear polarized states shown by the purple and orange lines. The vertical axis corresponds to completely circular polarizations shown by the red and blue traces.

light and has the value $1.3 \cdot 10^{-8}$.

The nonlinear polarizability that is responsible for second order phenomenon can be written in this case as $P(2\omega) = 2\varepsilon_0 d_{eff}[E(\omega)]^2$ where d_{eff} is the effective second order susceptibility (normalized to the measured efficiency) and $E(\omega)$ is the fundamental pump field. Using a driven Lorentz oscillator model appropriate for electrons in gold, we find that d_{eff} ranges from 15.3 pm/V for RCP excitation to 3 pm/V for LCP excitation. These values are comparable to the d_{eff} measured for tilted gold hemispherical nanoparticles.[6] Even though the nanospiral extinction varies as a function of the incident polarization state, there is nevertheless a finite SHG response to all polarizations. This novel property of the

nanospiral is a consequence of the absence of any local axis of symmetry.

The polarization response of the second harmonic emission is consistent with FDTD simulations shown in figure 2.3. At a wavelength of 800 nm, the focusing mode is excited, concentrating the near-field intensity in the center of the spiral to create a single region of high electric field. Right-handed circularly polarized light assists this electron concentration by driving the electrons from the outer regions of the nanoparticle towards the center. This, in turn, generates increased electric field amplitude and consequently a larger SHG signal. Left-handed circular polarization causes the opposite effect by driving the electrons away from the center of the spiral. Three-dimensional chiral geometries exhibit strong responses to polarization and a geometry that cannot be superimposed upon itself as discussed, for example, in references [70] and [71]. The existence of two-dimensional chirality in plasmonic structures has sometimes been debated, because even thin nanostructures such as the nanospirals in our experiment, which have an aspect ratio of order 16 are not rigorously planar. Nevertheless, quasi-two-dimensional plasmonic nanostructures with chiral boundary conditions in only two dimensions have been shown to rotate linear polarized light and to convert one polarization state to another.[72, 73, 74] This property can be identified as one albeit only one characteristic of a chiral system.

2.3.3 SHG polarization analysis

We now show that the second harmonic generated by Archimedean nanospirals reveals the complex interplay among polarization states that is the hallmark of this quasi-chiral response. The conversion between linear and circular polarizations was investigated by placing a second quarter-wave plate and linear polarizer in the path of the SHG emission. Figure 2.9 (a-c) show the polarization profiles for three types of incident polarization using only a linear polarizer as an analyzer. The dipolar pattern in Figure 2.9 (a) shows that when the nanospirals are illuminated by linearly polarized light, the SHG emission is linearly polarized about the same axis as the exciting fundamental beam. This is not surprising,

because the localized dipolar plasmon resonance responds to all polarizations. When the fundamental beam is right-circularly polarized, as in Figure 2.9 (b), the SHG emission is still linearly polarized, but the SHG axis of polarization is pinned on the axis 135° from horizontal. Lastly, a fundamental beam with left-handed circular polarization, Figure 2.9 (c), does not produce linearly polarized SHG emission at all.

However, the left-handed circular polarization experiment in Figure 2.9 (c) only shows that the emitted light is not linearly polarized; this result could have occurred either because the SHG was circularly polarized or because it was essentially depolarized. To resolve this question, a quarter-wave plate was inserted between the nanospirals and the linear analyzer, which would have converted any circularly polarized light to the linearly polarized state. Since no axis of linear polarization was evident in the analyzed SHG signal, it was clear that left-handed circular polarized light incident on the nanospirals creates depolarized second-harmonic light. While the signal is lower than SHG from linear or RCP light, it is only a factor of four lower than the maximum signal observed from the nanospirals. This behavior seems to be reproduced by the focusing mode simulations shown in Figure 2.10. When the polarization is driving the electrons towards the center of the nanospiral as shown in Figure 2.10 (a), the strength of the electric field is enhanced. The surface charge density of the plasmon must be ordered if it is to maintain the constructively interfering, multipolar resonance condition that will prevent second-order light from destructively interfering with itself.

When the polarization is driving the electrons away from the center of the nanospiral, on the other hand, a disordered plasmon resonance is created that is simulated in Figure 2.10 (b). Depolarization in plasmon emission has been observed in simple nanoparticle geometries having resonances that overlap spectrally and spatially; the coherent emission from sub-wavelength structures may exhibit partial depolarization in various directions depending on the relative phases of the light. [75, 76] The near-field structure of the LCP excitation in the nanospiral shows regions of high-electric field enhancement that are spatially spread

SHG vs. Linear Analyzer Angle

Linear Polarization

a)

RCP

b)

LCP

c)

LCP after Quarter Wave Plate

d)

$1.3 \cdot 10^4 + 1.2 \cdot 10^4 \cos(2 \cdot x)$
$- 623 \cdot \sin(2 \cdot x)$

$1.7 \cdot 10^4 - 780 \cos(2 \cdot x)$
$- 1.3 \cdot 10^4 \cdot \sin(2 \cdot x)$

$1.0 \cdot 10^4 + 2.4 \cdot 10^3 \cos(2 \cdot x)$
$- 261 \cdot \sin(2 \cdot x)$

$5 \cdot 10^3 - 280 \cos(2 \cdot x)$
$- 434 \cdot \sin(2 \cdot x)$
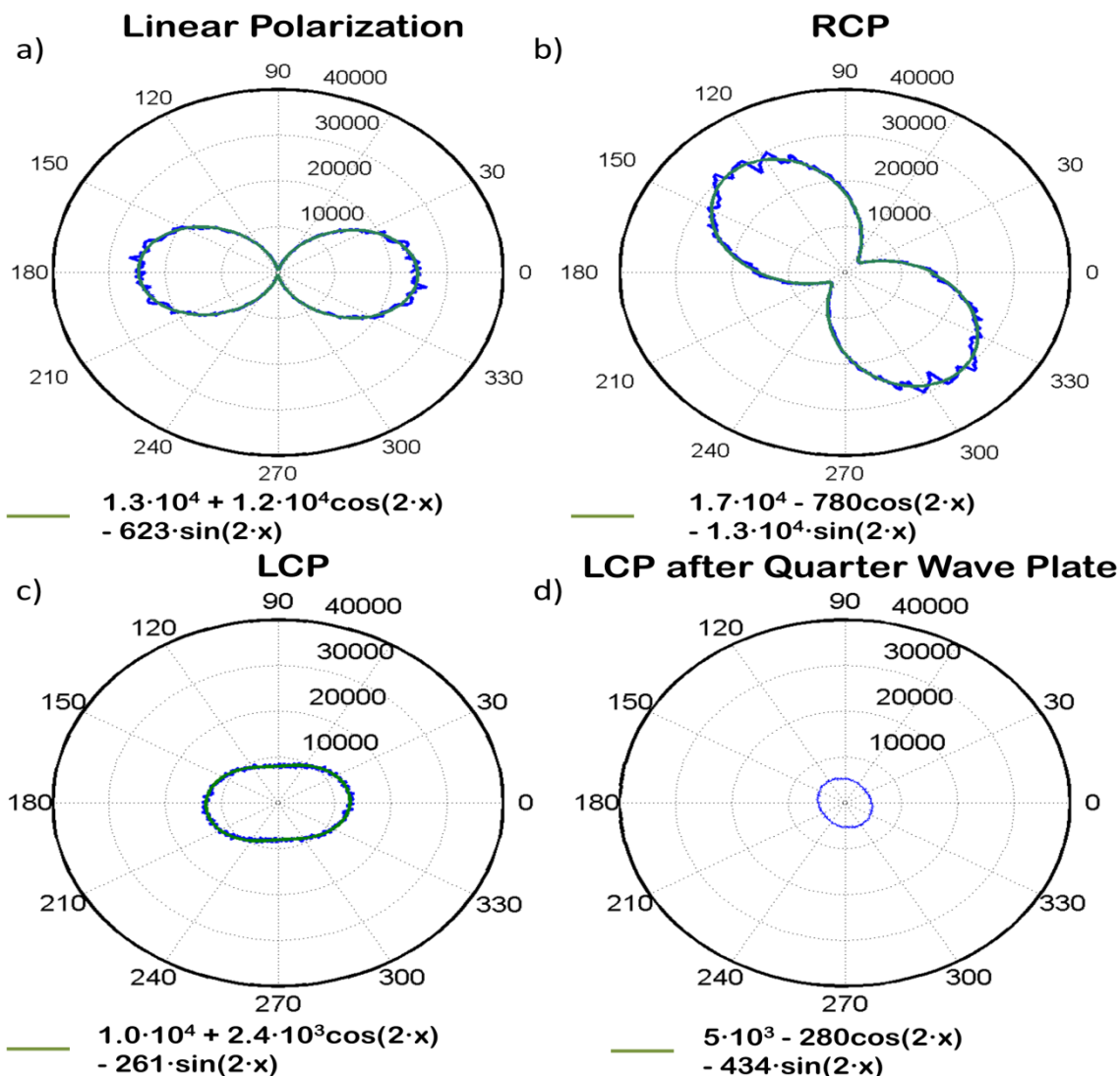
Figure 2.9: Each graph shows SHG as a function of a linear analyzer placed after the nanoparticles a-c) was analyzed using only a linear polarizer. d) used a quarter-wave plate before the linear analyzer. These measurements were fitted to a first order Fourier function to determine the polarization state of the emitted light. a) shows that linearly polarized incident light creates linearly polarized harmonic light that was coaxial with the fundamental. b) shows that right handed circularly polarized incident light creates linear polarized harmonic light with a rotation of the polarization axis by 45 degrees. c) that left handed circularly polarized light creates harmonic light with no dominant axis of polarization. d) shows that the measurements taken in c) was a superposition of all polarizations.
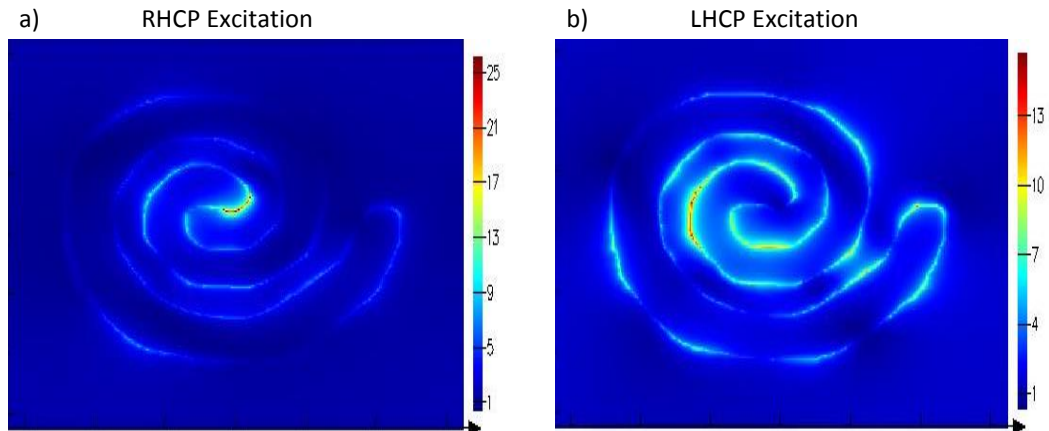
Figure 2.10: FDTD simulations of the focusing mode of the nanospiral using a right-handed circularly polarized excitation (a) and left-handed circularly polarized light (b)

out over larger parts of the nanospiral than in either RCP or linear excitation. This structure contains enough smaller resonances with randomly oriented propagation directions that the resulting SHG emission is completely depolarized. While the polarization conversion observed in nanospirals differs from the polarization rotation that has been demonstrated in other plasmonic geometries[72, 73, 74], the conversion between linear, circular, and depolarized light is evidence of the complex interplay between the second-order response and the near-field structure of the plasmon resonance.

In summary, the Archimedean nanospiral is shown here to produce second-harmonic emission at intensities sufficient for nanotechnology devices. The capacity to modulate the intensity of the SHG by altering the polarization state of the emission, and with efficiencies as large as $1.3 \cdot 10^{-8}$ at 280 W incident power per nanoparticle, the nanospiral is a competitive architecture for all-optical control applications. The nonlinear response to the handedness of circular polarization also reveals the relation between the complex boundary conditions imposed by the spiral shape of the nanoparticle and the plasmon resonance.

Planar frequency-conversion structures are an essential element of plasmonic circuitry. [77] By creating more efficient SHG structures that need not satisfy any phase matching

conditions, and by using localized surface plasmon resonances to further enhance efficiency, we have shown that the nanospiral is potentially significant addition to plasmonic technology. The complex plasmonic resonance structure inherent in the nanospiral, and its complex, but selectable, polarization response, bring additional dimensions to the search for efficient nonlinear plasmonic light sources.

2.3.4 Nanospiral near-field characterization

While previous work have shown strong evidence for the unique near-field profiles of the plasmon known as the hourglass, focusing, and standing wave modes, there was, to the best of our knowledge, no experimental evidence that the nanospiral could support these modes before this work. The nanospirals used in the scanning transmission electron microscope were fabricated on a suspended 50 nm membrane of silicon nitride (SiN). The fabrication details for these nanospirals can be found in appendix D.

Figure 2.11 shows unfiltered and spectrally filtered CL measurements gathered by a PMT made on a 600 nm wide nanospiral with similar dimensions to the nanospiral particles used for SHG generation. The unfiltered CL image, figure 2.11b, contains a superposition of each modes LDOS. We applied optical filters to the CL signal that would filter out increasingly larger portions of the band attributed to the hourglass mode, figure 2.11c-e. The result showed that after the hourglass mode was eliminated, the focusing mode was sufficiently dominate to be seen over the standing wave mode. Figure 2.11e shows the radiative portion of the LDOS that clearly agrees with the FDTD simulation of the focusing mode, figure 2.3c. [64]

An important thing to note here about the hourglass mode is that it is related to the excitation polarization in a different manner than the focusing or standing wave modes. While the hourlgass mode remains structurally the same, it major axis rotates to match the exciting polarization. This relationship is convenient for verifying the mode via CL. Instead of spectrally filtering the CL signal, we filter it based on the polarization of the
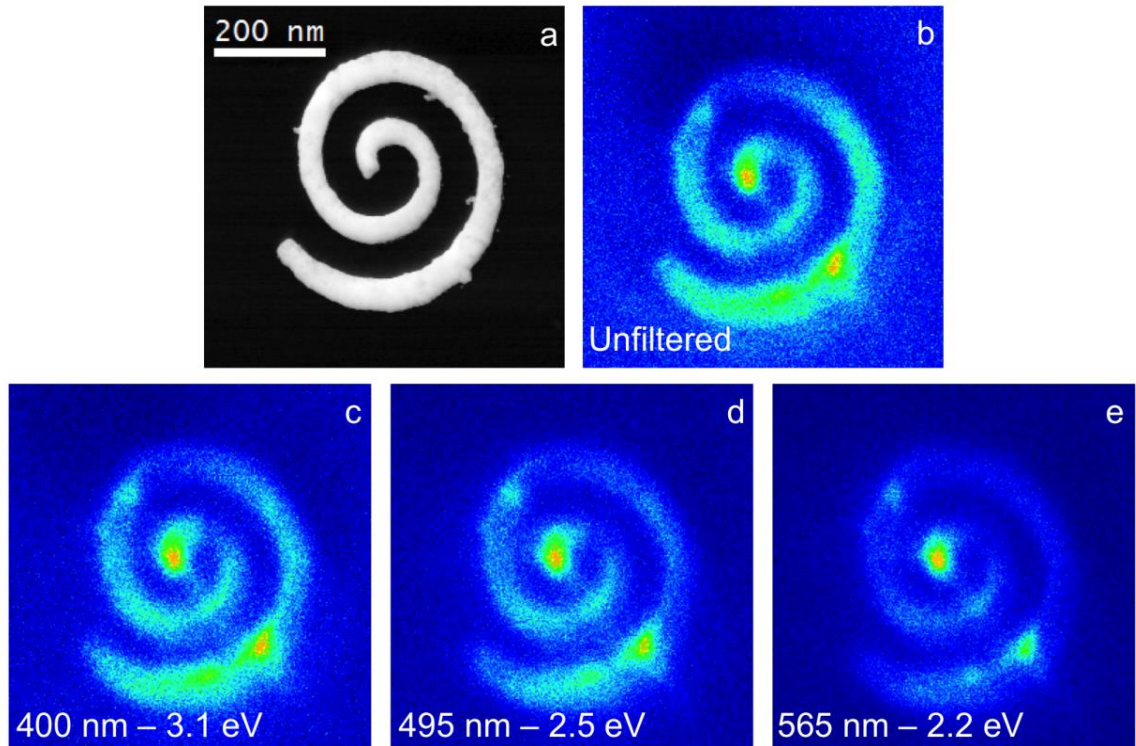
Figure 2.11: (a) Dark-field image of a nanospiral suspended on a 50 nm SiN membrane (b) Unfiltered CL image. (c-e) CL filtered with a (c) 400 nm long pass filter (d) 495 nm long pass filter and a (e) 565 nm long pass filter. The CL image in (e) best matches the focusing mode in simulations

CL signal. Figure 2.12 c-e show the CL image using three different orientations of the filtering polarizer. The near-field map this reveals also matches FDTD simulations shown in previous work. [64]

The standing wave mode of the nanospiral takes place in the infrared. This has proven challenging in the current optical detection scheme of our CL microscope. However, a nitrogen cooled InGaAs detector could easily be used to verify this final near-field profile. Smaller nanospirals could possible shift the standing wave mode into a more accessible band.

Overall, we have shown direct evidence supporting the theoretical work previously performed on the nanospiral. [64, 65] We have also established the direct measure of the radiative LDOS as a mean of determining the spatial profiles of plasmonic antennas with
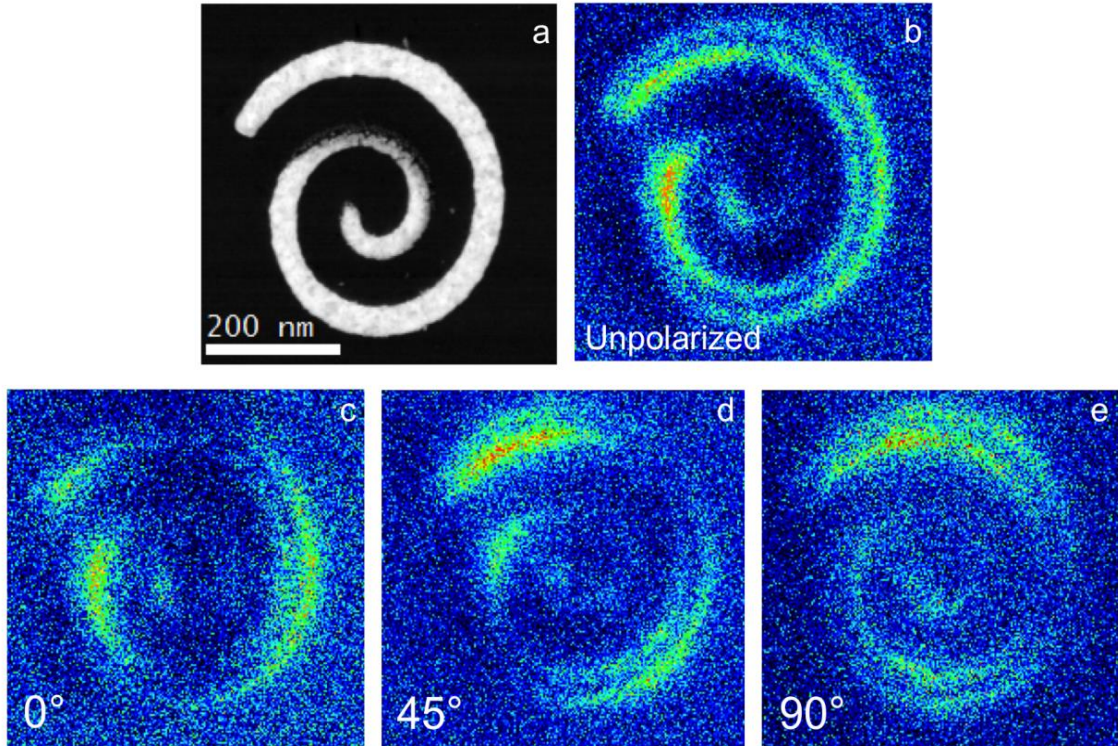
Figure 2.12: (a) Dark field image of a nanospiral (b) Unfiltered CL image (c-e) CL images filtered by a linear polarizer rotated to (c) 0° (d) 45° (e) 90°. The filtered images match the FDTD simulations of the hourglass mode.

nanometer scale resolution. This work is currently unpublished due to an ongoing effort to fully characterize the nanspiral near-field as well as evidence of the two-dimensional chirality shown in the optically induced nonlinear emissions.

Chapter 3

Optical control of SHG in the serrated nanogap

Dielectric materials near the surface of plasmonic nanostructures also exhibit enhanced nonlinear optical responses proportional to the confinement of the electric field.[3, 4, 41, 42] The short excitation lifetime and nanoscale footprint of metasurface devices hold promise for replacing macroscopic nonlinear crystals in biophotonic applications and tunable light sources. While the efficiency of these coupled metal-dielectric systems continues to improve, controlling these systems at timescales that would utilize the ultrashort plasmonic lifetimes remains an obstacle to fabricating nonlinear plasmonic devices that can be used for active manipulation of optical signals. Current plasmonic technology has yet to deliver a method of characterizing and controlling nonlinear signals on the ultrafast timescale.

In this chapter we demonstrate efficient second-harmonic generation (SHG) in a serrated nanogap plasmonic geometry that generates steep electric field gradients on a dielectric metasurface. An ultrafast pump is used to control plasmon-induced electric fields in a thin-film material with inversion symmetry that, without plasmonic enhancement, does not exhibit an an even-order nonlinear optical response. The temporal evolution of the plasmonic near-field is characterized with ~ 100 as resolution using a novel nonlinear interferometric technique. The nonlinear emission arising from the nonlinear response is also quantitatively separated from 2ω signal sources originating from plasmonic effects such as hyper-Rayleigh scattering and two-photon absorption. The ability to manipulate nonlinear signals in a metamaterial geometry as demonstrated here is indispensable both to understanding the ultrafast nonlinear response of nanoscale materials, and to producing active, optically reconfigurable plasmonic devices. The following experiments use poly-methyl methacrylate (PMMA) as a dielectric materials for convenience, but these experiments can easily be expanded to any material that can be deposited in a thin film.

3.1 Plasmonic enhancement of harmonic generation in dielectrics

There have been several iterations of plasmonic geometries designed for the enhancement of nonlinear optical responses of nearby dielectric materials. Some of them can reach impressive conversion efficiencies of order 10^{-6} like one shown in figure 1.10b. In their current state, plasmonically enhanced dielectric materials are capable of taking advantage of the small mode volumes and intense electric fields of plasmonic nanoparticles, but they still do not have the speed of modulation necessary to generate practical on-chip devices for signal manipulation.

Although active control over nonlinear plasmonic interactions has been achieved by
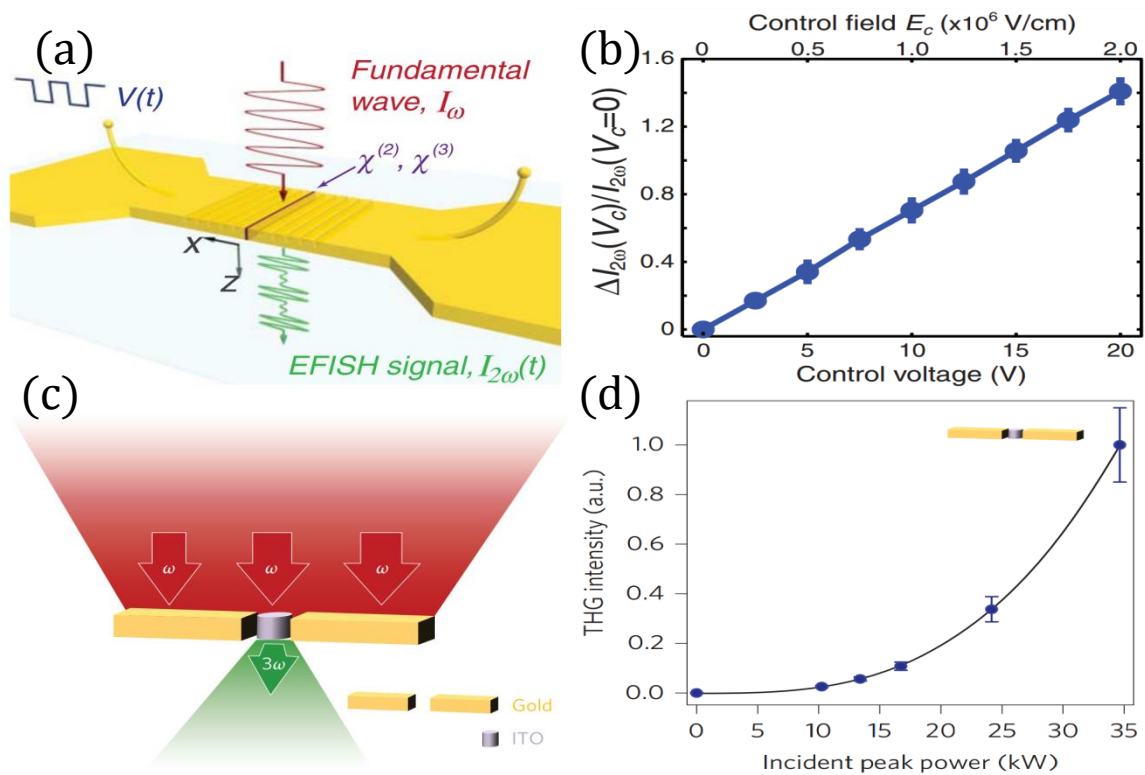
Figure 3.1: (a) SHG generation schematic from a plasmonic grating filled with PMMA. Direct electrical contacts on each side of the grating allow for a direct DC electric field application. (b) Third-harmonic generation enhancement as a function of voltage applied across direct electrical contacts shown in (a).[78] (c) SHG from a ITO particle enhanced by a nanorod dimer. (d) Peak power dependence of the exciting pulse. The black curve shows a third-order polynomial fit to the power dependence.[7]

applying DC electric fields[78, 79], the size of contacts and the frequency response of electrical excitation defeat the principal advantages afforded by plasmonic systems, most notably nanoscale footprints and femtosecond interaction times. Figure 3.1 shows an example of plasmonically enhanced second-harmonic generation from PMMA being actively controlled by a DC electric field applied by direct electrical contacts. While this is an effective means of plasmonically inducing nonlinear emissions from a dielectric material, the modulation speed is incredibly low in comparison with the lifetimes of an LSP. Figure 3.1b shows a nanoscale system for inducing changes in the nonlinearity of indium tin oxide (ITO).

3.2   The serrated nanogap

The experiments presented in this chapter use a novel plasmonic geometry that was specifically designed for the purpose generating steep electric field gradients within a dielectric filled gap. For this purpose we have designed the serrated nanogap (SNG). A scanning electron microscope image of a gold SNG can be seen in figure 3.2a. These particles were designed with a large aspect ratio in order to spectrally separate the plasmonic responses originating from the long and short axes. These particles are similar to a one-dimensional array of bow-tie shaped dimers with an offset between each side equal to half of the arrays period. The side of the particles opposite the gap being physically connected between each triangle gives the SNG a distinct advantage over a bow-tie array. It drastically reduces electric field enhancement factors that would occur outside of the gap. This allows for nonlinear spectroscopy performed on this system to probe only the material within the gap. Figure 3.2b shows the FDTD simulation of the spatial profile of the SNG plasmon. According the simulation, almost all of the electric field enhancement does indeed occur within the nanogap. There is still some residual electric field enhancement at the upper and lower tips of the SNG, but they are minor in comparison the optical energy concentrated within the gap.
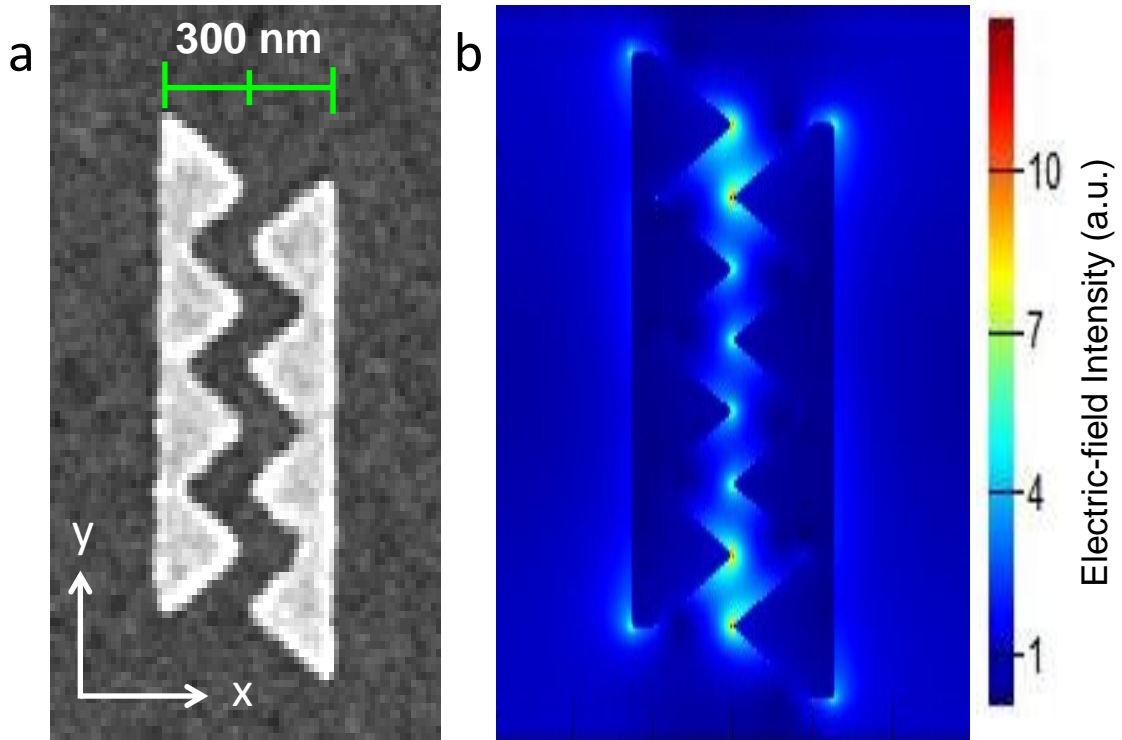
Figure 3.2: (a) Scanning-electron microscope image of a single element of the SNG array (b) Finite-difference, time-domain simulation of the near-field intensity of the SNG plasmon excited by a pulse polarized perpendicular to the nanogap or horizontal to the image at $\lambda = 800$nm.

The SNG particles were designed and characterized to be resonant at 800 nm about the short axis. The aspect ratio between the long and short axis of the SNG is approximately 4:1. This puts the long axis plasmon resonance far enough into the infrared band that we can assume that it does not interact with the optical excitation centered at 800 nm. The SNG dimensions were length = 600 nm, width = 300 nm, gap width = 100 nm, and separation between adjacent teeth points = 150 nm. The nanostructures were fabricated using electron-beam lithography and thermal evaporation of gold. Details on the nanoparticle fabrication process can be found in appendix D. The SNGs were made in arrays with a pitch of 1 m in the x-direction and 2 m in the y-direction. A single array consisted of 82 distinct SNGs covered with PMMA 495A4 electron-beam resist to acquire the data with PMMA filling the nanogaps.
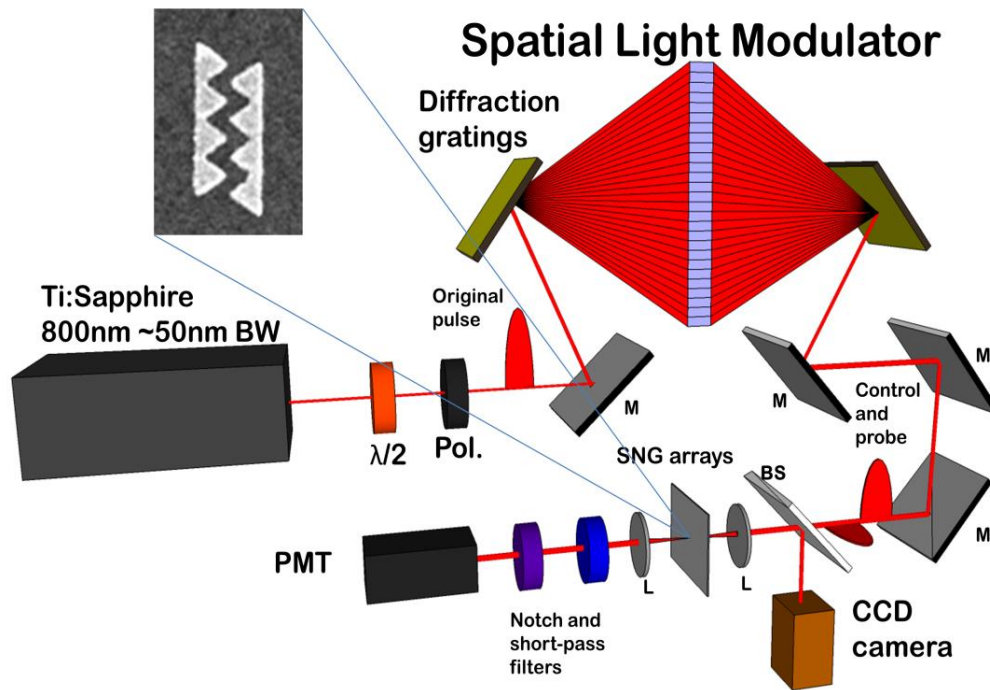
Figure 3.3: (a) A mode-locked Ti:sapphire laser is coupled to a spatial light modulator (SLM) for control of temporal pulse shape and polarization. The SLM generates transform-limited control and probe pulses with orthogonal polarizations and variable optical power and temporal delays between each 30 fs, 800 nm pulse.

3.3   Experimental methods

The experimental setup used throughout this chapter is illustrated in figure 3.3. Output pulses from a Ti:sapphire laser oscillator mode-locked at 83MHz (KMLabs Cascade) were passed through and compressed by a spatial light modulator (SLM) (Biophotonics Solutions Inc.) in order to achieve a transform-limited pulse 3 fs in duration at the metasurface. The laser pulse train was focused onto the SNG array with a numerical aperture objective of 0.35. The beam was then filtered by a set of two optical filters to in order to block signals from the fundamental wavelengths and processes other than SHG. The first was a high pass filter (Semrock FF01-440/SP-25) with a cutoff at 440 nm and an optical density of 0.01 at 400 nm and 5.5 at 800nmm. The second was a band pass filter (Thorlabs FB400-40) with a center wavelength at 400 nm, FWHM of 40 nm, and an optical density of 0.32
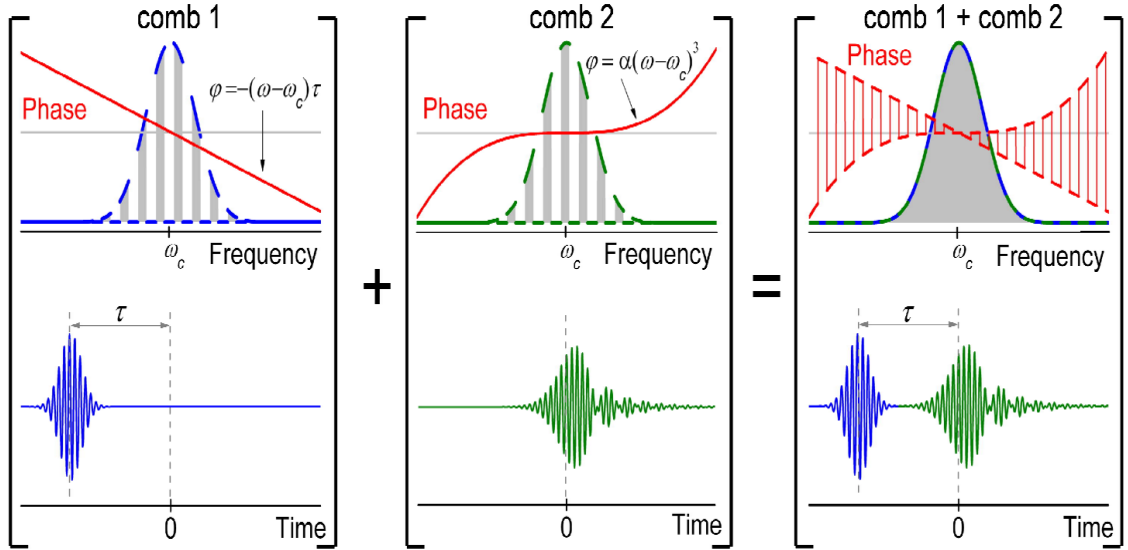
Figure 3.4: Two phase masks applied across alternating pixels of the spatial light modulator in order to generate two temporally separate optical pulses with approximately identical spectral content.[66]

at 400 nm and 4.7 at 800nm. The resulting second harmonic signals were detected using a Hamamatsu PMT (RU-9880U-110) connected to a Photon Counter (Stanford Research Systems).

3.3.1 Spatial light modulation

The SLM consisted of 128 liquid crystal cells. Pulse pairs were generated by creating two phase masks from alternating liquid crystal cells to create identical spectral content as illustrated in figure 3.4.[80] The phase mask was then altered for each measurement to scan the probe across the control field with a resolution of 100 as. In order to reduce the power of the control pulse, separate dummy pulses were created with a vertical polarization and temporal separation from the control of greater than 200 fs. These pulses did not contribute to the SHG signal, as confirmed by a hundred-fold reduction in the SHG signal from a purely vertical excitation. This was done due to the inability to control the relative polarization and amplitudes of the pulses generated by the SLM.

By observing the second-harmonic signal as a function of delay between these two

pulses, a type spectroscopy is performed that is similar to pump-probe. However, it is important to note that in traditional pump-probe experiments, the signal from the pump and probe are completely separated via polarization or propagation paths. This second-harmonic interferometry differs in that both pulses are contributing to the electric fields responsible for the SHG emission. These signals can be deconvolved with the inherently superior temporal resolution of this technique. The major limitation on traditional pump-probe measurements arises from the pump and probe needing to be non-collinear with one another. If they were collinear then the signal from the pump would make it impossible to recover how the probe signal varies as a function of delay. Inevitable mechanical vibrations in every optic the pump and probe interact with after separation introduce noise between the phases of the two beams. This prohibits a temporal resolution of less than 100 fs. The second-harmonic interferometry presented here uses two pulses that are constantly collinear. This coupled with the attosecond scale resolution of the spatial light modulator creates a couple of orders of magnitude improvement on the temporal resolution that we can achieve. The experiments shown here use a resolution of 100 as. A study of the limits of the temporal resolution of this technique was not done, because the shortest phenomenon observed here was on the few femtosecond scale.

3.4   Results and discussion

When the nanostructure is excited by a control laser pulse polarized perpendicular to the gap, regions of high electric field form at the points of the teeth, creating steep electric field gradients within the nanogap. When the nanogap is filled by spin-coating poly(methyl methacrylate) (PMMA) onto the sample and the plasmon is excited using an ultrafast laser pulse, intense electric fields within the dielectric oscillate with a period of approximately 2.7 fs. These oscillations rapidly polarize the electronic structure of the PMMA, causing large, time-dependent changes in its effective second-order susceptibilities.

In order to demonstrate plasmonic control over the SHG signal and isolate the SHG

57
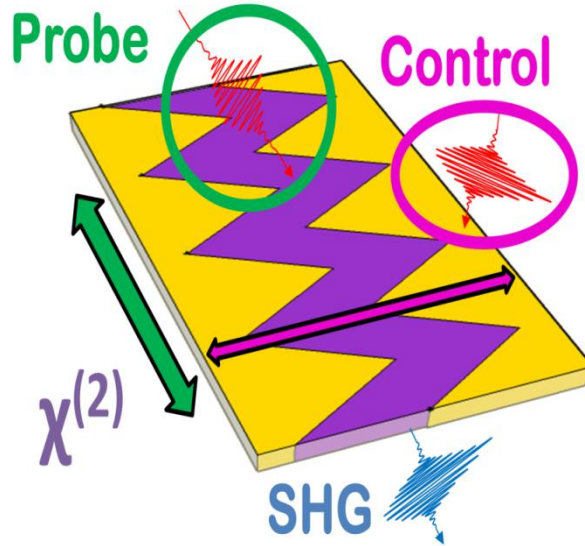
Figure 3.5: (a) The SNG structures are excited with a horizontally polarized control pulse (magenta) and probed with a vertically polarized probe pulse (green), both incident normally on the SNG array.

resulting from plasmonic modulation of the dielectric, we employ a spatial light modulator (SLM) configured as shown in figure 3.3 to generate a collinear, orthogonally polarized pulse pair to simultaneously control and probe the plasmonic system. As shown in figure. 3.5, the control pulse, polarized perpendicular to the nanogap, excites the plasmon, while the second pulse probes the state of the polarized dielectric in the nanogaps. The orthogonally polarized pulses generate an interference response at the second harmonic of the input pulses that is distinctive for structures with and without PMMA. The high aspect ratio (4:1) of the SNG structure does not allow the probe pulse to be absorbed by the plasmon and thereby contribute to SHG arising from plasmon scattering.

3.4.1   Second-harmonic interferometry

We demonstrate plasmonic control of the SHG output in two steps. In the first, the orthogonally polarized pulse pairs are set to equal intensity levels, with a measured average power of 10 mW in both control and probe beams. The interaction of the two beams generates characteristic SHG interference responses that differ according to whether or
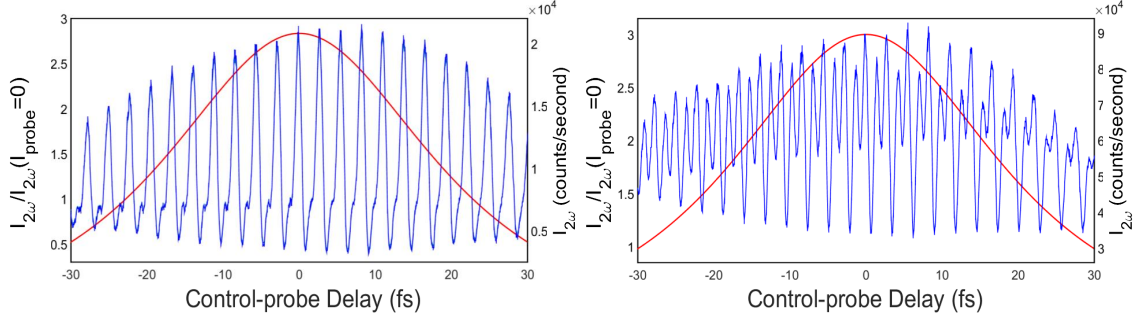
Figure 3.6: (a) SHG as a function of control pulse-probe delay from a bare SNG array. The SHG intensity is normalized to the SHG signal from the control pulse alone. (b) SHG from the same structure filled with the PMMA dielectric. The red solid curve in both graphs represents the temporal envelope of the control pulse.

not there is a thin layer of PMMA in the nanogaps, as shown in figure 3.6. The overall switching contrast for the SHG signal in both cases is 3:1 from peak to valley. The left-hand axes in both figures. 3.6a and b measure the SHG intensity as a function of delay between control and probe pulses normalized to the SHG signal from the control pulse in the absence of the probe.

In figure 3.6a, we see the characteristic SHG interference signature of the bare nanogap array as a function of control-probe delay time, with interference peaks spaced at time delays of τ=nλ/c. As expected, the envelope of the SHG pattern extends beyond the envelope of the control pulse (red curves in figure 3.6, indicating that the SHG signal is temporally broadened. The left and right-hand axes of the graphs show the normalized SHG intensity and the SHG counts for an integration time of 1 s, respectively. The imperfect linear polarization of the pulse pairs generated in the SLM contributed to the background SHG. There is a small shoulder near the intensity minima caused by plasmon-probe interference in the ITO/glass substrate and the air dielectric. Since the evanescent field of the plasmon does not extend deep into the substrate due to the absorption of the gold nanogaps and the ITO layer, this signal is relatively small.

When the SNGs are filled by spin-coating the array with PMMA, on the other hand, the transmitted SHG signal from the SNG array changes dramatically, as shown in figure 3.6b.

Not only does the overall SHG conversion rate, referred to the right hand axes, increase four-fold compared to the bare SNG array, but interference peaks are now observed both at delays of $\tau=n\lambda/c$ and $\tau=n\lambda/2c$. Peaks at $\tau=n\lambda/c$ correspond to constructive interference of the control and probe pulses, as before. Peaks at $\tau=n\lambda/2c$ lie where two 800 nm waves would normally interfere destructively to create an SHG minimum; this second set of peaks results from the optical interaction of the control beam with the probe-pulse-driven dielectric polarization of the PMMA. Due to the continuous pumping of the plasmon throughout the fundamental pulse duration, the envelope of this interference pattern is the result of convolving two 30 fs pulses with the addition of the lifetime of the plasmon, $\sim$10fs.[81] This envelope shows us that the resulting SHG pulse is approximately 70 fs in duration. A small change in the absorption of the plasmon due to the change in the dielectric environment after PMMA removal can be seen in the Supplementary Information (S1). However, the total change in absorption was less than 5%, which is not sufficient to account for the change in SHG conversion efficiencies that follow.

3.4.2 Single optical cycle oscillations

For time dependent external electric fields, the second-order polarizability depends on the second order susceptibility $\chi^{(2)}$ as,

$$P_{2\omega}(E) \sim \chi^{(2)}(E_{plasmon}) \int_0^{\tau_p} [E_{probe}(t+\tau)]^2 dt \qquad (3.1)$$

where E_{probe} represents the probe field amplitude from the pulse polarized parallel to the gap, and $E_{control}$ represents the optical field of the control pulse, polarized perpendicular to the gap, that drives the plasmon field.[82] In order to properly characterize the power dependencies of the plasmon driven SHG from the dielectric, it is important to note that the PMMA dielectric is amorphous ,and therefore, either of these fields can contribute to SHG conversion.

The second step is to demonstrate explicitly that the plasmon field drives the four-fold

enhancement in SHG intensity when the gap is filled with PMMA. This is accomplished by holding the average power of the probe pulse constant at 10 mW, while raising the control-pulse power in steps from 2.5 to 10 mW. figure 3.7a shows the variation in SHG yield during the first optical cycle after zero control-probe delay, normalized to the SHG yield in the absence of the probe pulse. The envelope of a single cycle of the normalized control pulse is shown in red. At 2.5 mW control-pulse power, there is already a low level of plasmon-driven SHG developing even in the minimum of the control pulse field. This rather noisy signal is close to threshold and as a result does not show an obvious coherent relationship to the control pulse.

However, for control-pulse powers at and above 5 mW, a clear oscillatory pattern in the plasmon-driven SHG signal that is nearly, but not exactly, π radians out of phase with the control field and oscillating at 2ω. The maxima in this signal occur at $\tau=n\lambda/2c$, as expected from the data in figure 3.6b; the minima in this signal occur very near $\tau=n\lambda/4c$ and $\tau=3n\lambda/4c$. The minimum at $\tau=3n\lambda/4c$ shows the additional interesting feature that it is not as deep, presumably because at this point the control-pulse intensity at frequency
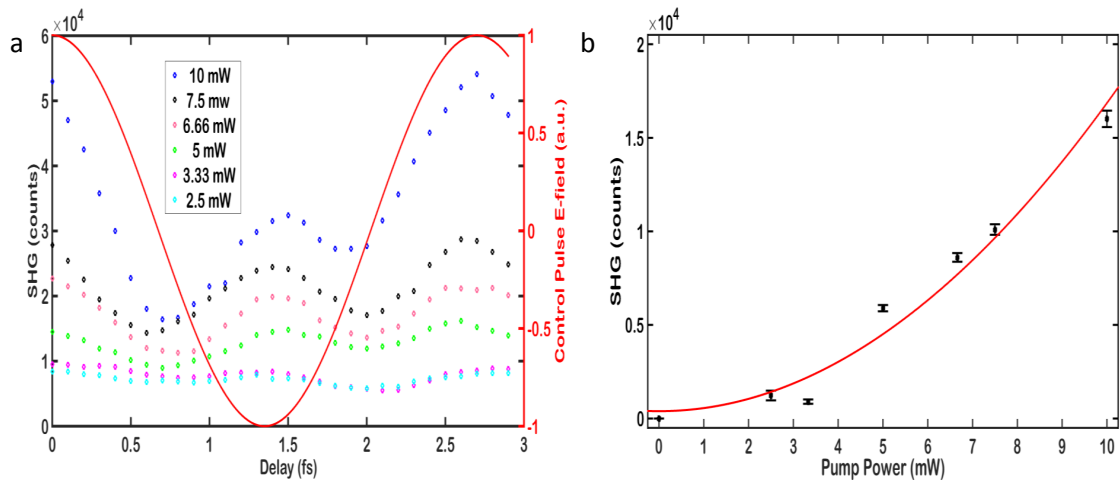
Figure 3.7: (a) A single interference cycle of the SHG signal from a PMMA covered SNG for varying control pulse powers overlaid with the normalized electric field of the control pulse (red). (b) Interference peak height from SHG maximum to minimum as a function of control pulse power. Measured interference heights are fitted to a quadratic function with no linear term with $R^2 = 0.98$.

ω, and with it the plasmon field, is once again increasing toward a maximum. This sub-femtosecond snapshot of of the SHG signal reveals the dynamics of the plasmon interaction with the PMMA with unprecedented temporal resolution. A possible explanation for this distinct asymmetry in the SHG signal is from the response time of the PMMA. Since the nonlinear properties of the dielectric are being altered at optical frequencies, the polarized material does not fully relax before the plasmon scattering signal associated with the τ=nλ/c maxima drives a new plasmon excitation. This effect does not appear for lower control pulse powers because the magnitude of the polarization in the PMMA is not as strong as for a 10 mW control pulse. Measurements of SHG from a PMMA film of equivalent thickness showed approximately 10^2 counts/second at a control pulse power of 10 mW. Changes in intensity for varying control powers were below the noise threshold for this measurement system.

Figure 3.7b shows the peak-to-valley amplitude of the interference intensity, measured as a function of the control pulse power. The lowest values occurring before and after the plasmonic excitation at τ=nλ/2c have a difference in magnitude of $0.5 * 10^4$. A quadratic fit (smooth curve) indicates that $\chi^{(2)}$ depends on the square of the control field for powers well below the optical damage threshold. A model describing this second-order dependence as well as characterizing the response of highly nonlinear materials in this plasmonic geometry remains to be done.

By demonstrating that the SHG efficiency for metamaterial-controlled dielectric scales quadratically with the control field, we have provided a robust platform for ultrafast switchable metasurfaces, efficiently generating nonlinear signals with pulse durations less than 100 fs. The SNG geometry can be used to study the optical properties of thin-film materials at nanometer length scales taking advantage of the polarizing effects of electric fields oscillating at optical frequencies. The SHG spectroscopy enabled by the spatial light modulator makes it possible to separate plasmonically induced second-harmonic light within a dielectric material from light scattered by the plasmon. These experiments can be expanded to

include materials with a larger $\chi^{(2)}$ as well as materials with stronger polarizabilities such as ferroelectrics. This technique is not limited to second-order nonlinearities, which makes it possible to explore third-order nonlinear effects such as phase conjugation and saturable absorption on metasurfaces.

Chapter 4

Rabi flopping in an electron beam driven nitrogen vacancy center

In previous chapters we have shown how we can generate strong nonlinearities by designing the local density of states of plasmonic metasurfaces and dielectric materials. The experiments shown in this chapter continue this theme with one major change in our approach. By studying the photon statistics of an ensemble of NV centers in a single diamond nanocrystal driven by a high-energy electron beam, we enable a combination of high spatial and temporal resolution in the description of nonlinear dynamics in driven quantum systems. In particular, we show Rabi oscillations in an ensemble of NV centers driven by an electron beam. This is, to the best of our knowledge, the first report of a dressed state induced by an electron beam, and it has laid a path toward nanoscale engineering of quantum states in excitonic nanostructures. Most previous research in this area also required cryogenic temperatures in order to maintain coherence over long enough time scales to generate strong coupling between the two-level system and the driving field.[56, 83, 53] This chapter demonstrates coherent quantum oscillations in a nitrogen vacancy center coupled to an electron beam at room temperature. These oscillations not only maintain coherence over tens of nanoseconds, but exhibit Rabi oscillation amplitudes that are larger than any known optically dressed system.

Here we demonstrate room temperature Rabi flopping in a two-level quantum emitter coupled to an electron beam in a scanning transmission electron microscope. This is done by directly measuring the temporal statistics of the cathodoluminescent signal using a Hanbury-Brown Twiss interferometer. Neutral NV center defects in diamond nanocrystals are used as a two-level system. These crystals are placed on a 120 nm silver pillar with a plasmonic response resonant with the NV center zero-phonon line in order to improve the signal-to-noise ratio (SNR). The plasmonic response of the diamond nanocrystal mediates
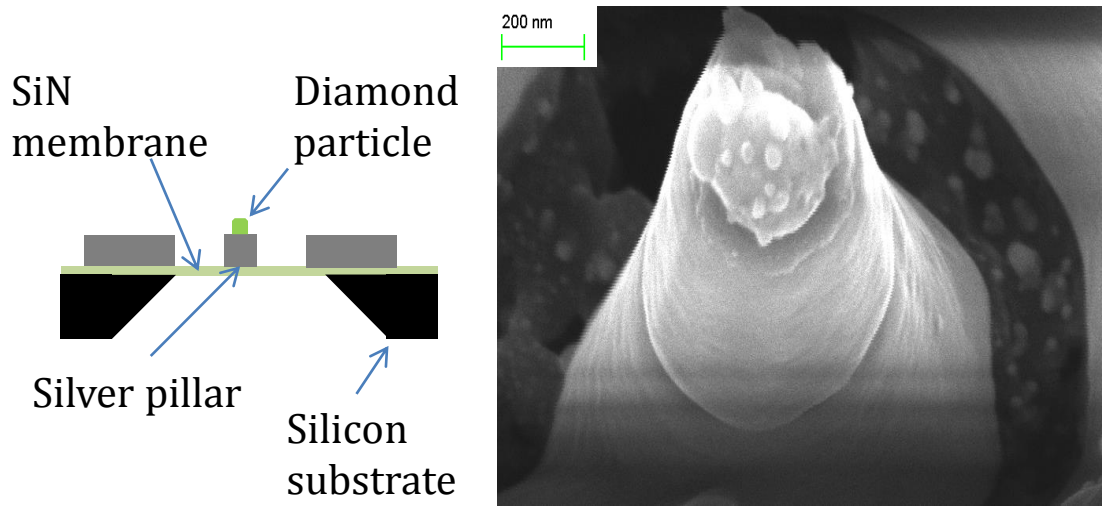
Figure 4.1: Single diamond nanocrystal on silver pillar for CL spectroscopy; the silver nanopillar is carved from a single-crystal silver plate by focused-ion beam milling. Right side is a scanning electron microscope image of a diamond nanoparticle functionalized silver nanopillar.

the simultaneous coherent excitation of multiple defect sites that lead to measurements that appear to be n^{th} order nonlinearities in the second-order correlation functions.

Second-order correlation functions are measured for the phonon-coupled and zero-phonon loss spectral bands. The Rabi flopping observed in these correlation curves violates the Cauchy-Schwarz conditions for classical light sources, described in equations 1.28 and 1.31, providing the first evidence for electron-beam dressing of NV centers. We describe a rudimentary model for electron-beam driven two-level systems in analogy to the existing theory for optical excitations in section 4.2.[83]

Negatively charged NV centers have been identified as potential qubits for quantum information processing, because of the interaction strength between the optically addressable electronic transition and the long-lived spin states.[84] An advantage of using neutral NV defects is that the neutral defect has fewer states to decay through than the negative defect. This means that there is only one radiative transition that needs to be considered when measuring the statistical distribution of cathodoluminescence from these color centers.

4.1 Electronic dynamics of NV^0 and NV^- defects

When optically exciting NV defects, it is possible to address a specific electronic transition by tuning the wavelength of the excitation source. For instance, the non-phonon assisted transitions that are commonly studied for NV^0 and NV^- lie at 575 nm and 637 nm respectively, as illustrated in figure 4.2a and b. The photoluminescence emission from this system will then be dominated by the $^2A - ^2E$ transition because it is the only radiative transition in the system if negatively charged defects are not present. The cathodoluminescent studies shown here excite higher energy transitions such as the $E_P = 30eV$ bulk plasmon mode in addition to the $^2A - ^2E$ transition. [86, 87]

The NV center cathodoluminescence generated in a STEM is shown in figure 4.3. The two main peaks of this emission are the zero-phonon line (ZPL) at 575 nm and the phonon-broadened emission centered around 650 nm. Both of these spectral features come from the transition between the ^2A and the ^2E state shown in figure 4.2b. In the later parts of
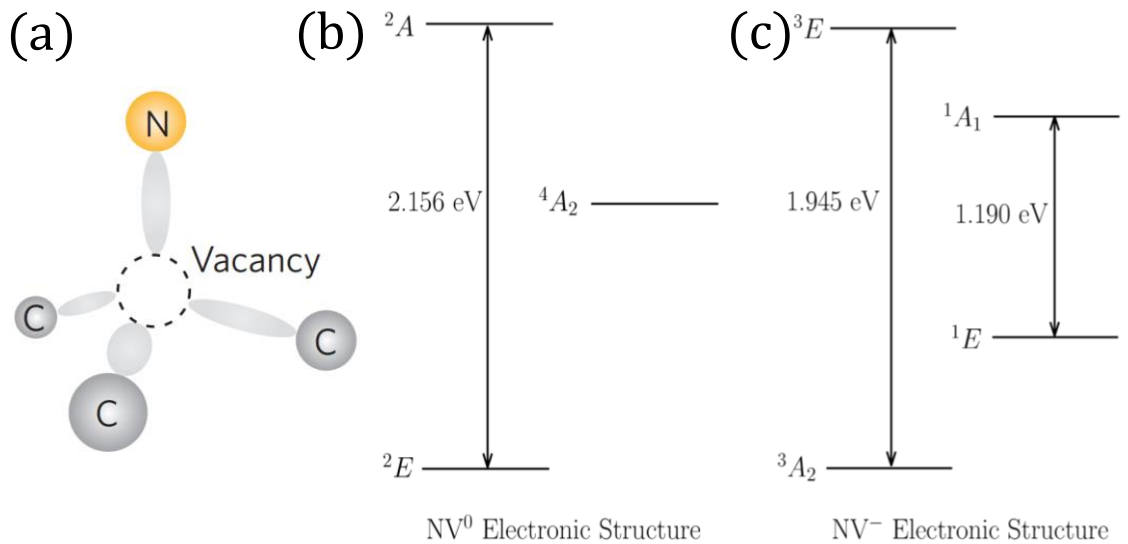
Figure 4.2: (a) An NV center in a diamond lattice consisting of a single nitrogen molecule adjacent to a missing carbon atom.[85] (b) The electronic structure of the neutral defect state (NV^0) contains doublet ground and excited states (^2E and ^2A) along with a quartet excited state ($^4A_2$) (c) The negatively charged defect state (NV^-) contains triplet ground and excited states ($^3A_2$ and ^3E) along with two singlet states (^1E and $^1A_1$)[84]
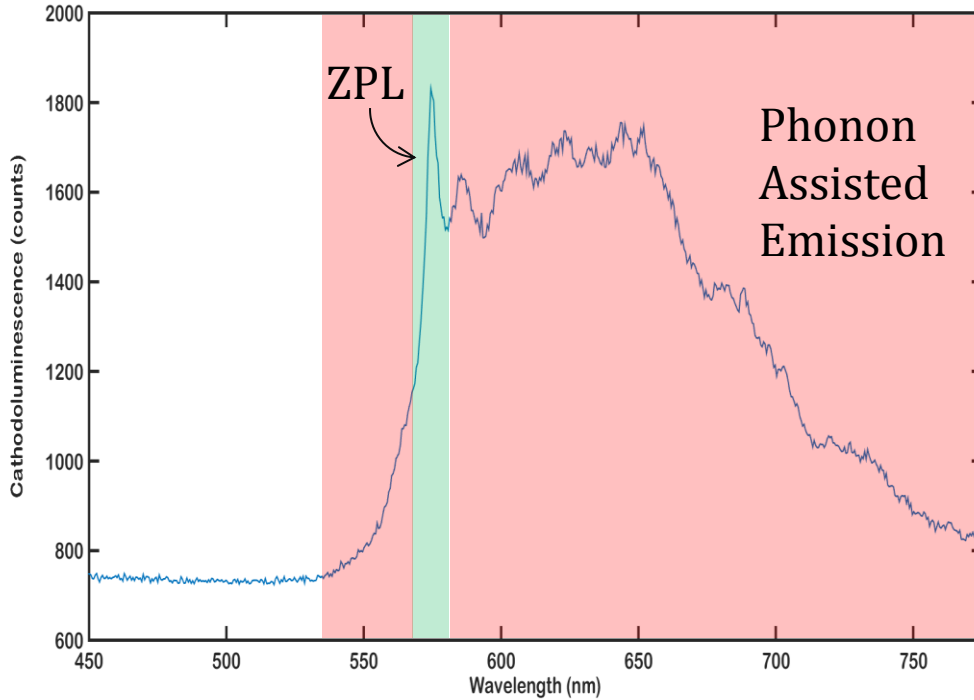
Figure 4.3: (a) Cathodoluminescence spectrum from a 120 nm single-crystal diamond with a high density of NV^0 defects, >1200 defects/particle. The green shaded region is the zero-phonon line (ZPL) and the red-shaded region is the phonon-assisted emission.

this chapter we will examine the effects of phonon scattering on the photon statistics by spectrally filtering out phonon broadened emission, effectively post-selecting the photon statistics of the zero-phonon line CL. The phonon-assisted emission has a much larger bandwidth, $\sim 200\ nm$, than the ZPL, $\sim 10\ nm$, so that the phonon broadened CL exhibits higher signal to noise ratios at the expense of reduced coherence.

The diamond nanoparticles used in these experiments were dropcast onto a 50 nm thick silicon nitride membrane and excited using a VG-601 scanning transmission electron microscope (STEM). Fabrication details for this membrane can be found in Appendix D. The diamonds used here are of a nominal size of 120 nm with greater than 1200 defects per particle and were purchased from Sigma Aldrich®. The diamond nanoparticles were dropcast onto single crystal silver plates in order to increase the signal to noise ratio of the cathodoluminescence. A FEI Novalab 600 Dual-Beam (electron/ion) focused ion beam (FIB) was

then used to carve out a 4μm ring shaped hole around a single crystal. This created a silver pillar of ~ 120 *nm* diameter with a diamond crystal on top as seen in Figure 4.1. The Ag crystal plates were on the order of 1 μm thick and 50 μm wide leaving enough empty space on the 500μm wide SiN membrane for characterizing diamond particles that were completely isolated from silver.

4.2 Rabi flopping in strongly-driven two-level systems

When a two-level system is driven continuously, the probability of the system existing in the excited state varies sinusoidally as a function of time. As shown in the reference [83], this can be seen in the solution of the Hamiltonian for a two-level system driven by a near-resonant sinusoidal potential such as an optical field. The general solution to the time-dependent Schrödinger equation can be written as

$$\Psi(t) = \sum C_n(t)e^{-iE_nt/\hbar}\phi_n \tag{4.1}$$

where $C_n(t)$ represent the time-dependent probability amplitudes. For any real systems that have several possible transitions, this equation cannot be analytically solved. But, when only one transition is taken into account, this solution can be simplified to,

$$\Psi(t) = C_1(t)\phi_1 e^{-iE_1t/\hbar} + C_2(t)\phi_2 e^{-iE_2t/\hbar} \tag{4.2}$$

Under the rotating wave approximation, as described in [88], the solutions to the time-dependent coefficients can be written as,

$$C_1(t) = e^{i\delta t/2}(cos(\Omega_r t/2) - i(\delta/\Omega_r)sin(\Omega_r t/2))$$
$$C_2(t) = i(V_0/\Omega_r\hbar)e^{i\delta t/2}sin(\Omega_r t/2) \tag{4.3}$$

The sinusoidal terms in this solution describes the Rabi flopping with a transition frequency

$\Omega_r = [\delta^2 + V_0^2/\hbar^2]^{1/2}$, where δ represents the detuning between the driving field and the transition wavelength, $\omega_l - \omega_o$, ω_l is the perturbation frequency, ω_o is the transition frequency, and V_0 is the amplitude of the harmonic perturbation.

The semi-classical model used above treats the two-level system quantum mechanically but the driving field classically. While this is sufficient to derive the Rabi flopping frequency, in order to understand the photon statistics of such a system we will quantize the optical field, as shown in reference [47], to derive the second-order correlation function for an optically driven system. While the electron beam cannot be treated as a sinusoidal potential, the diamond plasmon excited by the electron beam can be described in terms of raising and lowering operators. [89, 90, 91] We provide a simple model to outline th differences between the optically driven and electron-beam driven Hamiltonian.

We can write the Hamiltonian for the opticall driven system by treating it as an open system, H_S, coupled to a thermal reservoir, H_R.

$$
\begin{aligned}
H &= H_S + H_R + H_{SR} \\
H_S &= \hbar\omega_0 a^\dagger a + \frac{1}{2}\hbar\omega_0 \sigma_z + \hbar(\kappa_0 a^\dagger \sigma_- + \kappa_0^* a \sigma_+) \\
H_R &= \sum_{k,\lambda} \hbar\omega_k b_{k,\lambda}^\dagger b_{k,\lambda} \quad H_{SR} = \sum_{k,\lambda} \hbar(\kappa_{k,\lambda} b_{k,\lambda}^\dagger \sigma_- + \kappa_{k,\lambda}^* b_{k,\lambda} \sigma_+)
\end{aligned}
\tag{4.4}
$$

where a and $a^\dagger$ are annihilation and creation operators in an incident beam of frequency ω_0 and wave vector k_0. The operators b and $b^\dagger$ fulfill this role for the vacuum state of frequency ω_k and wave vector, k. $\sigma_{z,+,-}$ are pseudospin operators, κ_0 describes the coupling between the incident beam and the two-level system, and $\kappa_{k,\lambda}$ describe the coupling between the two-level system and the vacuum state. The pseudospin operators allow us to treat a two-level system in an electric potential analogously to a spin in a magnetic field.

The derivation of the master equation in the density-matrix picture for this Hamiltonian is well known and can be found in reference [92].

$$\frac{d\rho}{dt} = \frac{1}{i\hbar}[H_S, \rho] + \frac{\gamma}{2}(2\sigma_-\rho\sigma_+ - \rho\sigma_+\sigma_- - \sigma_+\sigma_-\rho) \tag{4.5}$$

In this master equation, γ is the decoherence rate. This equation can lead in general to a large number of coupled equations that can be difficult to solve. However, for the two-level system interacting with the incident field, the density-matrix elements can be described as,

$$\frac{d}{dt}\begin{bmatrix} \rho_{22} \\ \rho_{11} \\ \rho_{21} \\ \rho_{12} \end{bmatrix} = \begin{bmatrix} -\frac{1}{4}\gamma & \frac{1}{4}\gamma & 0 & 0 \\ \frac{1}{4}\gamma & -\frac{1}{4}\gamma & 0 & 0 \\ -\frac{1}{2}\gamma & -\frac{1}{2}\gamma & -(\frac{3}{4}\gamma + 2i\bar{n}^{1/2}\kappa) & -\frac{1}{4}\gamma \\ -\frac{1}{2}\gamma & -\frac{1}{2}\gamma & -\frac{1}{4}\gamma & -(\frac{3}{4}\gamma - 2i\bar{n}^{1/2}\kappa) \end{bmatrix}\begin{bmatrix} \rho_{22} \\ \rho_{11} \\ \rho_{21} \\ \rho_{12} \end{bmatrix} \tag{4.6}$$

where $\bar{n}$ is the average photon number. In order to evaluate second-order correlation functions for this system, we must evaluate the atomic matrix elements using this system of equations. We can define the vector,

$$\tilde{\rho} = \frac{1}{2}\begin{bmatrix} \rho_{22} + \rho_{11} \\ \rho_{22} - \rho_{11} \\ \rho_{21} + \rho_{12} \\ \rho_{21} - \rho_{12} \end{bmatrix} \tag{4.7}$$

Using this vector, we can write the formal solution,

$$\tilde{\rho(t)} = Se^{\Lambda t}S^{-1}\tilde{\rho}(0) \tag{4.8}$$

where S is represented by,

70

$$S = \begin{bmatrix} S_1 & 0 & 0 & 0 \\ 0 & S_2 & 0 & 0 \\ -\dfrac{\gamma^2 S_1}{\gamma^2 + 8\bar{n}\kappa^2} & 0 & S_3 & -\dfrac{2i\bar{n}^{1/2}\kappa S_4}{\frac{\gamma}{4}-\Omega} \\ \dfrac{2i\bar{n}^{1/2}\kappa\gamma^2 S_1}{\frac{\gamma}{2}(\gamma^2 + 8\bar{n}\kappa^2)} & 0 & \dfrac{2i\bar{n}^{1/2}\kappa S_3}{\frac{\gamma}{4}-\Omega} & S_4 \end{bmatrix} \tag{4.9}$$

$$\Lambda = D(0, -\frac{\gamma}{2}, -\frac{3\gamma}{4}+\Omega, -\frac{3\gamma}{4}-\Omega)$$

$$\Omega = (\frac{\gamma^2}{16} - 4\bar{n}\kappa^2)^{1/2} \tag{4.10}$$

where Λ is a 4x4 diagonal matrix in the formal solution to the master equation written in equation 4.8. Once again we can see the origin of the time-dependent oscillations of the state of the two-level system. When Ω is imaginary it's clear from eqns 4.8 and 4.10 that we're in a strongly driven regime exhibiting Rabi oscillations with frequency $-i\Omega$. This defines a dressed state limit that can be induced via strong light-matter coupling, κ, or large photon number, $\bar{n}$.

4.3 Second-order correlation functions and Rabi flopping

We utilize a Hanbury-Brown Twiss interferometer to observe describe quantum coherent dynamics of the CL generated in the STEM. This interferometer generates a second-order correlation function, $g^{(2)}(\tau)$ that exhibits Rabi flopping violating the Cauchy-Schwarz conditions on classical light sources as described in equations 1.28 and 1.31.

The experimental schematic for this experiment is shown in figure 4.4. A beam splitter was used to split the cathodoluminescence signal onto two single-photon counters (Micro Photon Devices© PDMs). A single-photon event timer (PicoQuant® Hydra Harp 400) was used to monitor the time of arrival between consecutive photons, or coincidences, with a resolution of 64 ps. The event timer built histograms over 10^4s to generate the $g^{(2)}(\tau)$ curves presented here. A 2 meter long cable was used as an artificial delay line on detector
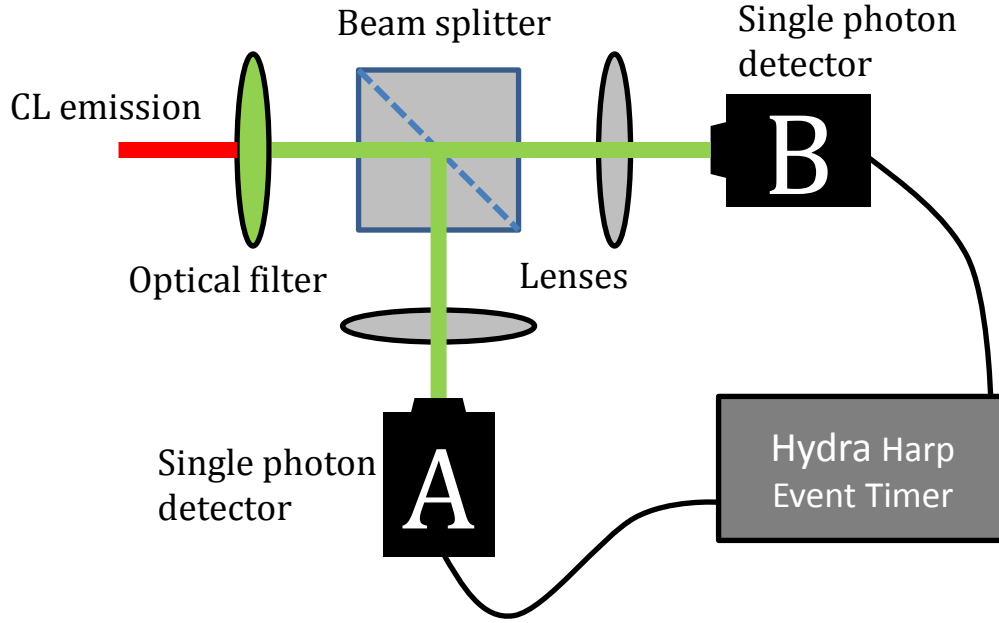
Figure 4.4: Hanbury Brown-Twiss experimental setup.

A, so that $g^{(2)}(\tau)$ could be observed for both the positive and negative values of τ. An optical bandpass filter (Semrock FF01-575/5-25) was used to single out the ZPL for detection for a portion of these experiments. Photon bunching from a well known thermal light source was used to determine the delay point at which $\tau = 0$.

In order to calculate the second-order correlation curve from the raw data, we use a binomial expansion on equation 1.19,

$$g^{(2)} = \frac{2P(2) + 6P(3) + \ldots}{(P(1) + 2P(2) + \ldots)^2} \tag{4.11}$$

where $P(N)$ is the probability of detecting N photons simultaneously. For these experiments, we have sufficiently low intensities that we can make the approximation that $P(1) \gg P(2) \gg P(3)$. From this we can write,

$$g^{(2)} = \frac{2P(2)}{P_A(1)P_B(1)} \tag{4.12}$$

For a completely coherent emission source, the $g^{(2)}$ curve has a constant value of one for all τ. A thermal state has super-poissonian statistics that result in $g^{(2)}(\tau = 0) > 1$ and $g^{(2)}(\tau \neq 0) < g^{(2)}(\tau = 0)$. These two photon distributions are characteristic of classical light sources. Anti-bunched light has a $g^{(2)}(\tau = 0) < 1$ which violates one of the two conditions placed on classical light sources as described in equation 1.28. While $g^{(2)}(\tau = 0) < 1$ can suggest single-photon behavior, until it reaches 0.5 it can easily be explained by an interference between two different coherent states or by a source with a small photon number.

We modify equation 4.4 to include N emitters by replacing σ_- with $\sigma_{-,i}$ and σ_+ with $\sigma_{+,i}$ and summing over all emitters. The results of this model are shown in the second-order
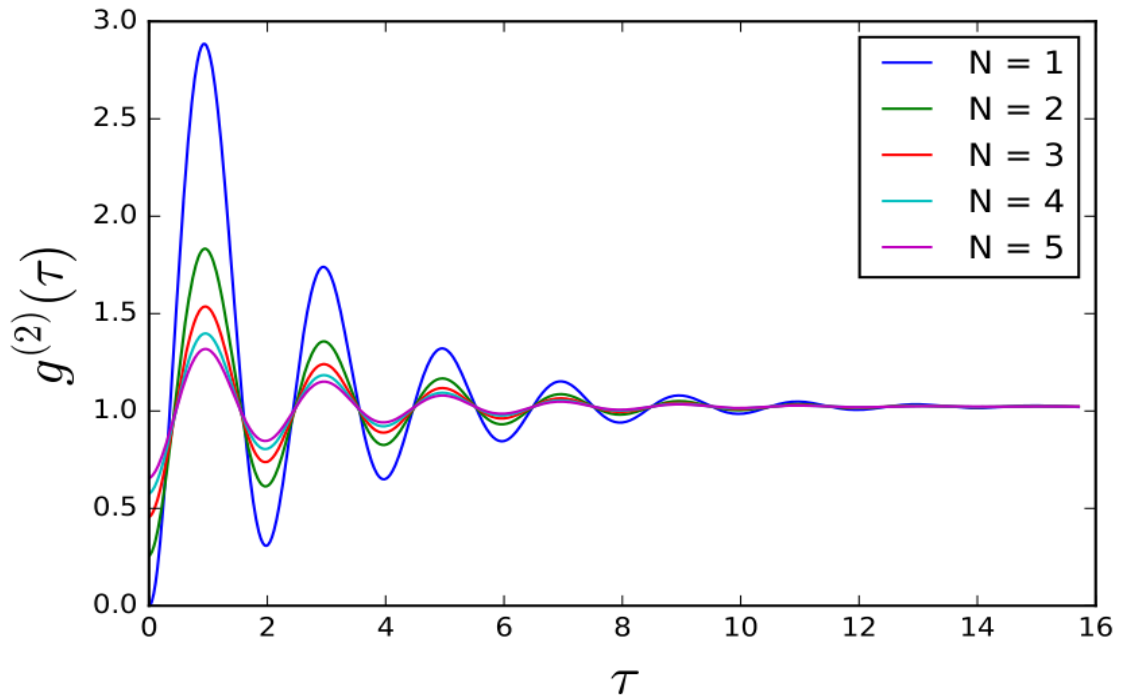
Figure 4.5: Second-order correlation curve for the Hamiltonian shown in equation 4.4 for N excitations. N directly represents the number of NV centers contributing to the cathodo-luminescence signal.

correlation curves in figure 4.5 for one to five emitters. For large numbers of emitters, $g^{(2)}$ approaches one because of the stochastic nature of the light-matter interactions.

The electron-beam excitation used here fundamentally alters the Hamiltonian for optically driven systems described in equation 4.4. The diamond nanocrystal has a known bulk plasmon response at $E_P = 30eV$ that can couple to the electron beam. Whereas each photon in the optically driven system in figure 4.5 can couple to only one of N emitters, the plasmon coherently decays into up to 14 NV centers. Equation 4.4 can be rewritten to describe these dynamics by replacing the photon creation and annihilation operators of the driving field with plasmon creation and annihiliation operators, and by replacing the pseudospin operators with a tensor product of N pseudospin operators describing the N NV centers excited by the diamond plasmon. In the weakly driven regime, this Hamiltonian is consistent with the photon bunching observed in [57] as a result of the simultaneous excitation of N emitters. In the dressed state regime, this Hamiltonian describes an effective N^{th} order nonlinearity resulting in Rabi flopping with amplitudes that increase with N in contrast with optically driven systems. These calculations are being numerically modelled using the quantum toolbox in python (QuTiP) but the results for the electron driven systems are beyond the scope of this dissertation.[93]

4.4   Results and discussion

In order to achieve sufficient SNR, diamond nanoparticles were placed on silver nanopillars on SiN membranes resulting in almost seven-fold stronger CL intensity. The plasmonic enhancement can be seen as a function of electron-beam current in figure 4.6.

The enhanced CL intensity may be a result of Purcell related effects or of additional electron-scattering events or of enhanced NV center excitation mediated by the silver plasmon. The increased recombination rate characteristic of a Purcell effect was not observed in the envelope of the second-order correlation function. This envelope, however, is a measure of the coherence time of the system which is determined by a combination of
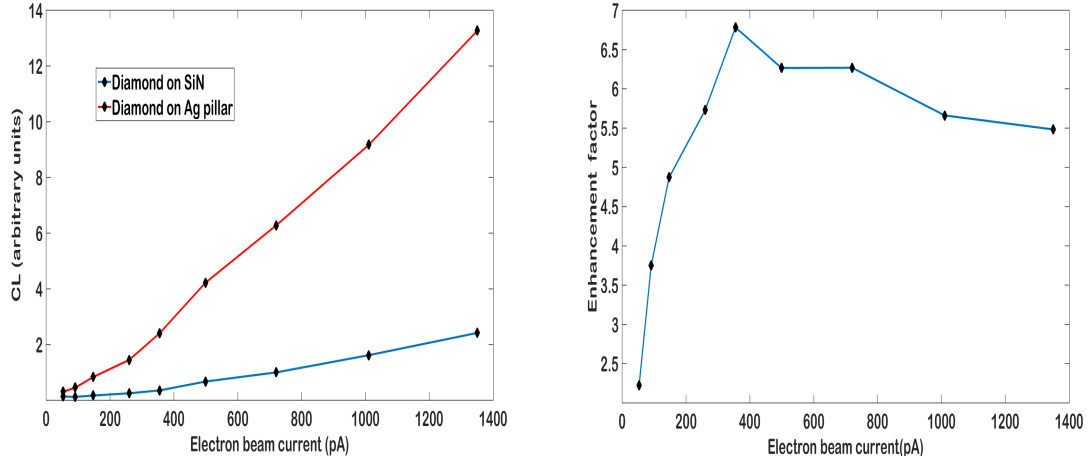
Figure 4.6: (a) Total CL signal as a function of electron beam current for an isolated diamond nanoparticle on SiN (blue) and a diamond nanoparticle on top of a Ag pillar (red). (b) Enhancement factors for the diamond CL as calculated as the ratio of total signal from plasmonically enhanced diamond to isolated diamond.

the recombination rate and phonon-induced dephasing. Because of the significant phonon population illustrated in figure 4.3, the coherence time is not likely representative the lifetime of the system. Therefore, we did not observe the decreased luminescence lifetime that would unambiguously confirm that this enhancement was the result of a Purcell effect.

4.4.1 Second-order correlation

Previous work done on NV centers in a STEM were done at cryogenic temperatures in order to gather enough signal to show anti-bunching behavior from a single defect site. [56] Here we will look at the statistics of the plasmonically enhanced signal at room temperature. Second-order correlations from plasmonically enhanced NV centers were viewed in two different spectral regimes. First, we will measure the statistics of the entire emission without optical filtering. This will include both the ZPL and the phonon-assisted emission.

A completely unfiltered $g^{(2)}$ curve for the plasmonically enhanced NV center is shown in figure 4.7. The diamond nanocrystals used in this experiment were of comparable defect density to those used in[57], with greater than 1200 NV centers per particle, but the 1 nA
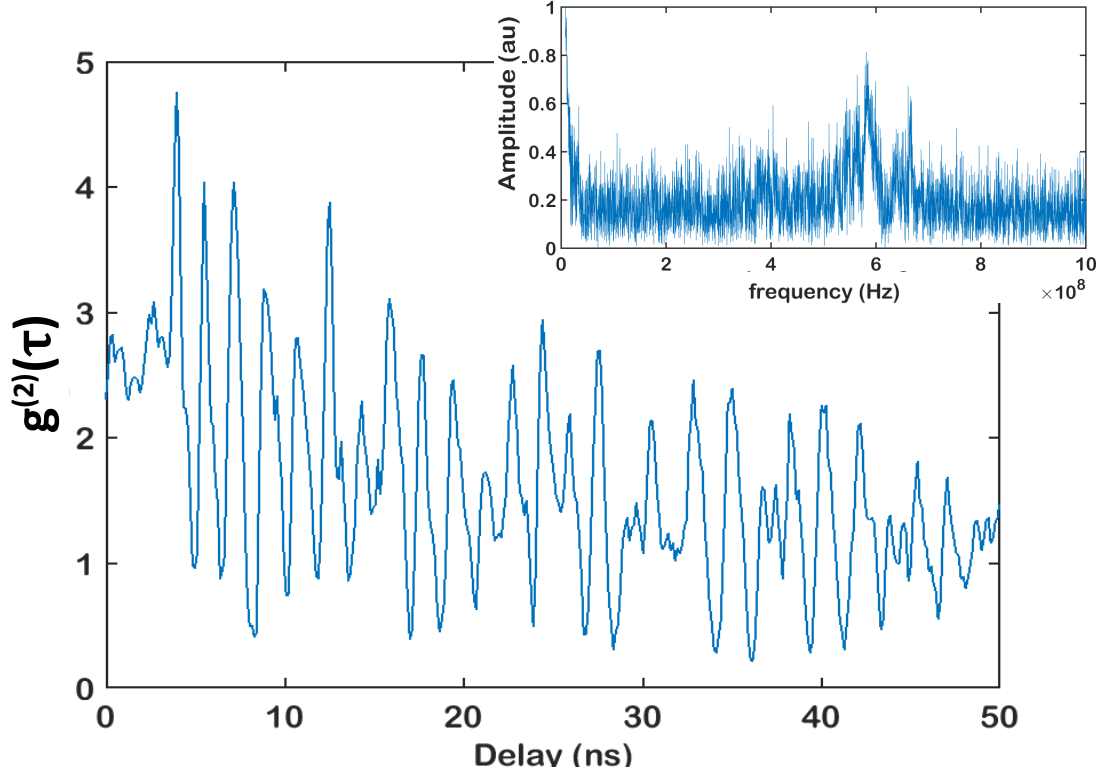
Figure 4.7: Second order correlation curves for optically unfiltered cathodoluminescence. Rabi flopping oscillations of approximately 1.7 ns in period are present. This measurement was taken with an electron-beam current of 1 nA.

current used was orders of magnitude greater. The maxima of these oscillations violate the Cauchy-Schwarz condition for classical light sources defined in equation 1.28, but not the one listed in equation 1.31, suggesting that the large phonon population results in a slight decoherence of the electron-beam driven system.

The Rabi oscillations in the effective two-level nitrogen vacancy center defect coupling to the electron beam are qualitatively consistent with the model in section 4.3. The current used in this measurement is approximately 1 nA which corresponds to an average of one electron arrival every 160 ps. This excitation rate is below the room temperature lifetime of neutral NV defects of ~ 20 ns [94] analogous to a continuous wave photonic excitation source. The Rabi flopping period is about 1.7 ns, and has a decoherence time on the order of tens of nanoseconds which is consistent with previous optically driven second-order correlation measurements.
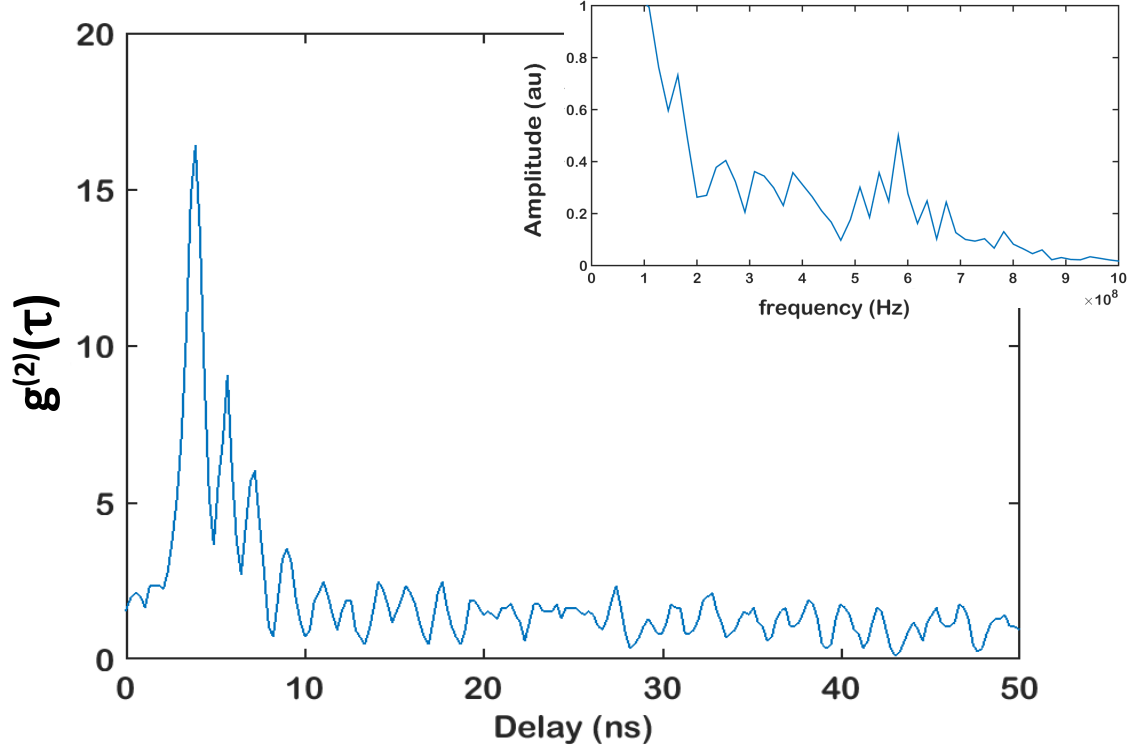
Figure 4.8: Second-order correlation curves for cathodoluminescence spectrally filtered a bandpass filter centered at the ZPL, 575 nm. The same 1.7 ns Rabi flopping period is present.

4.4.2 Zero-phonon line statistics

This experiment was performed on the same plasmonic system after adding a bandpass filter centered at the ZPL of 575 nm in front of the beamsplitter in the Hanbury Brown-Twiss interferometer. Since the ZPL and the phonon-assisted emission are spectrally overlapping, this did not completely filter out the phonon assisted emission, but it does allow the statistics of the ZPL to be the dominant signal in the $g^{(2)}$ curve. The overall Rabi flopping signature retains the same period as with the unfiltered signal, but the amplitude of the oscillations is significantly larger. By filtering out the phonon-broadened signal, we have effectively removed a major source of decoherence. This can be seen in the violation of both of the classical conditions written in equation 1.28 and equation 1.31.
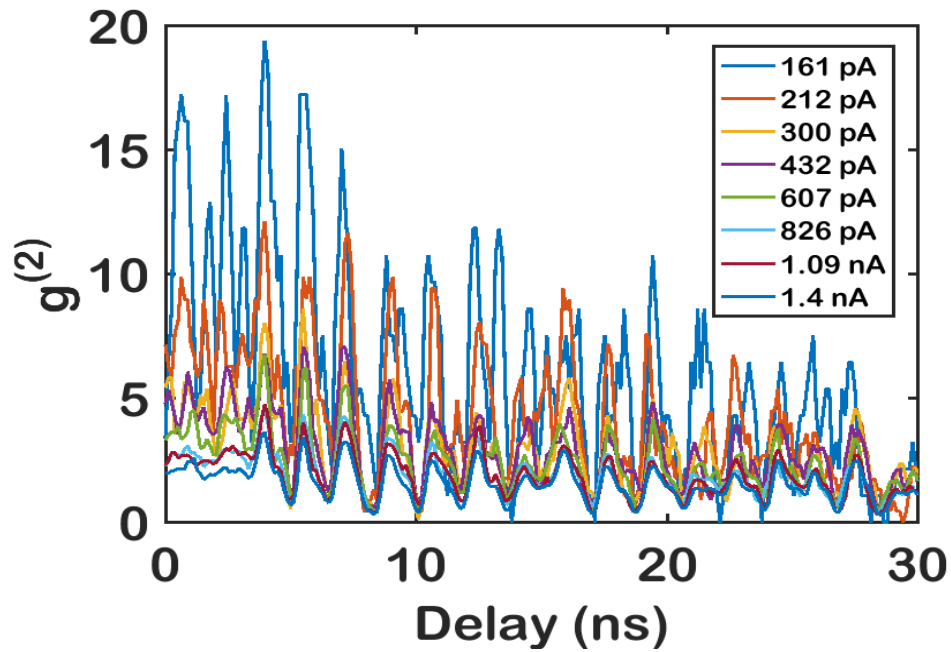
Figure 4.9: Electron beam current dependence of photon-bunching for unfiltered CL.
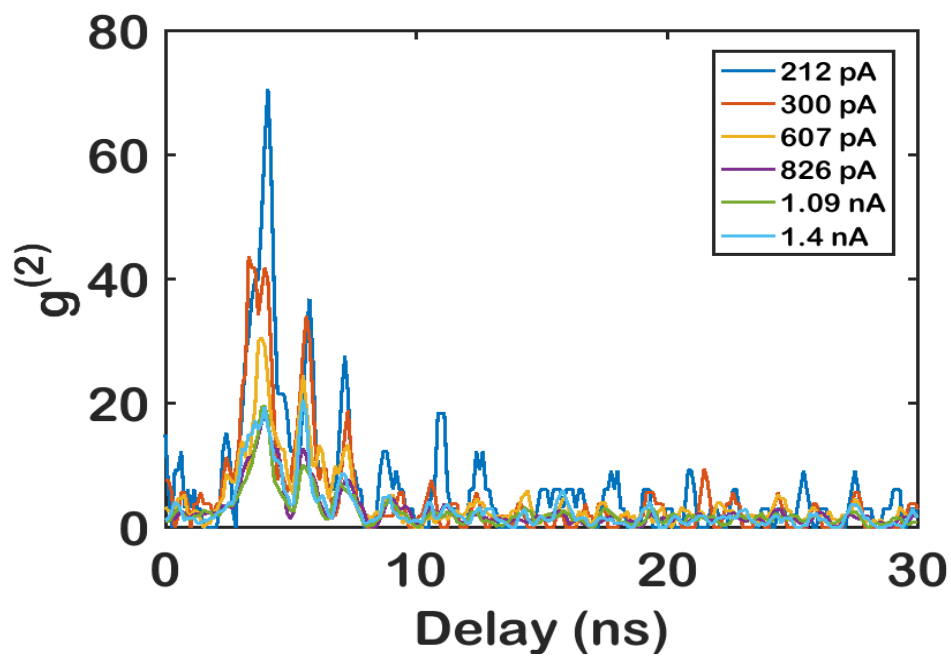
Figure 4.10: Electron beam current dependence of photon-bunching for bandpass filtered CL at 575 nm.

4.4.3   Rabi oscillation amplitude current dependence

As seen in both figures 4.10 and 4.11, the magnitude of the Rabi oscillation amplitude decreased as the electron beam current was increased. This is qualitatively similar to the reduced bunching with increasing current as seen in NV centers weakly driven by electron beams.[57] As the current is increased, more diamond plasmons are excited within the lifetime of a single defect site. Because each plasmon excites fourteen or fewer NV centers, the system is operating well below saturation and additional NV centers are excited with each excited plasmon. Increasing the electron-beam current in this scenario is analogous to increasing the number of emitters in the photonic picture illustrated in figure 4.5. The Poissonian distribution of electrons within the electron beam drives $g^{(2)}$ towards one with increasing current similarly to the stochastic nature of light-matter interactions driving $g^{(2)}$ towards one with increasing N. A complete numerical model of this system is still in development.

This is the first demonstration of quantum coherent dynamics in an electron microscope. The nth order nonlinearity in the Hamiltonian describing the electron-beam dressed state suggests that in a sufficiently coherent system the technique described here could enable the generation of scalable entanglement. With increasing interest in coupling quantum states of light into plasmonic structures [95, 96], particularly for ultratrace plasmonic sensing [97, 98], the ability to generate scalable entangled states of light on-chip will enable parallelizable quantum sensors capable of resolving signatures previously buried in quantum noise.

Chapter 5

Conclusion

The overarching goal of this dissertation was to explore the limits of efficiency and control of nonlinear plasmonic systems. We have demonstrated several methods of using the plasmonic near-field to enhance optical nonlinearities at the nanoscale. This work demonstrates a powerful means of engineering $\chi^{(2)}$ of plasmonic metasurfaces as well as generating coupling strengths strong enough to induce novel quantum optical phenomenon. A key theme throughout this dissertation has been to design optical experiments in order to gain superior temporal resolution than in previous work. This has allowed us to directly observe energy dynamics that have to date been, to the best of our knowledge, unobserved.

5.1 Major achievements

These experiments have answered a few questions on the subject of nonlinear plasmonics, but, more importantly, they have opened up an entirely new class of experiments that will further our fundamental understanding of nonlinear plasmonics. First we will outline the major achievements of this work.

5.1.1 Archimedean nanospirals

We have demonstrated a novel plasmonic geometry with no planar symmetry with a stronger $\chi^{(2)}$ than any previously reported fully metallic plasmonic antenna. The effective second-order susceptibilty was $d_{eff} = 15.3 \ pm/V$, approximately four times larger than that of bulk beta-barium borate. We have characterized the chiral characteristics of a two-dimensional plasmonic antenna via polarization conversion of light as it is converted into second-harmonic light. This polarization conversion was not only more efficient than

previous plasmonic elements, but was able to convert between polarizations across the linear, circular, and depolarized states. STEM-CL measurements experimentally verified the near-field profile of the nanospiral plasmon that had previously only been simulated. This also demonstrated a powerful non-perturbative means of measuring the near-field profiles of complex plasmonic systems.

5.1.2   The serrated nanogaps

We have designed a novel spectroscopy technique involving the interference of an optical pulse and a plasmonic resonance to probe the changes in the nonlinear susceptibility of a dielectric material under plasmonic exposure. Using the new type of spectroscopy, real-time oscillations in the second-order nonlinear susceptibility with a temporal resolution of 100as were observed. This resolution is not the limit of the experimental technique demonstrated here, but there was no information to gain from this system past this resolution. We have designed a plasmonic geometry that can serve as a platform for studying the nonlinear properties of any thin film material that can be deposited within the serrated nanogap.

5.1.3   Electron beam induced Rabi flopping in nitrogen vacancy centers

We have demonstrated Rabi flopping in NV centers coupled to an electron beam at room temperature with coherence times on the order of tens of nanoseconds. We have observed the differences between the maximum second-order correlation values of zero-phonon and phonon-assisted cathodoluminescence.

Each of these contributions has made progress towards a singular goal. We have designed and implemented three unique metasurfaces that have pushed the limits of nonlinear optical interactions in nanostructured systems.

5.2   Future work

While these achievements are exciting for the advancement of plasmonics technology, perhaps what is more exciting is the experiments that are left to be done on each of these systems.

5.2.1   The Archimedean nanospiral

The SHG experiments using the nanospiral were done by varying the geometry over a small parameter space. Due to time limitations, we did not fabricate enough nanospiral arrays to completely optimize nanospiral geometry. While the 4π spiral with the specific dimensions described in chapter 2 was a particularly good harmonic generator, the harmonic conversion efficiency could potentially be enhanced by optimizing the winding number, arm width, and arm spacing. Also, there are many more types of spirals than the Archimedean one.

5.2.2   Spatial light modulation

The spatial light modulation techniques used in chapters 2 and 3 only scratched the surface of the potential this process has in the study of plasmonics. The temporal control that the SLM allows over the structure of optical pulses could be a boon to both the study of plasmonic nonlinearities and material properties. We have preliminary data that shows an enhancement of the nanospiral harmonic conversion efficiency of about 10% when deviating from a transform limited pulse using a third order polynomial modulation to the optical pulse in frequency space. This shows that the optimal light pulse for harmonic generation is not one that solely generates maximum instantaneous intensities. This process of optical pulse engineering is not specific to the nanospiral, but the complex spatial profile of the nanospiral near-field might be particularly well suited to this type of enhancement.

5.2.3 Second-harmonic interferometry

The interferometry techniques demonstrated here only used PMMA as a dielectric material. This was because PMMA has no natural second-order nonlinear response. This made it easy to detect a change in $\chi^{(2)}$ of this material. The technique we have designed could be used to investigate any material that could be deposited in a thin film within the gap. With processes such as atomic layer deposition and chemical vapor deposition, this could easily be done with dielectric materials that have inherent nonlinearities without being exposed to plasmonic fields. It is already known that plasmons can drive the nonlinear properties of materials that already have impressive conversion efficiencies. [41, 42] This technique could reveal the temporal dynamics of these materials and how they respond to plasmonic fields. The serrated nanogap itself could potentially be coupled to a strongly nonlinear material such as GaAs in order to generate an efficient nonlinear plasmonic device.

5.2.4 Cathodoluminescence photon statistics

We have presented exciting results for exploring plasmonic coupling to longer lived excitations like excitons. The electron beam provided a passive driving field with nanoscale spatial resolution, but no active control over the quantum dynamics of the coupled system. Integrating a dynamically tunable optical control field with the existing electron microscope will enable us to engineer more complex quantum states by introducing active control to the Hamiltonian of the coupled system. Quantum emitters that are less well known for single photon behavior than the NV center in diamond will be investigated. The relatively long lived plasmonic Fano resonance could potentially couple more strongly to these quantum systems due to an increased quality factor. The Ag pillars that were used in this dissertation were not tuned with respect to the NV defect emission wavelengths, nor was the mode volume of the plasmon minimized.

Appendix A

Finite-difference time-domain simulations

FDTD simulations are centered around two approximations of the exact solutions of Maxwell's equations. The first approximation is that the electric and magnetic fields propagate through a cubic lattice known as the Yee cell. This effective quantitization of space, as seen in Figure 1.7, is composed of two interlocking lattices of the electric and magnetic portions of the local field. In order for this approximation to yield accurate results, we must choose a lattice constant for the Yee cell such that the electric and magnetic fields do not change appreciably over a single lattice increment. This means that the resolution of our numerical analysis must be smaller than a fraction of the wavelength, $\sim \Delta \hat{x} < \lambda/10$. The second approximation is referred to as the "leapfrog arrangement". This means that while both the calculations for $\tilde{\mathbf{E}}$ and $\tilde{\mathbf{H}}$ are coupled to one another via Maxwell's equations, they
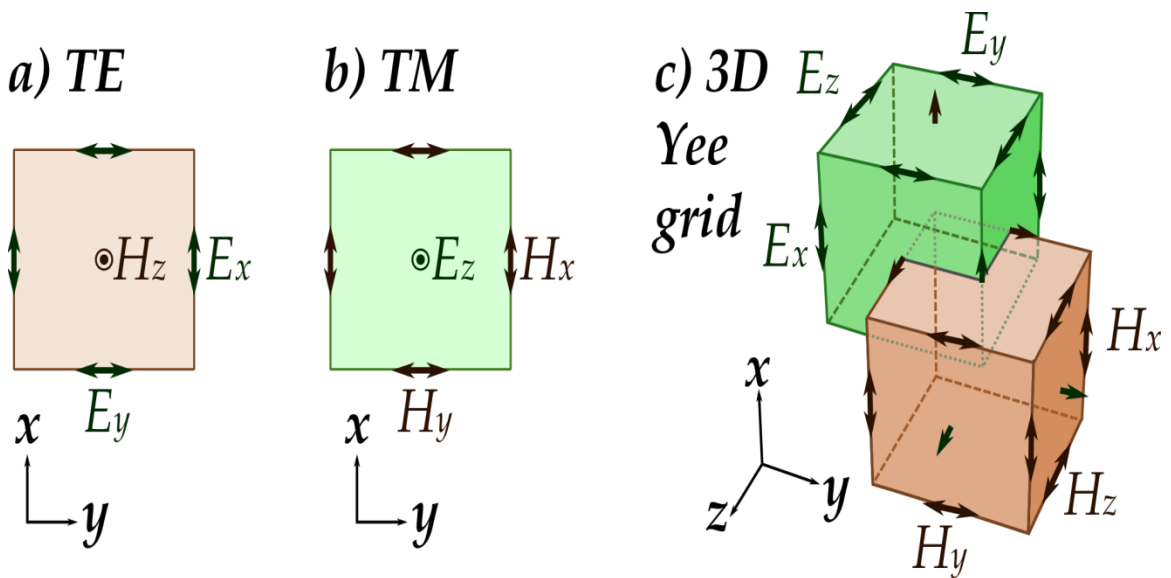
Figure A.1: (a) Two-dimensional section of the Yee cell electric field lattice(b) Two-dimensional section of the Yee cell magnetic field lattice.(c) Three-dimensional representation of the Yee cell with interlocking electric and magnetic field lattices. [99]

are not calculated simultaneously. Instead, they are solved sequentially in time. $\tilde{\mathbf{E}}$ will be solved for a particular time step using previously stored data for $\tilde{\mathbf{H}}$, and then the next time step will be solved for $\tilde{\mathbf{H}}$ using the previous data for $\tilde{\mathbf{E}}$. The advantage of this leapfrog time-stepping is that it can calculate the coupling effects between $\tilde{\mathbf{E}}$ and $\tilde{\mathbf{H}}$ while avoiding the time consuming simultaneous solution. [100, 101, 102]

This simulation method can accurately reproduce the far-field emission characteristics of the plasmon resonance, e.g. scattering and transmission, but it is obviously not limited to the far-field. Since $\tilde{\mathbf{E}}$ and $\tilde{\mathbf{H}}$ were directly calculated as a function of time and space, we can infer the spatial electric field profile of the plasmonic resonance. This is especially useful for plasmonic characterization as near-field measurements must involve interaction with the plasmonic system at a sub-diffraction size scale. There are a few reliable experimental procedures for doing this, but they are cumbersome and time-consuming in comparison to a few hours use of a computer simulation. Figure 1.8 shows the results of an FDTD simulation on the near-field of a plasmonic gold nanorod. From here we can easily infer the spectral and spatial positions of the plasmon resonance. In short, FDTD simulations allow
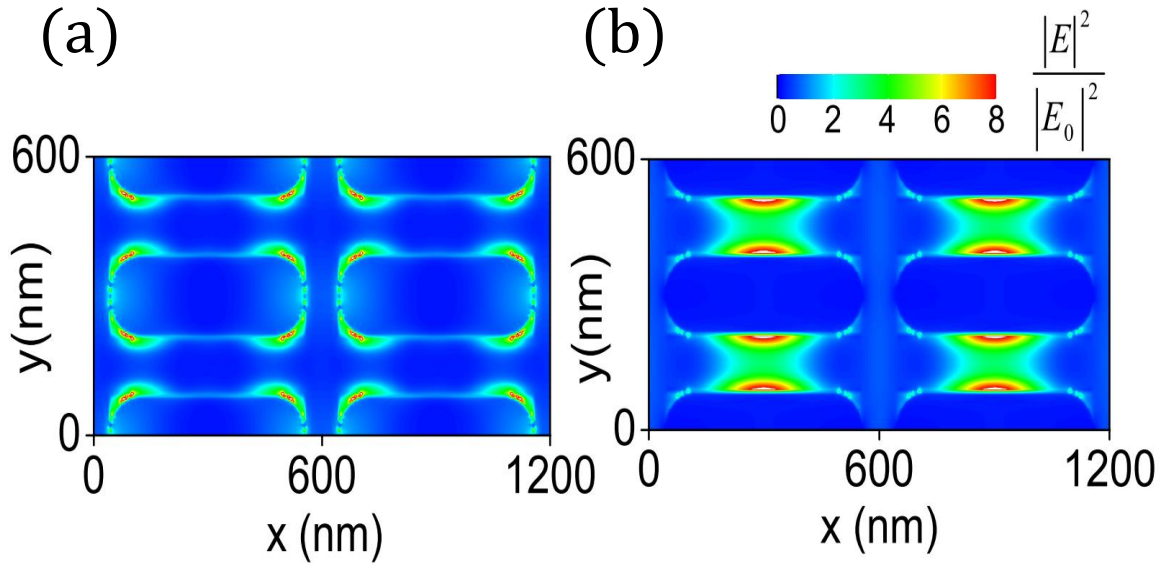
Figure A.2: Finite-difference time-domain (FDTD) simulations of gold nanorods excited with light polarized in the (a) x-direction at $\lambda = 695nm$ and (b) y-direction at $\lambda = 905nm$. The color scale represents the electric field enhancement factor.[103]

us to accurately fabricate plasmonic structures with dimensions that produce the desired dielectric functions, as well as probe the near-field of these structures. We can predict how plasmons will change upon a alteration of their dielectric environment and how they will couple to nearby charge distributions. Near-field information of these plasmonic structures has led to several important plasmonic applications such as electromagnetically-induced transparency and single-molecule detection. [104, 105, 106, 107]

Appendix B

Calculations for SHG efficiency and $d_{eff}^{(2)}$

When calculating the SHG efficiency for plasmonic metasurfaces, one must be careful to consider all of the experimental parameters that are not essential to the nonlinearity of the plasmonic antenna but still contribute to the overall nonlinear signal. These effects constitute a set of correction factors that are necessary to correctly calculate a metasurface nonlinear conversion efficiency. The correction factors that are used in this calculation are:

- filling factor
- background signal
- fundamental leakage

- detector efficiency
- transmission of optical filters
- SHG from other sources

B.1   SHG efficiency

The equation for harmonic conversion efficiency is quite simple. It's just the ratio of the total intensity of the nonlinear emission and the fundamental excitation.

$$\eta_{SHG} = \frac{I(2\omega)}{I(\omega)} \tag{B.1}$$

Where, ideally, the term 2ω is purely a result of the second-harmonic produced by the plasmonic antenna. This is, of course, not the case. All of the things listed above can contribute or diminish the total signal and must be corrected for individually. The background contribution, fundmental leakage, and SHG from other sources can all be dealt with by performing an SHG measurement on the bare substrate that is being used to support the plasmonic particles. This signal can then be subtracted from the SHG signal from the plasmonic source. There will be an error created by plasmonic enhancement of SHG from the substrate.

The other factors are simply a matter of careful measurement and calibration. The detectors and filters were calibrated using a well known light source. The filling factor of the nanoparticles was calculated using a scanning electron microscopy image of the particle array. The final equation used was:

$$\eta_{SHG} = \frac{I_{measured}(2\omega) - I_{substrate}(2\omega)}{I(\omega) \cdot f} \tag{B.2}$$

Where f is the filling factor of the plasmonic array. $I(\omega)$ was calculated based on the laser power as measured by a silicon photodetector.

B.2 Effective second-order susceptibility for the Archimedean nanospiral

The effective second-order susceptibility is written in [3] as

$$P(2\omega) = 2\varepsilon d_{eff} E(\omega)^2 \tag{B.3}$$

which leads to

$$d_{eff} = \frac{cnP(2\omega)}{I(\omega)} \tag{B.4}$$

So the question now becomes how to calculate the dielectric polarization $P(2\omega)$. We can do so by treating electrons in the nanospirals as Hertzian dipoles, for which, in the classical model of the one-dimensional oscillator, we have a time-varying polarization $P(2\omega) = Nex(t)$, with $x(t)$ being determined by the oscillation frequency at 2ω. The oscillation frequency at 400 nm is $\nu = c\lambda = 0.75 \cdot 10^{15}$ Hz. Assume that the electrons can move at the Fermi velocity, which for gold is $v_F = 1.4 \cdot 10^6 ms^{-1}$. The dipole moment x_0 involves the distance over which the electron can oscillate in one cycle of the electromagnetic field is $x_0 = v_F/\nu = 1.4 \cdot 10^6 ms^{-1}/0.75 \cdot 10^{15} Hz = 1.87nm$. From this we can then calculate (again, still in the classical model) $P(2\omega) = Nex_0$ given that the free-electron density in the gold is $N = 5.9 \cdot 10^{28} m^3$,

$$P(2\omega) = Nex_0 = (5.9 \cdot 10^{28} m^{-3})(1.6 \cdot 10^{-19} C)(1.87 \cdot 10^{-9} m) = 17.6 Cm^{-2} \qquad \text{(B.5)}$$

The energy in a single pulse is 0.33 pJ, with a pulse duration of 15 fs; the focal spot diameter is nearly diffraction-limited and we assume 10 m. The intensity for a single pulse is therefore

$$I = \frac{4P(\omega)}{\pi w_0^2} = 1.12 \cdot 10^{12} Wm^{-2} \qquad \text{(B.6)}$$

We must then correct for the quantum efficiency (measured to range from $3.6 \cdot 10^{-9}$ to $1.4 \cdot 10^{-8}$), because not every electron is excited at 400 nm; we do not need to correct for the filling fraction within the focal volume (0.12) because that is taken into account by the way we measured overall efficiency. Then for the effective second-order susceptibility, we have

$$d_{eff} = \eta_{SHG} \frac{cnP(2\omega)}{I(\omega)} \qquad \text{(B.7)}$$

Using this formalism for linear polarization and left and right handed circular polarization, we calculated the effective second-order susceptibilities reported in chapter 2.

Appendix C

Optical damage in plasmonic antennas

Unlike their macroscale counterparts, optical antennas have a great deal of non-radiative loss. This causes substantial heating of these antennas. If pumped with intense enough light, irreversible damage will take place. Figure C.1 shows an SEM image of a nanospiral that was excited with an optical power exceeding 30 mW. The nanospirals nonlinear and chiral properties were lost after being overexposed.

In order to avoid this, a linear polarizer and half-wave plate combination were used to tune the power of the incident laser. It is important to note that there are publsihed methods for protecting metallic antennas from melting by encasing them in a thin film of silica or similar transparent materials. This method was not used here, but it could be easily employed to push the overall efficiency of the nanospiral harmonic conversion efficiency
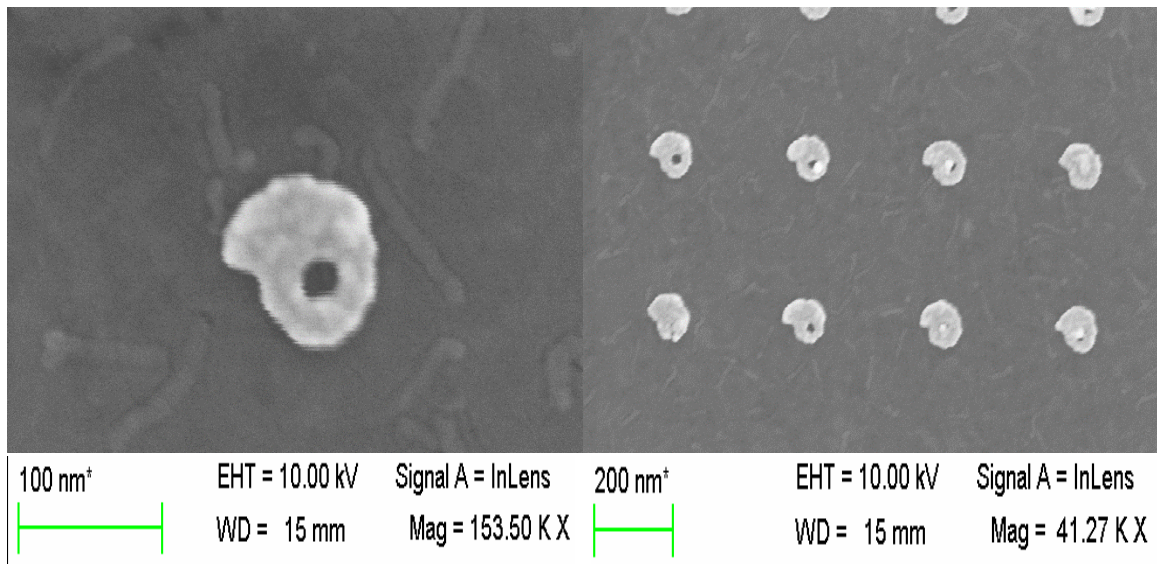
Figure C.1: Gold nanospiral arrays after being exposed to laser powers exceeding the melting threshold of the antenna.

even higher.

Appendix D

Fabrication details for EBL, FIB, and SiN membranes

D.0.1   Nanostructure fabrication

There are several different methods for fabricating plasmonic nanostructures with vary-
ing degrees of precision on mass-production capacity. There only two that are relevant to
the experiments presented here are electron beam lithography (EBL) and focused ion beam
milling (FIB). Here we will outline the basic procedures that were used to create nanostruc-
tures used throughout this research. The two techniques are similar in that they both use a
charged particle beam in order to mill out a specific geometry. They are unlike chemical
synthesis methods in that each individual nanoparticle is formed in a deterministic man-
ner, however they are limited in their ability to manufacture large numbers of structures
efficiently.

EBL is a process where a resist material is damaged in order create a mask in the shape
of the desired nanostructure geometry. Figure 1.9 shows this process using negative resist
and a glass substrate with a 2 nm indium tin oxide (ITO) layer. ITO covered glass is the
substrate that is used for the majority of the EBL reported here, but the only requirement on
the substrate is that it be conductive. This prevents a build up of charge from the electron
beam current. A resist material is then deposited onto the substrate and then exposed with
the electron beam in the pattern of the desired nanostructure. The exposure causes the
molecular structure of the resist to break down so that it may be more easily removed via
a solvent. After the damaged resist is removed, the metal of choice is deposited across
the entire surface. After the entirety of the resist is removed, all that is left is the metallic
nanostructure. Plasmonic structures made with this process can have feature sizes on the
order of 20 nm. Some simple structures can even push this limit down to a few nanometers.
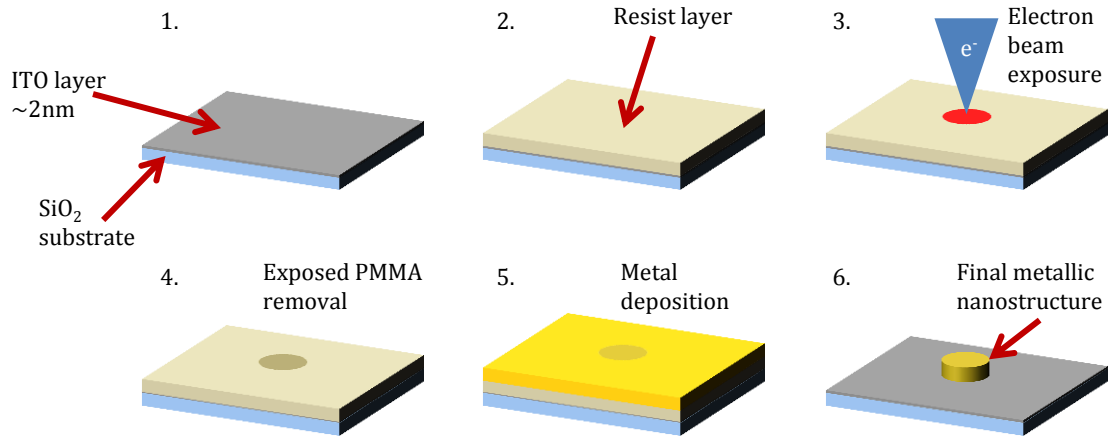
Figure D.1: Electron-beam lithography (EBL) process.

This lower limit on resolution is largely due to the effective interaction volume of the electron. [108, 109, 110]

The other method used in this research for the fabrication of plasmonic structures is focused ion beam milling. This is where the sample begins as a solid piece of material such as a metallic or dielectric film and is milled out using an ion source. Some of the primary elements used for FIB are gallium, argon, and helium. Gallium and argon based FIB processes can reach spatial resolutions on par with EBL, however helium ion sources can surpass EBL by approximately a factor of two. Figure 1.10 demonstrates the FIB process using a thin metallic layer being milled by a gallium ion source. Fabricating plasmonic structures using FIB is clearly superior to EBL when generating structures where the plasmon is defined by the boundary conditions of the vacuum, such as a hole or a grating. However, when generating geometries that involve individual particles like in Figure 1.9, this can be time consuming. [111, 112]

Since neither the fabrication nor simulation process is limited to analytical geometries such as the disc or rod, it is a natural next step to observe the near-field profiles and the dielectric functions of more complex nanostructures. Here we can begin to observe the
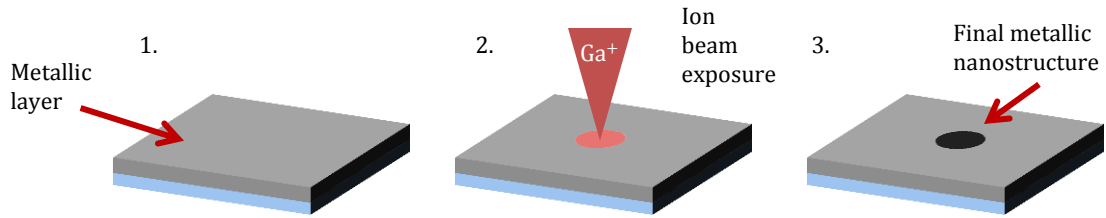
Figure D.2: Focused-ion beam milling (FIB) process.

effects of curved electron paths and coupling to other systems. These complications will actually be critical to the nonlinear optical effects that we will report in the experimental sections.

D.0.2   Silicon nitride membranes

The silicon nitride membranes that were used in the cathodoluminescence experiments in chapters 1 and 4 were made by a series of etching processes on a $300\mu m$ thick silicon wafer with 50 nm of silicon nitride on both sides. These wafers were fabricated by the staff at CNMS. Any electron beam lithography on the surface of the silicon nitride was done beforehand. After EBL, windows were etched into the backside silicon nitride with reactive ion etching and into the silicon with KOH etching. Afterwards, all that remained was the front facing silicon nitride window.

Fabrication details such as dosing, CAD files, and etch times can be found in the fabrication CAD computer at CNMS as well as the clean room notebooks there.

BIBLIOGRAPHY

[1] Jing-yuan Zhang, Jung Y Huang, H Wang, KS Wong, and GK Wong. Second-harmonic generation from regeneratively amplified femtosecond laser pulses in bbo and lbo crystals. *JOSA B*, 15(1):200–209, 1998.

[2] A Dubietis, G Jonušauskas, and A Piskarskas. Powerful femtosecond pulse generation by chirped and stretched pulse parametric amplification in bbo crystal. *Optics Communications*, 88(4-6):437–440, 1992.

[3] Robert W. Boyd. *Nonlinear Optics (3rd Edition)*. Elsevier, 2008.

[4] John E. Zernike, Frits; Midwinter. *Applied Nonlinear Optics (2nd Edition)*. Courier Corporation, 2006.

[5] Stefan Alexander Maier. *Plasmonics: fundamentals and applications*. Springer Science & Business Media, 2007.

[6] Yu Zhang, Nathaniel K Grady, Ciceron Ayala-Orozco, and Naomi J Halas. Three-dimensional nanostructures as highly efficient generators of second harmonic light. *Nano Letters*, 11(12):5519–5523, 2011.

[7] Heykel Aouani, Miguel Navarro-Cia, Mohsen Rahmani, Themistoklis PH Sidiropoulos, Minghui Hong, Rupert F Oulton, and Stefan A Maier. Multiresonant broadband optical antennas as efficient tunable nanosources of second harmonic light. *Nano Letters*, 12(9):4997–5002, 2012.

[8] Martti Kauranen and Anatoly V Zayats. Nonlinear plasmonics. *Nature Photonics*, 6(11):737–748, 2012.

[9] Michele Celebrano, Xiaofei Wu, Milena Baselli, Swen Großmann, Paolo Biagioni, Andrea Locatelli, Costantino De Angelis, Giulio Cerullo, Roberto Osellame, Bert Hecht, et al. Mode matching in multiresonant plasmonic nanoantennas for enhanced second harmonic generation. *Nature Nanotechnology*, 10(5):412–417, 2015.

[10] Krishnan Thyagarajan, Simon Rivier, Andrea Lovera, and Olivier JF Martin. Enhanced second-harmonic generation from double resonant plasmonic antennae. *Optics Express*, 20(12):12860–12865, 2012.

[11] Antonio Capretti, Gary F Walsh, Salvatore Minissale, Jacob Trevino, Carlo Forestiere, Giovanni Miano, and Luca Dal Negro. Multipolar second harmonic generation from planar arrays of au nanoparticles. *Optics Express*, 20(14):15797–15806, 2012.

[12] Hannu Husu, Roope Siikanen, Jouni Makitalo, Joonas Lehtolahti, Janne Laukkanen, Markku Kuittinen, and Martti Kauranen. Metamaterials with tailored nonlinear optical response. *Nano Letters*, 12(2):673–677, 2012.

[13] Thibault Peyronel, Ofer Firstenberg, Qi-Yu Liang, Sebastian Hofferberth, Alexey V Gorshkov, Thomas Pohl, Mikhail D Lukin, and Vladan Vuletić. Quantum nonlinear optics with single photons enabled by strongly interacting atoms. *Nature*, 488(7409):57–60, 2012.

[14] Eiichi Hanamura, Yutaka Kawabe, and Akio Yamanaka. *Quantum nonlinear optics*. Springer Science & Business Media, 2007.

[15] II Davidson, B Roderick, Jed I Ziegler, Guillermo Vargas, Sergey M Avanesyan, Yu Gong, Wayne Hess, and Richard F Haglund Jr. Efficient forward second-harmonic generation from planar archimedean nanospirals. *Nanophotonics*, 4(1), 2015.

[16] Roderick B Davidson, Anna Yanchenko, Jed I Ziegler, Sergey M Avanesyan, Benjamin J Lawrie, and Richard F Haglund. Ultrafast plasmonic control of second harmonic generation. *ACS Photonics*, 2015.

[17] Mark Fox. *Optical Properties of Solids (2nd Edition)*. Oxford University Press, 2010.

[18] Marc D. Levenson. *Introduction to Nonlinear Laser Spectroscopy*. Academic Press, 1982.

[19] Maria Göppert-Mayer. Über elementarakte mit zwei quantensprüngen. *Annalen der Physik*, 401(3):273–294, 1931.

[20] T. H. Maiman. Optical and microwave-optical experiments in ruby. *Physical Review Letters*, 4:564–566, Jun 1960.

[21] P. A. Franken, A. E. Hill, C. W. Peters, and G. Weinreich. Generation of optical harmonics. *Physical Review Letters*, 7:118–119, Aug 1961.

[22] J. Volicer and Stephen F. Tello. The structure of simple solids, 1998.

[23] Kohei Imura, , Tetsuhiko Nagahara, , and Hiromi Okamoto*, . Near-field two-photon-induced photoluminescence from single gold nanorods and imaging of plasmon modes. *The Journal of Physical Chemistry B*, 109(27):13214–13220, 2005. PMID: 16852648.

[24] J. Z. Sanborn, C. Hellings, and T. D. Donnelly. Breakdown of the slowly-varying-amplitude approximation: generation of backward-traveling, second-harmonic light. *JOSA B*, 20(1):152–157, Jan 2003.

[25] D. N. Nikogosyan. Beta barium borate (bbo). *Applied Physics A*, 52(6):359–368, 1991.

[26] Intel microprocessor quick reference guide - year, 2008.

[27] Constantine A Balanis. *Antenna theory: analysis and design*. John Wiley & Sons, 2016.

[28] Lukas Novotny and Niek Van Hulst. Antennas for light. *Nature Photonics*, 5(2):83–90, 2011.

[29] Palash Bharadwaj, Bradley Deutsch, and Lukas Novotny. Optical antennas. *Advances in Optics and Photonics*, 1(3):438–483, 2009.

[30] Motoichi Ohtsu. Handbook of nano-optics and nanophotonics. *Handbook of Nano-Optics and Nanophotonics:, ISBN 978-3-642-31065-2. Springer-Verlag Berlin Heidelberg, 2013*, 1, 2013.

[31] Oliver Benson. Assembly of hybrid photonic architectures from nanophotonic constituents. *Nature*, 480(7376):193–199, 2011.

[32] Justin White. Surface plasmon polaritons, 2007.

[33] C Ciracì, RT Hill, JJ Mock, Y Urzhumov, AI Fernández-Domínguez, SA Maier, JB Pendry, A Chilkoti, and DR Smith. Probing the ultimate limits of plasmonic enhancement. *Science*, 337(6098):1072–1074, 2012.

[34] VAG Rivera, E Marega Jr, and FA Ferri. *Localized surface plasmon resonances: noble metal nanoparticle interaction with rare-earth ions*. INTECH Open Access Publisher, 2012.

[35] E Prodan, C Radloff, Naomi J Halas, and P Nordlander. A hybridization model for the plasmon response of complex nanostructures. *Science*, 302(5644):419–422, 2003.

[36] Chia-Yang Tsai, Shao-Ping Lu, Jyun-Wei Lin, and Po-Tsung Lee. High sensitivity plasmonic index sensor using slablike gold nanoring arrays. *Applied Physics Letters*, 98(15):153108, 2011.

[37] OL Muskens, V Giannini, JA Sßnchez-Gil, and J Gmez Rivas. Optical scattering resonances of single and coupled dimer plasmonic nanoantennas. *Optics Express*, 15(26):17736–17746, 2007.

[38] Encai Hao and George C Schatz. Electromagnetic fields around silver nanoparticles and dimers. *The Journal of Chemical Physics*, 120(1):357–366, 2004.

[39] Bernd Metzger, Mario Hentschel, and Harald Giessen. Ultrafast nonlinear plasmonic spectroscopy: From dipole nanoantennas to complex hybrid plasmonic structures. *ACS Photonics*, 2016.

[40] Gustavo Grinblat, Mohsen Rahmani, Emiliano Cortés, Martín Caldarola, David Comedi, Stefan A Maier, and Andrea V Bragas. High-efficiency second harmonic generation from a single hybrid zno nanowire/au plasmonic nano-oligomer. *Nano Letters*, 14(11):6660–6665, 2014.

[41] Jongwon Lee, Mykhailo Tymchenko, Christos Argyropoulos, Pai-Yen Chen, Feng Lu, Frederic Demmerle, Gerhard Boehm, Markus-Christian Amann, Andrea Alù, and Mikhail A Belkin. Giant nonlinear response from plasmonic metasurfaces coupled to intersubband transitions. *Nature*, 511(7507):65–69, 2014.

[42] Heykel Aouani, Mohsen Rahmani, Miguel Navarro-Cía, and Stefan A Maier. Third-harmonic-upconversion enhancement from a single semiconductor nanoparticle coupled to a plasmonic antenna. *Nature Nanotechnology*, 9(4):290–294, 2014.

[43] Darrick E Chang, Vladan Vuletić, and Mikhail D Lukin. Quantum nonlinear optics - photon by photon. *Nature Photonics*, 8(9):685–694, 2014.

[44] Roy J Glauber. The quantum theory of optical coherence. *Physical Review*, 130(6):2529, 1963.

[45] Roy J Glauber. Coherent and incoherent states of the radiation field. *Physical Review*, 131(6):2766, 1963.

[46] PR Rice and HJ Carmichael. Single-atom cavity-enhanced absorption. i. photon statistics in the bad-cavity limit. *IEEE Journal of Quantum Electronics*, 24(7):1351–1366, 1988.

[47] HJ Carmichael and DF Walls. A quantum-mechanical master equation treatment of the dynamical stark effect. *Journal of Physics B: Atomic and Molecular Physics*, 9(8):1199, 1976.

[48] SL Mielke, GT Foster, and LA Orozco. Nonclassical intensity correlations in cavity qed. *Physical Review Letters*, 80(18):3948, 1998.

[49] BR Mollow. Power spectrum of light scattered by two-level systems. *Physical Review*, 188(5), 1969.

[50] Xiaodong Xu, Bo Sun, Paul R Berman, Duncan G Steel, Allan S Bracker, Dan Gammon, and Lu J Sham. Coherent optical spectroscopy of a strongly driven quantum dot. *Science*, 317(5840):929–932, 2007.

[51] M Baur, S Filipp, R Bianchetti, JM Fink, M Göppl, L Steffen, PJ Leek, Alexandre Blais, and A Wallraff. Measurement of autler-townes and mollow transitions in a strongly driven superconducting qubit. *Physical Review Letters*, 102(24):243602, 2009.

[52] Paz London, J Scheuer, J-M Cai, I Schwarz, A Retzker, MB Plenio, M Katagiri, T Teraji, S Koizumi, J Isoya, et al. Detecting and polarizing nuclear spins with double resonance on a single electron spin. *Physical Review Letters*, 111(6):067601, 2013.

[53] Arne Laucht, Rachpon Kalra, Stephanie Simmons, Juan P Dehollain, Juha T Muhonen, Fahd A Mohiyaddin, Solomon Freer, Fay E Hudson, Kohei M Itoh, David N Jamieson, et al. A dressed spin qubit in silicon. *Nature Nanotechnology*, 2016.

[54] Alexander Huck, Shailesh Kumar, Abdul Shakoor, and Ulrik L Andersen. Controlled coupling of a single nitrogen-vacancy center to a silver nanowire. *Physical Review Letters*, 106(9):096801, 2011.

[55] A Gruber, A Dräbenstedt, C Tietz, L Fleury, J Wrachtrup, and C Von Borczyskowski. Scanning confocal optical microscopy and magnetic resonance on single defect centers. *Science*, 276(5321):2012–2014, 1997.

[56] LHG Tizei and M Kociak. Spatially resolved quantum nano-optics of single photons using an electron microscope. *Physical Review Letters*, 110(15):153604, 2013.

[57] S Meuret, LHG Tizei, T Cazimajou, R Bourrellier, HC Chang, F Treussart, and M Kociak. Photon bunching in cathodoluminescence. *Physical Review Letters*, 114(19):197401, 2015.

[58] Alexios Beveratos, Rosa Brouri, Thierry Gacoin, Jean-Philippe Poizat, and Philippe Grangier. Nonclassical radiation from diamond nanocrystals. *Physical Review A*, 64(6):061802, 2001.

[59] Christian Kurtsiefer, Sonja Mayer, Patrick Zarda, and Harald Weinfurter. Stable solid-state source of single photons. *Physical Review Letters*, 85(2):290, 2000.

[60] Alexios Beveratos, Rosa Brouri, J-P Poizat, and Philippe Grangier. Bunching and antibunching from single nv color centers in diamond. In *Quantum Communication, Computing, and Measurement 3*, pages 261–267. Springer, 2002.

[61] Rosa Brouri, Alexios Beveratos, Jean-Philippe Poizat, and Philippe Grangier. Photon antibunching in the fluorescence of individual color centers in diamond. *Optics Letters*, 25(17):1294–1296, 2000.

[62] J Bernard, L Fleury, H Talon, and M Orrit. Photon bunching in the fluorescence from single molecules: A probe for intersystem crossing. *The Journal of Chemical Physics*, 98(2):850–859, 1993.

[63] Fedor Jelezko, T Gaebel, I Popa, A Gruber, and Jorg Wrachtrup. Observation of coherent oscillations in a single electron spin. *Physical Review Letters*, 92(7):076401, 2004.

[64] Jed I Ziegler and Richard F Haglund Jr. Complex polarization response in plasmonic nanospirals. *Plasmonics*, 8(2):571–579, 2013.

[65] Jed I Ziegler and Richard F Haglund Jr. Plasmonic response of nanoscale spirals. *Nano Letters*, 10(8):3013–3018, 2010.

[66] Dmitry Pestov, Vadim V Lozovoy, and Marcos Dantus. Multiple independent comb shaping (mics): Phase-only generation of optical pulse sequences. *Optics Express*, 17(16):14351–14361, 2009.

[67] Andrew M Weiner. Femtosecond pulse shaping using spatial light modulators. *Review of Scientific Instruments*, 71(5):1929–1960, 2000.

[68] Arthur Losquin and Mathieu Kociak. Link between cathodoluminescence and electron energy loss spectroscopy and the radiative and full electromagnetic local density of states. *ACS Photonics*, 2(11):1619–1627, 2015.

[69] Robert Czaplicki, Mariusz Zdanowicz, Kalle Koskinen, Janne Laukkanen, Markku Kuittinen, and Martti Kauranen. Dipole limit in second-harmonic generation from arrays of gold nanoparticles. *Optics Express*, 19(27):26866–26871, 2011.

[70] Bettina Frank, Xinghui Yin, Martin Schaferling, Jun Zhao, Sven M Hein, Paul V Braun, and Harald Giessen. Large-area 3d chiral plasmonic structures. *ACS Nano*, 7(7):6321–6329, 2013.

[71] Martin Schäferling, Daniel Dregely, Mario Hentschel, and Harald Giessen. Tailoring enhanced optical chirality: design principles for chiral plasmonic nanostructures. *Physical Review X*, 2(3):031010, 2012.

[72] A Papakostas, A Potts, DM Bagnall, SL Prosvirnin, HJ Coles, and NI Zheludev. Optical manifestations of planar chirality. *Physical Review Letters*, 90(10):107404, 2003.

[73] Makoto Kuwata-Gonokami, Nobuyoshi Saito, Yusuke Ino, Martti Kauranen, Konstantins Jefimovs, Tuomas Vallius, Jari Turunen, and Yuri Svirko. Giant optical activity in quasi-two-dimensional planar nanostructures. *Physical Review Letters*, 95(22):227401, 2005.

[74] Mengxin Ren, Eric Plum, Jingjun Xu, and Nikolay I Zheludev. Giant nonlinear optical activity in a plasmonic metamaterial. *Nature Communications*, 3:833, 2012.

[75] Nils Calander, Ignacy Gryczynski, and Zygmunt Gryczynski. Interference of surface plasmon resonances causes enhanced depolarized light scattering from metal nanoparticles. *Chemical Physics Letters*, 434(4):326–330, 2007.

[76] John C Heckel and George Chumanov. Depolarized light scattering from single silver nanoparticles. *The Journal of Physical Chemistry C*, 115(15):7261–7269, 2011.

[77] Nikolay I Zheludev and Yuri S Kivshar. From metamaterials to metadevices. *Nature Materials*, 11(11):917–924, 2012.

[78] Wenshan Cai, Alok P Vasudev, and Mark L Brongersma. Electrically controlled nonlinear generation of light with plasmonics. *Science*, 333(6050):1720–1723, 2011.

[79] Lei Kang, Yonghao Cui, Shoufeng Lan, Sean P Rodrigues, Mark L Brongersma, and Wenshan Cai. Electrifying photonic metamaterials for tunable nonlinear optics. *Nature Communications*, 5:1–7, 2014.

[80] Dmitry Pestov, Vadim V. Lozovoy, and Marcos Dantus. Multiple independent comb shaping (mics): Phase-only generation of optical pulse sequences. *Optics Express*, 17(16):14351–14361, Aug 2009.

[81] C. Sönnichsen, T. Franzl, T. Wilk, G. von Plessen, J. Feldmann, O. Wilson, and P. Mulvaney. Drastic reduction of plasmon damping in gold nanorods. *Physical Review Letters*, 88:077402, Jan 2002.

[82] Marion Cornet, Jérôme Degert, Emmanuel Abraham, and Eric Freysz. Terahertz-field-induced second harmonic generation through pockels effect in zinc telluride crystal. *Optics Letters*, 39(20):5921–5924, 2014.

[83] Peter L Knight and Peter W Milonni. The rabi frequency in optical spectra. *Physics Reports*, 66(2):21–107, 1980.

[84] Marcus W Doherty, Neil B Manson, Paul Delaney, Fedor Jelezko, Jörg Wrachtrup, and Lloyd CL Hollenberg. The nitrogen-vacancy colour centre in diamond. *Physics Reports*, 528(1):1–45, 2013.

[85] Dmitry Budker. Diamond nanosensors: The sense of colour centres. *Nature Physics*, 7:453–454, 2011.

[86] RH Ritchie. Plasma losses by fast electrons in thin films. *Physical Review*, 106(5):874, 1957.

[87] L Zhang, R Erni, J Verbeeck, and G Van Tendeloo. Retrieving the dielectric function of diamond from valence electron energy-loss spectroscopy. *Physical Review B*, 77(19):195119, 2008.

[88] Kazuyuki Fujii. Introduction to the rotating wave approximation (rwa): Two coherent oscillations. *arXiv preprint arXiv:1301.3585*, 2013.

[89] Giuliana Di Martino, Yannick Sonnefraud, Mark S Tame, Stéphane Kéna-Cohen, F Dieleman, ŞK Özdemir, MS Kim, and Stefan A Maier. Observation of quantum interference in the plasmonic hong-ou-mandel effect. *Physical Review Applied*, 1(3):034004, 2014.

[90] Reinier W Heeres, Leo P Kouwenhoven, and Valery Zwiller. Quantum interference in plasmonic circuits. *Nature Nanotechnology*, 8(10):719–722, 2013.

[91] James S Fakonas, Hyunseok Lee, Yousif A Kelaita, and Harry A Atwater. Two-plasmon quantum interference. *Nature Photonics*, 8(4):317–320, 2014.

[92] GS Agarwal. I master equation methods in quantum optics. *Progress in Optics*, 11:1–76, 1973.

[93] JR Johansson, PD Nation, and Franco Nori. Qutip 2: A python framework for the dynamics of open quantum systems. *Computer Physics Communications*, 184(4):1234–1240, 2013.

[94] G Liaugaudas, G Davies, K Suhling, RUA Khan, and DJF Evans. Luminescence lifetimes of neutral nitrogen-vacancy centres in synthetic diamond containing nitrogen. *Journal of Physics: Condensed Matter*, 24(43):435503, 2012.

[95] Benjamin J Lawrie, Philip G Evans, and Raphael C Pooser. Local surface plasmon mediated extraordinary optical transmission of multi-spatial-mode quantum noise reduction. *Physical Review Letters*, 110(15):156802, 2013.

[96] MW Holtfrerich, M Dowran, R Davidson, BJ Lawrie, RC Pooser, and AM Marino. Toward quantum plasmonic networks. *Optica*, 3(9):985–988, 2016.

[97] Raphael C Pooser and Benjamin Lawrie. Plasmonic trace sensing below the photon shot noise limit. *ACS Photonics*, 3(1):8–13, 2015.

[98] Wenjiang Fan, Benjamin J Lawrie, and Raphael C Pooser. Quantum plasmonic sensing. *Physical Review A*, 92(5):053812, 2015.

[99] F. Dominec. Fdtd grid 2-d and 3-d.

[100] Kane S Yee et al. Numerical solution of initial boundary value problems involving maxwells equations in isotropic media. *IEEE Trans. Antennas Propag*, 14(3):302–307, 1966.

[101] Allen Taflove, Susan C Hagness, et al. Computational electrodynamics: the finite-difference time-domain method. *Norwood, 2nd Edition, MA: Artech House, l995*, 1995.

[102] Guy AE Vandenbosch. *Computational Electromagnetics in Plasmonics*. INTECH Open Access Publisher, 2012.

[103] G Vecchi, V Giannini, and J Gómez Rivas. Shaping the fluorescent emission by lattice resonances in plasmonic crystals of nanoantennas. *Physical Review Letters*, 102(14):146807, 2009.

[104] Benjamin Gallinet and Olivier JF Martin. Relation between near–field and far–field properties of plasmonic fano resonances. *Optics Express*, 19(22):22167–22175, 2011.

[105] Shuang Zhang, Dentcho A Genov, Yuan Wang, Ming Liu, and Xiang Zhang. Plasmon-induced transparency in metamaterials. *Physical Review Letters*, 101(4):047401, 2008.

[106] Na Liu, Lutz Langguth, Thomas Weiss, Jürgen Kästel, Michael Fleischhauer, Tilman Pfau, and Harald Giessen. Plasmonic analogue of electromagnetically induced transparency at the drude damping limit. *Nature Materials*, 8(9):758–762, 2009.

[107] Srdjan S Acimovic, Mark P Kreuzer, María U González, and Romain Quidant. Plasmon near-field coupling in metal dimers as a step toward single-molecule sensing. *ACS Nano*, 3(5):1231–1237, 2009.

[108] RFW Pease. Electron beam lithography. *Contemporary Physics*, 22(3):265–290, 1981.

[109] THP Chang. Proximity effect in electron-beam lithography. *Journal of Vacuum Science & Technology*, 12(6):1271–1275, 1975.

[110] Vitor R Manfrinato, Lihua Zhang, Dong Su, Huigao Duan, Richard G Hobbs, Eric A Stach, and Karl K Berggren. Resolution limits of electron-beam lithography toward the atomic scale. *Nano Letters*, 13(4):1555–1558, 2013.

[111] LA Giannuzzi and FA Stevie. A review of focused ion beam milling techniques for tem specimen preparation. *Micron*, 30(3):197–204, 1999.

[112] REJ Watkins, P Rockett, S Thoms, R Clampitt, and R Syms. Focused ion beam milling. *Vacuum*, 36(11-12):961–967, 1986.